DEPARTMENT OF PHYSICS
UNIVERSITY OF JYVÄSKYLÄ
RESEARCH REPORT No. 6/2009

COMPUTATIONAL STUDIES OF DEFECTS IN GRAPHENE AND CARBON NANOTUBES

BY
SAMI MALOLA

Academic Dissertation
for the Degree of
Doctor of Philosophy

To be presented, by permission of the
Faculty of Mathematics and Natural Sciences
of the University of Jyväskylä,
for public examination in Auditorium FYS-1 of the
University of Jyväskylä on August 14th, 2009
at 12 o'clock noon

Jyväskylä, Finland
July 2009

Preface

This work was done at the Nanoscience Center, Physics Department of the University of Jyväskylä between years 2006 and 2009.

I would like to thank my supervisors Professor Hannu Häkkinen and PhD Pekka Koskinen for the motivating guidance throughout the work. Their help and expertise have been always near when I have needed it.

I have got important advice also from other people: Matti Manninen, Kimmo Tuominen and Mika Pettersson. Group members and people in Nanoscience Center and Physics Department deserve acknowledgements about the fruitful discussions, help in all kind of practical and technical problems, and especially creating great working environment.

I am grateful about the financial support from the Finnish Cultural Foundation, which covered most of my PhD studies. About computational resources, I thank the Finnish IT Center for Science, CSC.

Finally, I would like to thank my parents for all the support they have given me during these three years. Thanks also for all my friends and relatives for the spare time which we have spend together. I am happy that you have given me also something else to think about than science.

Jyväskylä, July 2009

Sami Malola

Abstract

Carbon structures have a big role in nanoscience today because of their rich and promising electrical, mechanical and optical properties. However, advancing these properties requires understanding the underlying structure and its behavior. In addition to ideal systems, defects are frequently unavoidable in experiments; hence their effects, along with their possibilities to enrich the functionalities of carbon nanostructures, should be investigated.

This thesis concentrates on computational studies of various defects in graphene and carbon nanotubes. It combines investigations of changes in Raman-active modes of single-walled carbon nanotubes due to vacancies and bending, reconstructions for graphene edges, and adsorption and diffusion mechanism of single gold atoms in graphene. Most of the results can be understood in terms of simple physical principles and relations to experiments are discussed in detail.

Effects of carbon atom vacancies on Raman-active phonons are understood via their symmetry properties and structural weakening. However, the effect of tube bending on Raman-active modes is complicated to understand. Bending proved to be computationally challenging, but our so-called wedge boundary conditions offered a way to practical modeling. Wedge boundary conditions are free from constraints and finite-size effects, and really make bending the only disturbance in the system. This kind of approach will be useful for other physical problems as well.

In this thesis we found a new ground state for graphene edges — a new edge beyond armchair and zigzag. We show that this specific reconstruction of zigzag self-passivates the edge against molecular hydrogen adsorption and increases the rigidity of the graphene edge. We discuss about the possibilities to identify the edge structure from scanning tunneling microscope (STM) images, Raman-active modes and vibrational properties relating the differences to physical properties.

This thesis also shows that gold atoms are thermally stable in-plane with graphene opening possibilities to tune the properties of carbon nanostructures. Our results confirm that, in addition to imaging, transmission electron microscope (TEM) has a great potential as a preparation tool for samples of carbon nanomaterials containing metals. Because contacts may dominate behaviour in nanosize systems, understanding the metal-carbon interface through defects like vacancies is important. With the help of TEM-beam there can be a way to selectively make direct contacts with metals and carbon nanostructures at any point of the lattice, not only at the edges.

Author's address Sami Malola
Department of Physics
University of Jyväskylä
Finland

Supervisors Professor Hannu Häkkinen
Department of Physics and
Department of Chemistry
University of Jyväskylä
Finland

PhD Pekka Koskinen
Department of Physics
University of Jyväskylä
Finland

Reviewers Professor Kai Nordlund
Department of Physics
University of Helsinki
Finland

PhD Ari P. Seitsonen
CNRS, IMPMC
University of Pierre and Marie Curie
France

Opponent Professor David Tománek
Physics and Astronomy Department
Michigan State University
USA

List of Publications

I S. Malola, H. Häkkinen and P. Koskinen, *Raman spectra of single-walled carbon nanotubes with vacancies* Phys. Rev. B **77**, 155412 (2008)

II S. Malola, H. Häkkinen and P. Koskinen, *Effect of bending on Raman-active modes of carbon nanotubes* Phys. Rev. B **78**, 153409 (2008)

III P. Koskinen, S. Malola and H. Häkkinen, *Self-passivating edge reconstructions of graphene* Phys. Rev. Lett. **101**, 115502 (2008)

IV S. Malola, H. Häkkinen and P. Koskinen, *Comparison of Raman spectra and vibrational density of states between graphene nanoribbons with different edges* Eur. Phys. J. D **52**, 71 (2009)

V S. Malola, H. Häkkinen and P. Koskinen, *Gold in graphene: In-plane adsorption and diffusion* Appl. Phys. Lett. **94**, 043106 (2009)

The author has done all of the numerical calculations and written the drafts of articles **I**, **II**, **IV** and **V**. He has implemented the computer codes needed in non-resonant Raman calculation, symmetry separation of Raman active modes and analysis in **I**, **II** and **IV**. The author has also done required changes for DFTB-code to use it with the wedge boundary conditions related to article **II**. In addition, the author has done the calculations, from which the zigzag edge reconstruction was originally observed and has participated in writing and doing computations in the article **III**.

Contents

1 Introduction

1.1 Step inside nanoscience

Dreams make breakthroughs; stop dreaming and you will stop. A researcher of nanoscience has nanosize dreams, in which self-guiding nanorobots carry medicine inside human body to areas, where the blades of the surgeons are too big and clumsy to reach. Nanorobots have started labeling already minor changes in human body, eliminating cancer cells before they proceed to be fatal. Quantum computer has become every day life and is not anymore an old fashioned dream. Nanoelectronic components are freely scalable in size down to nano and can be easily integrated with macrosize devices. Nano, spelled as a word has the same effect on people's minds as kilo when buying apples from the store. Wait a minute — am I still dreaming?

Word "nano" describes the length scale, word "science" separates reality from the dreams. A chain of eight carbon atoms is nanometer long and to describe nanoscale system individual atoms have to be counted. Atoms consist of nuclei and electrons, which can be described sensibly only by using quantum mechanics — the method for most of the nanoscience studies. Almost every study about the properties of small compounds of atoms can be considered to be part of nanoscience.

Is there, after all, any good reason to call research of small compounds of atoms with a common name — nanoscience? Well, is there a good reason to call research of nuclei of atoms as nuclear physics? Furthermore, why don't we call physics just science? Specifying the research of small compounds under a common name, nanoscience, is the first try to gather researchers doing similar things; the first try to get them work together.

Nanoscience has an ambitious goal — to combine the three different fields biology, chemistry and physics. It tries to advance knowledge from all of them and starts looking at the scientific problems from various angles at the same time, not only concentrating on components of living organisms, reactions between molecules or dynamics of the atoms. Here, to find the common and understandable scientific language is one of the first and at the same time biggest obstacles. In achieving such a fictitious dream as self-guiding nanorobots for example, to gather knowledge of biology, chemistry and physics together becomes one of the greatest abilities.

Why won't we just forget nano — we know already too much about macroworld. Do we? Everything builds up from small, so understanding the world in nanoscale helps us to understand the world in macroscale. Since the rules of the macroworld are not all valid in the nanoworld, all the phenomena can not be generalized. One common example is gold, whose behavior is much more reactive as a small nanosize clusters than as a bulk material. This example emphasizes that small can make a difference and that investigation of phenomena on the nanoscale is needed. Even though you cannot see nanoscale objects with your own eyes, it does not mean that they would not be important. Nanoscience can help in finding solutions for example for the overloading energy consumption of the world. Maximizing the functionality of different materials like solar cells through nanomaterial design does not sound too utopistic dream anymore. It may not solve all the problems, but every step forward helps. Maybe the breakthroughs will come from those fields, that we have not yet looked at.

Is basic research just for mad men's curiosity? Making devices and applications is hard from material whose properties are unknown. The engineer becomes a magician, drawing devices out of a hat. One can of course try, and try another time, but after ten trials and an awful headache, it is good to think through why the invention did not work. Here the basic research steps into the picture, creating the fundamental limits and opening new insights for new device inventions.

Nanoscience is still rather at the stage of finding general understanding than at the stage of developing devices. There are still ongoing attempts to achieve better resolution in experimental imaging methods, to prepare the samples selectively and to overcome the accuracy and efficiency barriers in computer simulations of realistic system sizes. Solving these problems are steps we still have to take before understanding thoroughly phenomena in the nanoscale systems — not steps taken during invention of well functioning nanodevices.

1.2 Carbon nanostructures

The stage of research of the carbon nanomaterials may be closer to real applications than the stage of research of any other nanomaterial — at least hopes are high. Carbon nanostructures are mostly well known and also have been made and imaged successfully. The concern has turned from understanding pure structures to defects, which have also been investigated in various ways already. The first steps to control defects experimentally have been taken.

Carbon is one of the most prominent elements in nature, vital for biology and life. Discoveries of modern carbon nanomaterials in 80's and 90's have influenced widely

the interest in nanoscience: fullerenes found by Kroto et. al. in 1985 [1] and carbon nanotubes found by Iijima in 1991 [2]. Today they create the sharpest front-edge of the field, together with graphene. Without advantageous properties, a discovery itself does not initiate long-lasting interest. Carbon as an element allows flexible bonding giving possibility to build a wide range of different materials; hence leading to rich physical properties. Here, the modern carbon nanomaterials make definitely no exception.

Although macroscopic carbon structures of amorphous carbon, graphite and diamond have been known for a long time [3], graphene has stepped out in spotlights truly within recent years. The breakthrough progress was made in experimental processing and imaging methods to reach limit of single atomic layer [4–9]. Graphene can be considered as a structural basis for most of the other carbon nanomaterials [10]. Going into details of structures shown in figure 1.1, graphene itself consists of a hexagonal honeycomb lattice with sp^2 hybridization. Stacking several layers on top of each other makes graphene graphite, in which different layers are bound together with weak van der Waals forces. Carbon nanotubes can be considered as a cylinder rolled out of a rectangular piece of graphene. Rolling direction defines the type of the tube giving zigzag, armchair and achiral tubes, among which there can be both semiconductive and metallic structures. Fullerenes are spherical molecules that can be wrapped-out from graphene, but in addition to hexagons, at least pentagons have to be added to create a sensible curvature and spherical shape. Diamond has its own crystal structure, in which each carbon is covalently bond to four neighboring carbon atoms giving sp^3 hybridized atoms. Compared to graphite, diamond has no such weakly interacting layered structure. Modern carbon nanomaterials give the full range in dimensions; 0D fullerenes, 1D nanotubes and graphene nanoribbons, 2D graphene, and 3D graphite and diamond. Dimension gives its own flavour for properties like the electron density of states, with examples shown in figure 1.2.

From these modern carbon nanomaterials, carbon nanotubes and graphene are the most promising for applications, because of the promising structural, mechanical, electrical, and optical properties [10–14]. Wide range of applications like nanoelectronic components, nanoelectromechanical devices, hydrogen and energy storage material, sensors, and high-strength composites [15–17] take advantage of these properties. As an example, hydrogen storage applications advances binding properties, nanoelectronics semiconductive and metallic characteristics, and mechanical devices high strength of hexagonal network, especially in carbon nanotubes.

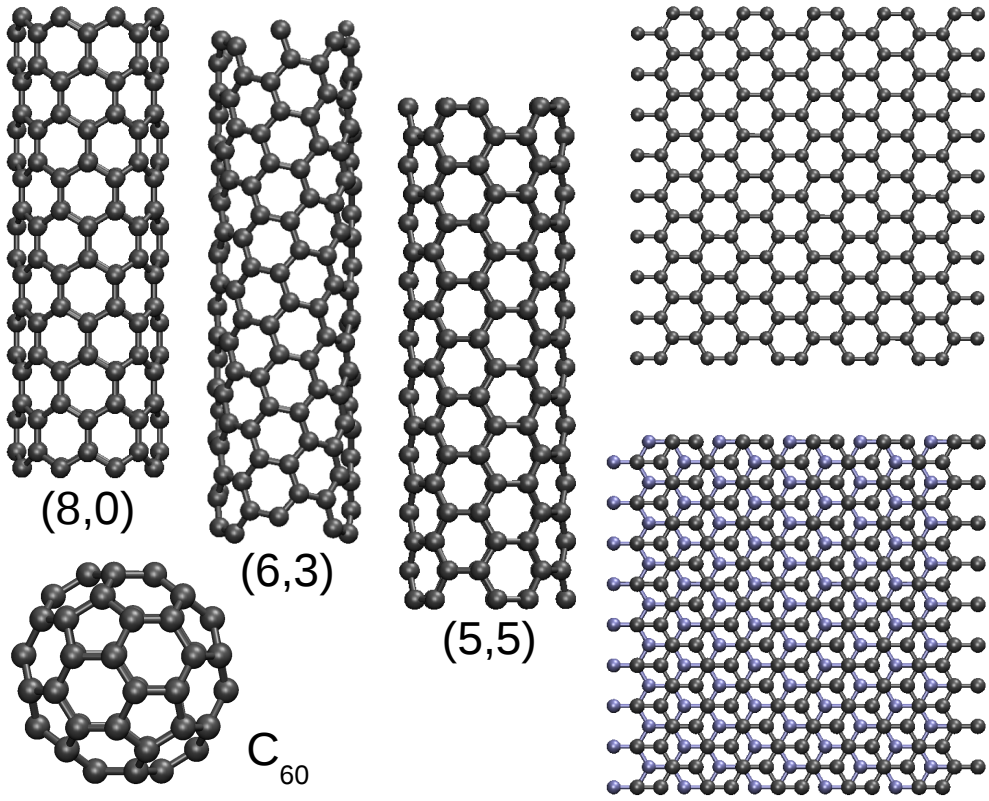

Figure 1.1: Carbon nanostructures: (8,0) zigzag, (6,3) chiral and (5,5) armchair nanotubes, C60 fullerene, a single graphene sheet, and graphite showing the $ABAB\ldots$ packing.

1.3 Defects in carbon nanostructures

1.3.1 Ad-atoms and vacancies

Flexible bonding properties of carbon give various different possibilities to even enrich the properties of carbon nanotubes and graphene with different defects and ad-atoms; also combinations of different type of carbon nanomaterials are possible [18]. For example, deposition of metal atoms or molecules, or incorporation of nitrogen or boron in the structures can be used to tune chemical activity and structural behavior. In general, metal atoms have fundamental relevance in catalysis, batteries, and nanoelectronics [19–22].

Deposited atoms can be thought of as point defects, just like vacancies. Vacancies are holes, which make the structure weaker. Differences between the defect and the lattice atoms affect the binding strength together with the possible presence of vacancies. Namely, ad-atoms can be found to be non-covalently bonded on top of the structures, outside the lattice, or covalently bonded inside the lattice. Comparing the mass and the number of valence electrons between the elements reveals whether they are made for each other, i.e. whether there is an elephant or just another species of ant inside the anthill. Carbon nanostructure is here the anthill and nitrogen and boron would be another ant species and a metal atom like gold more like the elephant.

Vacancies are needed in formation of junctions between carbon nanotubes and therefore correct preparation can improve the stiffness of composite materials. Although not in all cases preferred, the existence of defects in samples is often unavoidable, because of the growth, the preparation, and the imaging methods. Research on the field so far has given explanations about electronic properties of defects and junctions [23–27], defect stability [25, 26, 28], defect identification [25, 29, 30], local vibrational density of states [31], and defect diffusion [32].

1.3.2 Bending of carbon nanotubes

In practice, because carbon nanotubes (CNTs) are long, they can bend. Bending within elastic limits can be categorized as a continuous defect that maintains the structure. Bending is observed in isolated CNTs between electrodes [33], or in "paper" [34], "forests" [35], rings [36], and composite systems [37] made out of CNTs. Nanotube serpentines [38] are newly found structures, which are processed on the specific stepped substrates like quartz. Nanotube serpentines are an example of systems where a defect can open ways for new applications. Same kind of wiggly structures are familiar from many well-known macroscopic devices like heating or cooling elements,

antennas, and radiators.

It appears that bending is ubiquitous in experiments—and challenging to study theoretically. For example most of the previous theoretical Raman studies are for straight tubes, because modeling of bent systems has been computationally too expensive [11]. Modeling of bending with classical methods is straightforward and has been used to study force moments and strains [39], structural deformations like buckling [40–43] and other large-scale mechanical properties that result from rather high curvature [44].

1.3.3 Edges of carbon nanostructures

Edges play crucial role in chemical reactivity [45], electronic structure [46] and vibrations [47]. The edge chemistry is important for example in the catalyzed growth of carbon nanotubes [48, 49], to which carbon-metal interface is also related. The electronic properties of graphene, as well as carbon nanotube armchair and zigzag edges, have been studied extensively [46, 50], often in connection with the nanotube growth [48, 51], or the so-called electronic "edge states" [45, 52, 53].

Because of the lower coordination, atoms on the edges are exposed to reconstructions more than atoms inside the material. This effect is akin to melting, which also usually starts from the surface or around a defect. Edge reconstructions have already been studied, but usually it has meant edge roughness [52, 54] or dramatic folding of the edge into a loop [55]. Effects of different edge structures of graphene nanoribbons have been reported on functionality of nanoelectronic devices like transistors [56, 57], but including only different compositions of zigzag and armchair edges. Big vacancies also have edges which can deform through reconstructions [58]. Though, in the case of small few-atom vacancies, the edges can not be contrasted to actual long free edges of graphene or to open nanotube ends, in which reconstructions plays role during the closure [59]. Usually in research of graphene, zigzag and armchair have got the entire attention as the two basic edges; it has been the first natural intuition based on the underlying hexagonal lattice.

1.4 Structural detection and modeling

Since the properties of a nanomaterial depend on the precise atomic geometry, its knowledge is crucial for focused preparation of experiments and for worthy theoretical modeling. From the experimental point of view the nanoscale size makes the structural characterization complicated. Furthermore, accurate theoretical calculations for reasonable size nanoscale systems often need remarkable computational resources, which

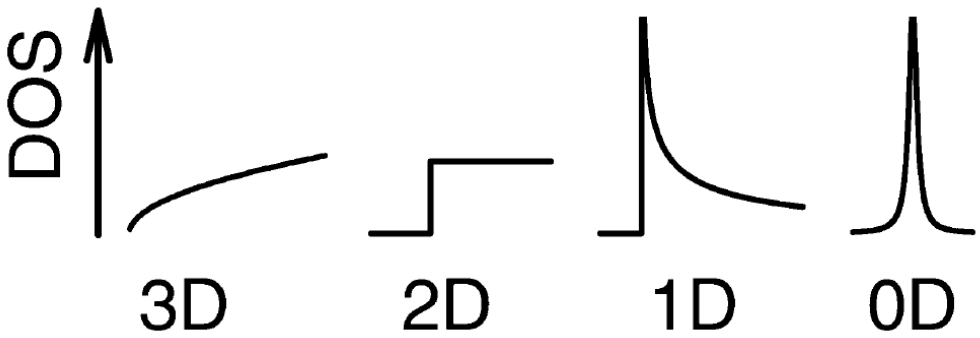

Figure 1.2: Characteristics of the electron density of states for materials in different dimensions. Taken from Ref. [14].

makes the interplay with experiments challenging.

From a theoretical point of view the invention of density-functional theory (DFT) in the middle of 20th century [60], has solved many difficulties. DFT has become one of the most powerful and common theoretical methods for nanoscience. Through Hohenberg-Kohn theorem [61] the method reduces the many electron problem to depend only on one key variable — electron density. Kohn-Sham method [62] models the system with non-interacting electrons diminishing the many electron problem effectively into a set of single particle problems. The critical, approximative part of the method — the exchange-correlation functional — aims to describe all of the essential interactions left out in derivation. Today there exist plenty of functionals for different purposes. With help of DFT scientists have had definitely sharper teeth against chunk of physics problems than without it.

For detecting the structural properties experimentally, Raman spectroscopy is one of the basic tools [11, 63–66]. In the Raman scattering process a laser field excites the electrons that are further scattered by phonons — the fingerprint of nuclear motion and bond strengths. After phonon scattering, the rest of the excitations decay and emitted light can be measured. Intensity and energy details of the characteristic bands in the spectra will get rather small structural differences to emerge. Resonance in electron transitions between the real states enhances the intensity as is schematically shown in figure 1.3; in 1D carbon nanotubes van Hove singularities have a dominating role. One of the advantageous properties of carbon nanotubes is the characteristic inverse diameter behavior of the low energy modes, radial breathing mode (RBM) in particular. With help of Kataura plot [14] presenting the excitation energies with respect to tube diameter in figure 1.3, chirality detection can be done based on experimental

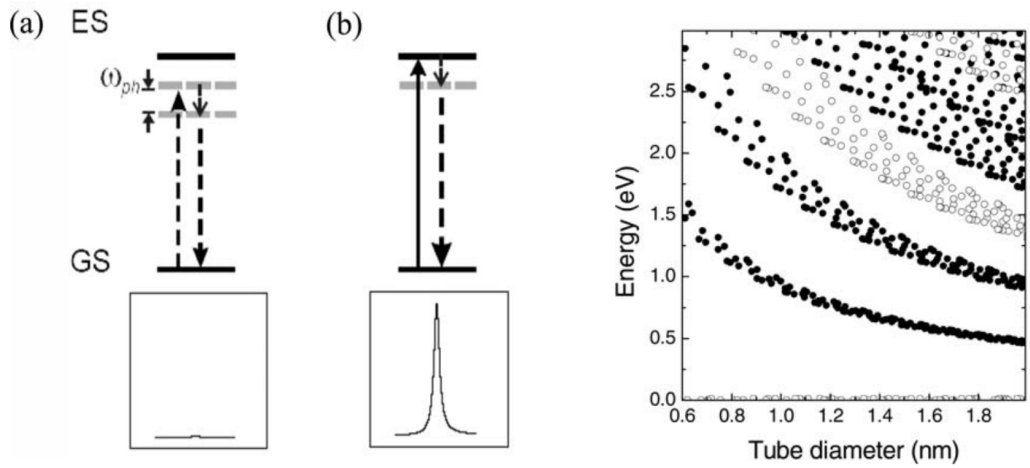

Figure 1.3: On the left: Schematic view of the scattering process and the resonant effect due to transitions between real electron states shown in (b) compared to transitions between artificial states in (a). GS is for ground and ES for excited state, and ω_{ph} is the frequency of the phonon. The height of the peak shows the influence of the resonance on the Raman intensity. On the right: Kataura plot; electron transition energies due to van Hove singularities with respect to diameter for semiconductive (empty) and metallic (filled) tubes. Different arrays of the data points refer to different kind of electronic transitions. Taken from Ref. [14].

laser energies. Identifying chirality of an isolated tube would be one step closer to selective sample preparation for applications.

To describe the resonance effects theoretically, the full scattering process must be followed. Solving excited states correctly, estimating electron-phonon coupling [67, 68], and carrying out all the possible transitions and phonons in the momentum space complicates the calculations greatly. For ideal systems simplifications in formulation and reductions in number of atoms and phonons can be done [69], but for non-ideal defective systems this is questionable. Defects require to take into account more atoms and also usually break the nice simplifications.

Raman spectroscopy is not the only tool for structural detection. Imaging methods like transmission electron microscopy (TEM) [70, 71] and scanning tunneling microscopy (STM) [53] aim to give a realistic image about the structure. In TEM-imaging electron beam is used to bombard the sample and the beam scattered through is measured. Differences in measured intensity of the beam gives information about the structure; most of the electrons scattering back from the nuclei. Because of the high-energy electron beam displacing light elements, generation of defects with the TEM is possible.

In STM-imaging the electrons that tunnel between the sample and a conductive tip are measured, and this gives the information about the differences in electron density

of the system. In the points of space where electron density close to Fermi energy is higher, the tip must be raised to maintain the constant current. However, these imaging methods have disadvantages: single atom resolution is hard to reach and the electron bombardment in TEM-imaging excites easily the motion of light elements like carbon. Therefore the most important details might be hidden in bad resolution, or the system may not remain in the true thermal equilibrium. But these are the conditions for all of the other imaging methods too, whenever they try to reach the atom resolution. Is it after all possible to reach atomic resolution without affecting and interacting strongly with the structures? Separation of individual atoms requires to go deep into the quantum mechanical and nanoscale phenomena, which are in general complicated to control. If the same holds for imaging, separation of atoms will also be complicated and will then need strong interaction with the sample.

The stage of TEM-imaging as an experimental method is sort of similar to the stage of DFT in computational side, both having some difficulties and reliability problems, but without them we would be far behind from development of today's nanoscience. Still, at least I personally prefer to see something, if another choice is to be blind on everything about the structures. Restrictions of the methods increase the importance of the interplay between computational and experimental sciences to confirm and explain observations. In other words, although neither theory nor experiment would be absolutely accurate, together they can give correct explanations.

2 Theory & Methods

2.1 Density-functional theory

Density functional theory (DFT) was developed in the middle of 20th century and is nowadays widely used method in computational nanoscale material science. It is a quantum mechanical method and useful for many-electron problems. Extensions to standard DFT, especially time-dependent DFT (TD-DFT) has solved some of the problems in standard DFT.

Atomistic systems must be considered as many-body problems consisting of two kind of species: nuclei and electrons. To describe the problem correctly, interactions between the species are needed to construct the Schrödinger equation. Because of the mass difference between nuclei and electrons one very useful approximation can be made — the Born-Oppenheimer (BO) approximation, which separates nuclear and electronic parts of wavefunction. Because of the huge mass difference between nuclei and electrons BO assumes, that the nuclei affect on electrons effectively through their fixed positions. Under the BO-approximation many-body problem of both electrons and nuclei diminishes in solving only the many-electron problem.

Density-functional theory is based on the Hohenberg-Kohn theorem [61] which states that there is a unique mapping between the ground state electron density, the electron wavefunction and the effective potential. Furthermore, every ground state observable inherit the same unique connection to electron density through the ground state wavefunction. This theorem reduces the full many-electron problem to depend only on one variable — electron density, that determines all the observables as well as the full many-electron wavefunction.

At this point the many-electron problem is still too time-consuming and complicated to handle. The Hellman-Feynman theorem indicates through the integration of equation (A.6) in Appendix A that the total energy of interacting many-electron system can be always found using a one-electron theory. The Hellman-Feynman theorem also allows to solve forces directly from the derivative of the Hamiltonian. The Kohn-Sham method completes the standard DFT approach. It simplifies the true interacting system with a non-interacting model system that gives the same electron density as the interacting system. With the help of the Hellman-Feynman theorem this is a reasonable task to accomplish. The interactions not taken into account in the non-interacting

model system are fitted to an extra energy term called exchange-correlation energy. If the exchange-correlation energy is exact, also the Kohn-Sham method is exact. The Kohn-Sham approach transforms the many-electron problem to a set of separate, coupled single-electron problems. The Kohn-Sham equations must be solved self-consistently including definitions of electron density, Kohn-Sham potential and single-particle Schrödinger equations.

The details of the formal derivation of the Kohn-Sham approach are described in Appendix A. DFT needs approximations for the exchange-correlation functional and a suitable basis set for single-electron wavefunctions. Although the contribution from the exchange-correlation energy into the total energy is small, it plays a crucial role in determining energy differences, like the adsorption energy. Usual choices for the basis set are plane waves, atomic orbitals or Gaussian functions; the first one uses Bloch's theorem to describe the electron wavefunctions in periodic potential of a lattice. The second one describes the atomic orbitals and the third one treats the wavefunctions with a set of Gaussian functions.

In addition to basis sets, there exists simplifications for decreasing the computational load. Pseudo potentials simplify the inert core states of electrons with simple potential and solves the problem only for relevant valence electron states. Solutions of the pseudo potential method are pseudo wavefunctions, which differ from real wavefunctions, but give otherwise the same information about the measurable observables.

2.1.1 GPAW, DFT software

GPAW is an all-electron real-space grid code [72]. It scales well in massively parallel computations, and is therefore an efficient DFT-code. As the end of the name reveals, the electronic wavefunctions are treated by projector-augmented waves (PAW) [73]. Projector-augmented waves method relies on linear transformations that relate more practical pseudo-wavefunctions to true all-electron wavefunctions. In other words, the linear transformation gives the transformation from pseudo wavefunctions to all-electron wavefunctions.

PAW uses principles familiar from pure pseudo-potential methods, but does not require norm-conservation of the wavefunctions. Core-electron states are considered to be fixed and the valence states are expanded into partial-waves inside specific augmentation regions around each atom. Because of the cut-off, smoothness at the boundary of the augmentation regions has to be considered. Outside of the regions wavefunctions are fitted to true all-electron wavefunctions, which indicates that the linear transformation acts only inside of the augmentation regions. Augmentation is realized as an increase from smooth pseudo-wavefunctions to true all-electron wavefunctions when the transformation is taken. Formal details of PAW can be found from Appendix C.

For the exchange-correlation functional the current implementation of GPAW offers all of the usual ones including local density (LDA) and generalized gradient approximations (GGA). In LDA the exchange-correlation contribution is evaluated using only the value of the exchange-correlation functional at each point. Hence LDA does not take into account the local curvature of the electron density. The local spin density approximation (LSD) is a spin-dependent version of LDA.

GGA is one step further from LDA and takes into account small curvature effects around each point in space. GGA functionals take into account density gradient dependencies on the exchange-correlation energy. By expansion into the first-order, the gradient expansion approximation (GEA) is established, while LDA describes the zeroth order expansion. GEA functional however violates some analytic conditions of exchange hole e.g. being negative definite and normalizing to -1. These failures will be corrected in GGA functionals by using cut off procedures for exchange hole. Afterall, where LDA fails to describe systems with slowly varying electron densities, GGA usually works more accurately also in these cases.

There are plenty of different functionals for GGA, both empirically and theoretically grounded. The problem with functionals, that are fitted to experimental parameters, is the weak relation to basic physical principles. In addition, empirically built functionals usually work only for those systems for which they are fitted. In theoretically grounded GGA functionals, the limits from the background physics are usually better known. One version of theoretically built GGA-functionals, relevant to this thesis, was made by Perdew, Burke and Ernzerhof (PBE) [74], from which full details together with LDA and general GGA-functionals is represented in Appendix B.

GPAW uses a double-grid method by Ono and Hirose [75], in which the main discretization is done in a coarse-grid and the final accuracy is achieved by interpolating electron densities, wavefunctions and potentials to a denser grid.

2.2 Density-functional tight-binding method

The density-functional tight-binding (DFTB) method was developed in the 90's as a computationally efficient alternative to density-functional theory [76, 77], but with an extended accuracy compared to classical methods. DFTB is suitable for systems that have localized electrons, like covalently bonded hydrocarbons, but have been used succesfully for gold [78]. As an example, compared to DFT calculation parallelized over several processors, DFTB can compute the same system with a single processor much faster. It is suitable for desktop computer use.

Even though DFTB is made much faster than DFT by tight-binding type energy pa-

rameters, it is still a quantum-mechanical approach with quantum-mechanical insight on problems, and is therefore suitable for many kind of use ranging from serious research to testing, searching and educational purposes. Compared to DFT long and demanding MD-simulations are not problematic to do with DFTB.

Theory of DFTB is based on conventional tight-binding approaches. DFTB uses a minimum basis set and local wavefunctions. For periodic systems Bloch waves are used. DFTB takes the electron density to be a sum of neutral atom electron density and a small fluctuation. Based on electron density convention total energy in DFTB is separated into three parts including band structure and repulsive energies, and charge fluctuation-dependent Coulomb energy.

All DFTB energies can be constructed to be dependent on atom pairs and their distances only, which further separates the energies to on-site and inter-site parts. On-site and inter-site energies together with orbital overlaps will be finally parameterized using DFT with LDA approach to a grid, from which energies are interpolated during calculation. Repulsive energy parameterization can be fitted to chosen reference systems giving pair potentials for element pairs. Energy parameterizations are characteristic for tight-binding approaches. Reading tabulated parameters is much faster than solving the forces on every structure optimization or MD-simulation step, as done in DFT.

To define charges that are caused by density fluctuations, DFTB uses the so-called Mulliken analysis. Because of charge fluctuations, DFTB approach must be solved self-consistently. Kohn-Sham equations in DFTB approach include Schrödinger equations in algebraic form, and definitions of the charge and the Hamiltonian. For further details behind DFTB method, see Appendix D.

2.3 Various densities of states and simulated STM-images

Electron density of states (DOS) gives information about the electronic structure. DOS can be drawn from the electron eigenstates applying either Dirac delta function or then Gaussian or Lorenz distribution function at the eigenenergies, i.e. [79]

$$DOS(\varepsilon) = \sum_a \delta^\sigma(\varepsilon - \varepsilon_a) \ , \tag{2.1}$$

where σ denotes broadening if distribution functions are used. Local density of states is position dependent DOS

$$LDOS(r, \varepsilon) = \sum_a f_a \delta^\sigma(\varepsilon - \varepsilon_a) |\Psi_a(r)|^2 \ , \tag{2.2}$$

where f_a is the occupation of the eigenstate Ψ_a.

Integration of LDOS over certain energy range $\int_{\varepsilon_0}^{\varepsilon_1} d\varepsilon$ gives pure position-dependent LDOS, which tells how much states there are in the chosen energy range from ε_0 to ε_1. This is the approach that is used in theoretical scanning tunneling microscopy image calculations [80], and is based on early studies of Tersoff and Hamann [81, 82]. To have a complete theoretical STM-image either constant current or constant height STM method must be imitated. Constant height STM is straightforward, because changes in the integrated LDOS profile can be followed at constant height from the sample. For theoretical constant current STM certain isosurface of the integrated LDOS is chosen and the changes in height of that isosurface are collected. Current defines the relevant value for the isosurface. In practice the electron states that are visible in STM-images, are the outer-most states. Those states interact with the tip and define the main differences in the experimental images, that at the theoretical approach leads to integration of occupied states over an energy range close to Fermi level.

From equation (2.2) it is possible to estimate LDOS for certain atom group; only states that belong to definite atoms are considered. Then for atom I of the group of atoms $\mathcal{R}$ the LDOS can be written

$$LDOS_{\mathcal{R}}(\varepsilon) = \sum_{I\in\mathcal{R}} LDOS(I,\varepsilon) = \sum_{I\in\mathcal{R}}\sum_{a} f_a \delta^{\sigma}(\varepsilon-\varepsilon_a) q_{I,a} \ , \tag{2.3}$$

where $q_{I,a}$ is the charge of atom I contributed by the eigenstate a. Separation of the charge contribution into individual atoms is built into the both methods used in this thesis, DFT and DFTB. So equation (2.3) describes the integrated LDOS of equation (2.2) over the chosen atomic regions Ω_I.

The projected density of states separates the contribution from different angular momentum states into DOS. PDOS can be defined similarly to LDOS for group $\mathcal{R}$ of atoms, but the difference is the fixed angular momentum l of the electron states

$$PDOS_{\mathcal{R}}(l,\varepsilon) = \sum_{I\in\mathcal{R}} PDOS(I,l,\varepsilon) = \sum_{I\in\mathcal{R}}\sum_{a} f_a \delta^{\sigma}(\varepsilon-\varepsilon_a) q^l_{I,a} \ , \tag{2.4}$$

where q^l_I is the charge of atom I contributed from the states with angular momentum l. If the group $\mathcal{R}$ includes all the atoms, equation (2.4) gives $PDOS$ for the whole system; however, it is often desireable to look at a certain group of atoms or individual atoms.

2.4 Symmetries of graphene and carbon nanotubes

Before going to symmetries of graphene and carbon nanotubes, basic definitions of group theory are briefly introduced. The symmetry group G of a system must fulfill

the criteria of a mathematical group [83]. $G = \{a, b, c, \ldots\}$ is a group, if there is a mapping $\circ : G \times G \rightarrow G$ so that the following three properties are valid; (1) mapping of any $a, b, c \in G$ obeys associativity $(a \circ b) \circ c = a \circ (b \circ c)$, (2) there exists an identity element e so that for any $a \in G$ $a \circ e = a$, and (3) there exists an inverse element $a^{-1} \in G$ for all $a \in G$ so that $a \circ a^{-1} = 1$. Subgroup is a set of elements that fulfills the group criteria, but is part of the some other larger group.

Elements of the group can be divided into different conjugacy classes. Elements $a, b \in G$ are conjugate for each other, if there is an element $g \in G$ so that $gag^{-1} = b$. Set of the elements, that are conjugates with each other, are called a conjugacy class. Representation φ of a group G is a linear mapping $\varphi(a) : G \times V \rightarrow V; \mathcal{V} \rightarrow \varphi(a, \mathcal{V})$ that describes how a vector $\mathcal{V}$ in vectorspace V changes under action of the group element a. Sub-representation is a reduced mapping $\tilde{\varphi}$ into a reduced vector space $\tilde{V}$ fullfilling still the requirements of a representation. From all of the possible representations, the irreducible ones are those that have no other sub-representations than the identity and themselves [83].

Characters χ describe the trace of representation matrix of the symmetry group. Character table is the usual way to list the properties of a symmetry group. It consists of irreducible representations in rows and conjugacy classes in columns, furthermore it includes only the irreducible characters. Elements from the same conjugacy class act the same way; they produce same characters for the same representation.

Symmetry element a acting on N-dimensional vector $\mathcal{V}$ (e.g. consisting of basis of N phonons, for example) gives a $N \times N$-dimensional matrix A, which describes the representation and defines the character

$$a\mathcal{V} = A\mathcal{V} \equiv \begin{pmatrix} a_{11} & \cdot & \cdot & \cdot & a_{1N} \\ \cdot & \cdot & & & \cdot \\ \cdot & & \cdot & & \cdot \\ \cdot & & & \cdot & \cdot \\ a_{N1} & \cdot & \cdot & \cdot & a_{NN} \end{pmatrix} \begin{pmatrix} v_1 \\ \cdot \\ \cdot \\ \cdot \\ v_N \end{pmatrix} \; ; \chi = Tr(A) \; . \tag{2.5}$$

For one dimensional irreducible representations, matrix A is just 1×1 -matrix and the character is under any action always ± 1. Connecting this to an physical example of phonons, 1D-phonon $\mathcal{V} = v_1$ under action of any symmetry operation gives always either exactly the same phonon mode $+1 \cdot v_1$ or that with vectors pointing opposite direction $-1 \cdot v_1$. With multiple-dimensional irreducible representations also the dimension of vectors must coincide with the dimension of the representation.

Figure 2.1 shows the graphene plane with geometrical information needed to construct a carbon nanotube out of it. Hexagonal lattice determines the symmetries of graphene and the rolling direction the symmetries of carbon nanotubes. Graphene has symmetry point group of $D_{6h} = D_6 \otimes C_i$ [84]. All the symmetry elements of the point group

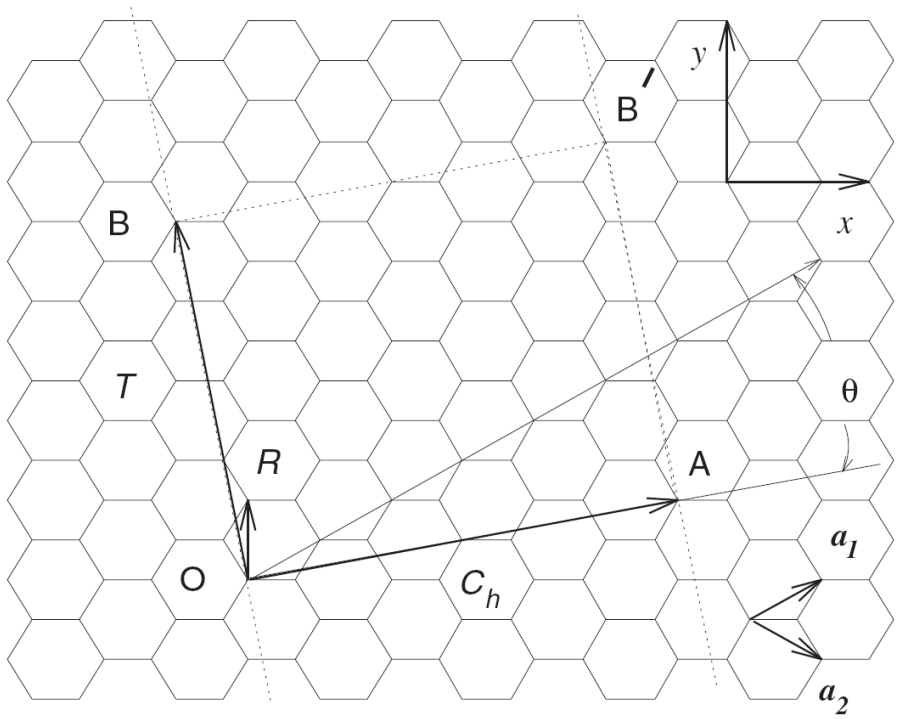

Figure 2.1: Formation of carbon nanotube out of graphene. Square denotes the piece of graphene that will be rolled into tube by connecting B to B' and O to A. Lattice vectors a_1 and a_2 defines the chiral indices (n,m) through the chiral vector $C_h = na_1 + ma_2$, T is the unit cell vector in tube direction. Chiral angle θ can be defined with chiral indices. Taken from Ref. [86].

D_{6h} can be constructed from rotations (C_6, C_2), reflections (σ_h) and inversion (i); rotations and reflections constructing a dihedral subgroup D_6 while inversion i and identity e symmetry subgroup $C_i = \{e, i\}$.

Cutting graphene into a nanoribbon reduces the number of symmetry operators. The highest possible symmetry requires cutting both edges symmetrically into armchair or zigzag nanoribbons. The order of the main rotation axis decreases from C_6 to C_2 and the point group of the highest symmetry armchair and zigzag nanoribbons falls down to D_{2h} [85]. Translation group must be considered to construct the symmetry line group TD_{2h} of an infinite ribbon.

Structural symmetries of single-walled carbon nanotubes can be divided into three

different line groups with respect to chirality indices (n,m) [87]

$$\begin{aligned} &TD_{nh}, \text{ achiral tubes with even n,} \\ &TD_{nd}, \text{ achiral tubes with odd n, and} \\ &TD_{N}, \text{ chiral tubes,} \end{aligned} \tag{2.6}$$

where T refers to translational symmetry group of the tube with respect to the length of the unit cell. Like for graphene, D_{nh} and D_{nd} are point groups both based on the dihedral point group D_n, but with additional σ_h or inversion symmetries, respectively. Instead of the main rotation axis perpendicular to graphene plane, achiral, zigzag and armchair carbon nanotubes have the main rotation axis along the tube axis; secondary C_2 rotation axis in the radial direction.

Symmetry group of one unit cell of chiral tubes can be formed from the Abelian subgroup C_N, for which symmetry operations are translations by vector R on tube surface and C_2 rotations with axes perpendicular to the nanotube axis. Index N equals the number of symmetry operations R needed to go full circle around the tube. This translation symmetry vector R on tube surface is defined to have the minimum rotation of the tube [86]. Figure 2.2 visualizes the symmetry operations existing in chiral and achiral tubes.

A shortened and reduced character table of the line group TD_{nh} for achiral tubes is shown in table 2.1. Main features of the character table coincide with TD_{nd} and TD_N groups as well, remembering the differences in point group elements. Similarities between all of the groups TD_{nh}, TD_{nh}, and TD_N are the rotational dependencies with respect to tube direction and the dependencies of the translations in tube direction. In the next section the relations of the irreducible representations to phonon modes will be introduced.

2.5 Phonons

Phonons describe the small-amplitude motion of nuclei in an atomic system. In conventional DFT and DFTB approaches the Born-Oppenheimer approximation fixes the nuclei and phonons must be solved separately from the curvature of the total energy around a fixed local energy minimum positions of nuclei. The first approximation is

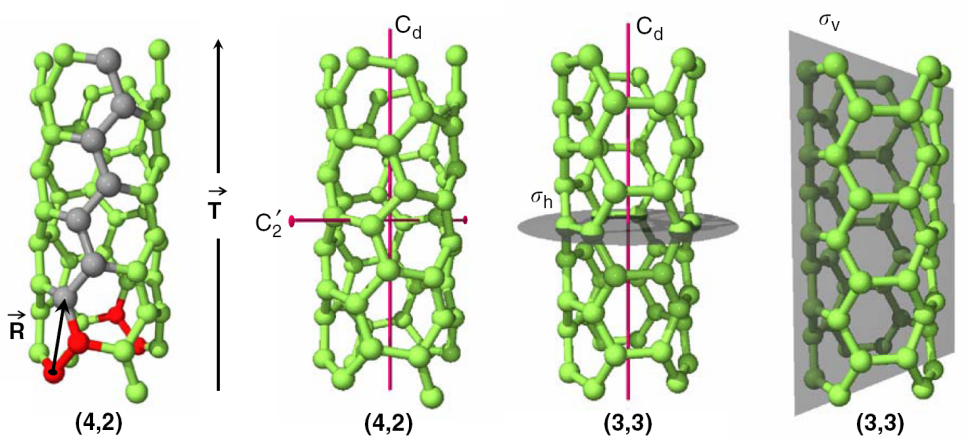

Figure 2.2: Symmetries in the SWCNTs. First two figures on the left show the chiral tube (4,2) with characteristic Abelian subgroup symmetry vector R and rotational symmetry axis C_2' radially through the tube. Another radial rotation axis is labeled usually by C_2'', and if presented, would point through a center of hexagon. In addition there can exist in chiral tubes a pure rotation axis parallel to tube, in this case C_d with $d = 2$. T denotes the unit cell vector for chiral tube (4,2) in tube direction and at the same time corresponds to translational group symmetry vector. Third and fourth figures show the achiral tube (3,3) with horizontal σ_h and vertical σ_ν reflection planes, and the main rotation axis C_d with $d = 3$ in this case. For achiral tubes (n,0) and (n,n) with even n there exist two different kinds of vertical reflection planes σ_ν intersecting hexagon and $\sigma_{\nu'}$ coinciding with carbon bonds. Taken from Ref. [86].

Table 2.1: Character table of line group $T_{2q}D_{nh}$ for achiral nanotubes (n,0) and (n,n). Parameters are defined as follows: unit for rotation angle is $\alpha = 2\pi/2n$, number of translations in tube direction is $t = 0, \pm1, \pm2, \ldots$, angular quantum number is $m = 1, 2, \ldots, (n-1)$, number of rotations is $r = 0, 1, \ldots, (n-1)$, and the wave vector in tube direction is $k \in (0, \pi)$. Inversion is realized with combination of reflection and rotation as $I = \sigma_h C_2$. σ_ν and $\sigma_{\nu'}$ are vertical reflections, σ_h is horizontal reflection, $\sigma_x \in \{\sigma_\nu, \sigma_{\nu'}\}$ satisfy $\sigma_h = C_2'\sigma_x$, C_2' and C_2'' are rotations perpendicular and C_{2n} rotations parallel to tube direction. Dimensions of the irreducible representations can be realized from the coefficients in characters giving dimensions $dim(A) = 1$, $dim(B) = 1$, $dim(E) = 2$, and $dim(G) = 4$. Irreducible representations transforming quadratically due to Cartesian coordinates x, y and z are A_0^+, E_1^- and E_2^+ [88, 89].

	$\left(C_{2n}^{2r}\|t\right)$	$\left(C_{2n}^{2r+1}\|\frac{1}{2}t\right)$	$\left(\sigma_v C_{2n}^{2r}\|t\right)$ $\left(\sigma_x C_{2n}^{2r}\|t\right)$	$\left(\sigma_v C_{2n}^{2r+1}\|\frac{1}{2}+t\right)$ $\left(\sigma_{v'} C_{2n}^{2r}\|\frac{1}{2}+t\right)$	$\left(\sigma_h C_{2n}^{2r}\|-t\right)$ $\left(\sigma_x C_2' C_{2n}^{2r}\|-t\right)$	$\left(\sigma_h C_{2n}^{2r+1}\|-\frac{1}{2}-t\right)$ $\left(\sigma_x C_2'' C_{2n}^{2r}\|-\frac{1}{2}-t\right)$	$\left(\sigma_h \sigma_v C_{2n}^{2r}\|-t\right)$ $\left(C_2' C_{2n}^{2r}\|-t\right)$	$\left(\sigma_h \sigma_v C_{2n}^{2r+1}\|-\frac{1}{2}-t\right)$ $\left(C_2'' C_{2n}^{2r}\|-\frac{1}{2}-t\right)$
${}_0A_0^\pm$	1	1	1	1	±1	±1	±1	±1
${}_0B_0^\pm$	1	1	-1	-1	±1	±1	∓1	∓1
${}_0A_n^\pm$	1	-1	1	-1	±1	∓1	±1	∓1
${}_0B_n^\pm$	1	-1	-1	1	±1	∓1	∓1	±1
${}_0E_m^\pm$	$2\cos(2rm\alpha)$	$2\cos((2r+1)m\alpha)$	0	0	$\pm2\cos(2rm\alpha)$	$\pm2\cos((2r+1)m\alpha)$	0	0
${}_kE_{A_0}$	$2\cos(kt)$	$2\cos(k(\frac{1}{2}+t))$	$2\cos(kt)$	$2\cos(k(\frac{1}{2}+t))$	0	0	0	0
${}_kE_{B_0}$	$2\cos(kt)$	$2\cos(k(\frac{1}{2}+t))$	$-2\cos(kt)$	$-2\cos(k(\frac{1}{2}+t))$	0	0	0	0
${}_kE_{A_n}$	$2\cos(kt)$	$-2\cos(k(\frac{1}{2}+t))$	$2\cos(kt)$	$-2\cos(k(\frac{1}{2}+t))$	0	0	0	0
${}_kE_{B_n}$	$2\cos(kt)$	$-2\cos(k(\frac{1}{2}+t))$	$-2\cos(kt)$	$2\cos(k(\frac{1}{2}+t))$	0	0	0	0
${}_\pi E_{A_0}^{A_2}$	$2(-1)^t$	0	$2(-1)^t$	0	0	0	0	0
${}_\pi E_{B_0}^{B_2}$	$2(-1)^t$	0	$-2(-1)^t$	0	0	0	0	0
${}_kG_m$	$4\cos(kt)\cos(2rm\alpha)$	$4\cos(k(\frac{1}{2}+t))\times$ $\cos((2r+1)m\alpha)$	0	0	0	0	0	0
${}_\pi G_j^{n-j}$	$(-1)^t 4\cos(2jr\alpha)$	0	0	0	0	0	0	0
for even n								
${}_\pi E_{q/2}^\pm$	$2(-1)^{r+t}$	0	0	0	0	0	$\pm2(-1)^{r+t}$	0

to perform a harmonic expansion of potential energy due to atomic displacements x_i

$$\begin{aligned} V =& V_0 + \sum_i \overbrace{\left(\frac{\partial V}{\partial x_i}\right)_0}^{=0} x_i + \frac{1}{2}\sum_{i,j}\left(\frac{\partial^2 V}{\partial x_i \partial x_j}\right)_0 x_i x_j + \dots \\ \approx& V_0 + \frac{1}{2}\sum_{i,j}\underbrace{\left(\frac{\partial^2 V}{\partial x_i \partial x_j}\right)_0}_{=\mathcal{H}_{ij}} x_i x_j \ , \end{aligned} \tag{2.7}$$

where $\mathcal{H}$ is the symmetric Hessian matrix with elements describing the second order derivatives of the total energy with respect to atomic coordinates x_i and x_j. Phonon modes are solved from the equation of motion i.e. Euler-Lagrange equation, which is easy to derive from the Lagrange function $\mathcal{L}$ writing [90]

$$\mathcal{L} = T - V = \frac{1}{2}\sum_i m_i \dot{x}_i^2 - \frac{1}{2}\sum_{i,j}\mathcal{H}_{ij} x_i x_j \ . \tag{2.8}$$

The Euler-Lagrange equation with respect to nuclei displacements $x_1, x_2, ..., x_N$ is then

$$\frac{d}{dt}\frac{\partial \mathcal{L}}{\partial \dot{x}_i} - \frac{\partial \mathcal{L}}{\partial x_i} = 0 \Rightarrow \sum_j (\mathcal{H}_{ji} x_j + \delta_{ij} m_i \ddot{x}_i) = 0 \ . \tag{2.9}$$

Atomic displacements x_i can be described due to Cartesian coordinate $i \in \{x, y, z\}$ with ansatz $x_i = v_i \exp[i(-\omega t + \delta)]$; v_i denoting amplitude, δ possible phase difference and ω frequency. Generalization of the expression for 3N-dimensional vectors including all of the nuclei leads to the final form of the equation of motion

$$\mathcal{H}\mathbf{v}_\mu = \omega_\mu^2 \mathcal{M}\mathbf{v}_\mu \ , \tag{2.10}$$

where $\mathcal{H}$ is the 3N×3N Hessian matrix defined in equation (2.7), $\mathcal{M}$ is a 3N×3N diagonal mass matrix, and ω_μ is the eigenfrequency and $\mathbf{v}_\mu$ 3N-dimensional eigenvector for phonon μ.

2.5.1 Raman-active modes

Phonons are vector space components assigned to atoms, classifiable into irreducible representations of the symmetry group of the system. Raman-active modes transform quadratically with respect to Cartesian coordinates e.g. xx, yy, zz, xy, xz, yz and must induce a change in the polarizability of the system. These conditions yield the general non-zero transition moment integral condition, $\int \Psi_i \alpha \Psi_f \neq 0$, where α is the polarizability tensor, Ψ_i initial ground state and Ψ_f final excited state [91].

In single-walled carbon nanotubes Raman-active modes belong to irreducible representations ${}_{(0)}A_0^+$, ${}_{(0)}E_1^-$ and ${}_{(0)}E_2^+$ in the line group notation of A_{1g}, E_{1g}, and E_{2g} in the molecular notation. From now on, lower-left corner indices related to wave vector in tube direction are neglected referring to $k = 0$ case. From these representations, A is one- and E two-dimensional, and consistently E symmetric phonon modes include two degenerate individual normal modes. Superscripts + and − describe the symmetry of the mode with respect to horizontal reflection, − for eigenvectors changing direction and + for unchanged direction under reflection [89, 92]. For chiral tubes there is no horizontal reflection and therefore superscripts are left out. In single-walled carbon nanotubes Raman-active modes can be divided into three different decompositions, based on symmetry groups [86, 93]

$$\begin{aligned}\Gamma_{\text{zigzag}} =& 2A_0^+ + 3E_1^- + 3E_2^+ \\ \Gamma_{\text{armchair}} =& 2A_0^+ + 2E_1^- + 4E_2^+ \\ \Gamma_{\text{chiral}} =& 3A_0 + 5E_1 + 6E_2 \ .\end{aligned} \tag{2.11}$$

Chiral tubes are less symmetric, which increases the number of Raman-active modes with respect to zigzag and armchair tubes. Low energy modes have 1/diameter dependence, from which the most intensive is the radial breathing mode (RBM) A_0^+ (A_{1g}). Other important Γ-point modes are the three (for chiral tubes six) high-energy modes responsible for G-band; one from each Raman-active symmetry. Due to resonant effects and 1/diameter-dependence, these modes are more useful for structural detection than others. Figures 2.3 and 2.4 show the Raman-active modes for armchair and zigzag tubes, from which the most important are labeled with RBM and G-band. Raman-active modes of the chiral tubes are a combination of the both of the modes in figures 2.3 and 2.4.

An example of experimental Raman spectrum is shown in figure 2.5 showing the assignments for different characteristic bands. RBM-band and G-band initiate from first-order scattering at Γ-point. D-band is also called the defect-band and includes scattering of electrons due to defects, which makes it therefore second-order scattering away from Γ-point. Overtone bands like G'-band (overtone of D-band) are due to second-order scattering with two phonons and the energy is correspondingly the sum of the energies of the involved phonons. The different scattering processes are discussed in the following section.

Numerically Raman-active modes can be identified using well-known dependencies under symmetry element action according to character table 2.1. In numerical procedure, as a first assumption, all of the phonon eigenmodes are one-dimensional. By acting with symmetry operations like rotations on the system and phonon eigenvectors, the specific characters can be solved through equation 2.5. If the character does not obey the one dimensional behavior i.e. if $\chi \neq \pm 1$, the 1D-assumption is corrected. Next, the phonon is considered as the first one of the degenerate two-dimensional

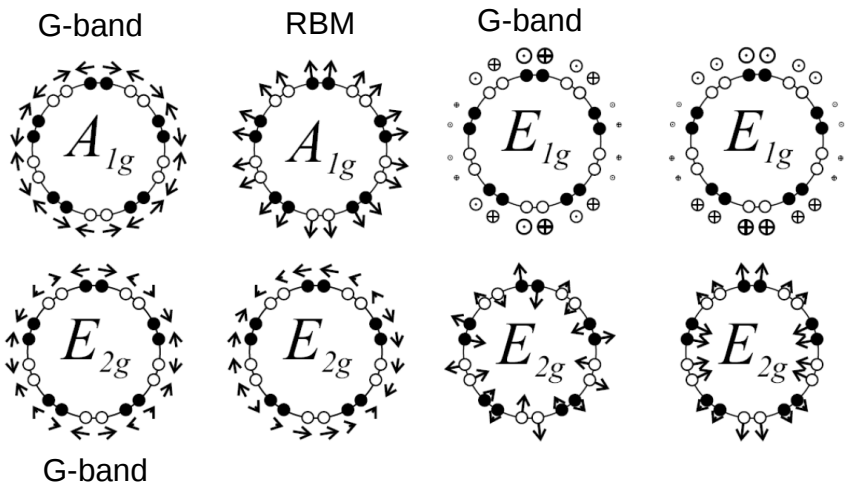

Figure 2.3: Raman-active modes of armchair tubes. Experimentally essential modes are labeled, responsible for RBM or G-band. Atoms in different level in tube direction are separated with filled and empty circles. Arrows describe the eigenvectors in circumferential and radial direction, and circles with dot and cross eigenvectors in tube direction upwards and downwards, respectively. From the degenerated 2D modes only one is shown. All the modes are uniform in tube direction characteristic for Γ-point modes. Taken from Ref. [89].

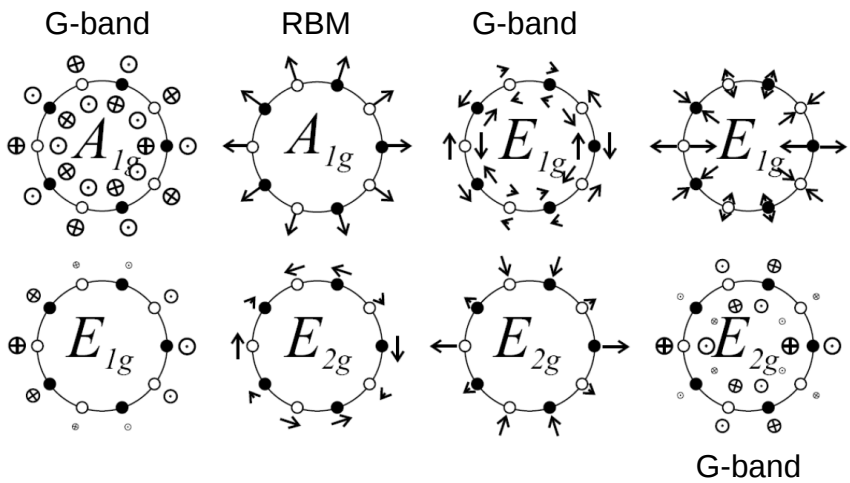

Figure 2.4: Raman-active modes of zigzag tubes. The conventions of figure 2.3 are used, except now the direction of the eigenvectors for the atoms on top of each other may alternate. Symbols outside the tube circumference denote the eigenvectors for uppermost atoms and symbols inside the tube circumference denote eigenvectors for atoms below them. Taken from Ref. [89].

phonon mode. To construct the full basis for the 2D-phonon with both degenerate eigenmodes, the phonons next in energy are tried, which works usually well because of the equilibrium conditions. The same procedure is gone through for 2D-assumption as for 1D-assumption; calculation of the characters for specific symmetry operations through equation 2.5 is repeated. Going through all of the modes separates the desired symmetries A_0^+, E_1^-, and E_2^+.

Although graphene has the same symmetry group as some of the achiral tubes, decomposition gives only two Raman-active E_{2g} symmetric Γ-point modes [84, 94]. The modes include one low-energy mode and one high-energy mode responsible of G-band in graphene. Reduction in the number of Raman-active modes compared to SWCNTs can be understood with lower dimensionality and simple hexagonal lattice, which makes the graphene effectively more symmetric. Because of the simple two-dimensional structure, the vibrational mode decomposition in Γ-point is already very different from carbon nanotubes including only 12 modes, from which nine are optical with $\Gamma_{opt} = 2E_{2g} + E_{1g} + 2B_{2g} + A_{2u}$ [84].

For graphene nanoribbons, the number of Raman-active modes is increased compared to graphene, because the number of symmetries is decreased. In the highest possible symmetry point group of graphene nanoribbons, D_{2h}, there can only exist 1D irreducible representations and thus 1D-phonons. Raman-active modes belong

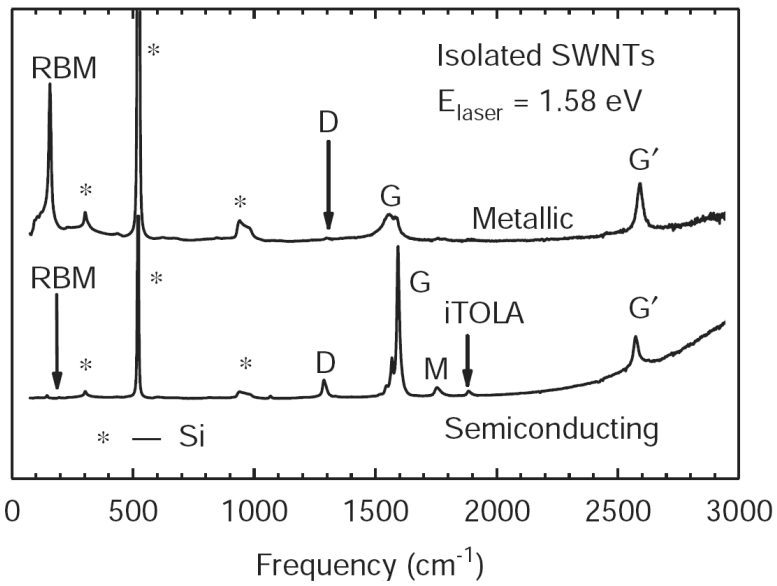

Figure 2.5: Experimental, resonant Raman spectrum of metallic and semiconducting, isolated single-wall carbon nanotube representing all the relevant bands, among others RBM- and G-band. Taken from Ref. [11].

to irreducible representations A_g and B_g due to group theory. Instead of infinite 2D-structure, graphene nanoribbons are infinite only in one dimension, which makes them more comparable to SWCNTs. Because of the finite structure, for example breathing modes of the ribbon width can exist as RBM in SWCNTs. Also the edge makes the system different by breaking the uniform bonding properties, making edge-localized modes possible.

2.6 Raman spectroscopy

Research of nanomaterials has its complications due to the small size. Raman spectroscopy is one of the basic tools for structural detection and can give information about relatively small differences in samples through phonons. Experimental Raman measurements includes resonant effects, which were discussed in the Introduction in connection with the figure 1.3. Resonant approach is therefore preferable starting point also for accurate computations.

Raman scattering process consists of: (1) coupling of laser light with electrons, i.e. excitation of electrons, (2) coupling of excited electrons with phonons, i.e. scattering of electrons with the phonons, and (3) coupling of scattered electrons with photons, i.e. emission of out coming photons [11]. After scattering, the out-coming photons are measured, which gives information about the phonons that were excited and further about the structural properties. Resonant enhancement exists when the incoming or out-coming photon matches with an optical singularity of the system. In other words, electronic transitions between real states give bigger intensity where van Hove singularities give an impact in 1D-systems, like carbon nanotubes. Collection of the possible scattering processes are shown in figure 2.6, including first- and second-order scattering.

Resonant calculations consider often ideal systems, which makes the problem simpler in many ways, because the number of relevant phonons and the size of the system can be diminished. Simplifications can also be used, for example the electron-phonon coupling in carbon nanotube has been determined utilizing graphene. Defects make everything more complicated; reasonable construction of defective systems requires taking into account many atoms more than in ideal systems. Also another advantage is lost as the analytical solutions of ideal systems may not be valid anymore. After all, the relevant number and the shape of the phonons may not be the same.

A good starting point in investigations of Raman spectra of defective systems theoretically is to look the Raman-active modes and their changes due to defects. To have a grasp of the Raman-active modes in defective systems, full resonant description is not necessarily needed at first. Raman-active modes have the property of changing

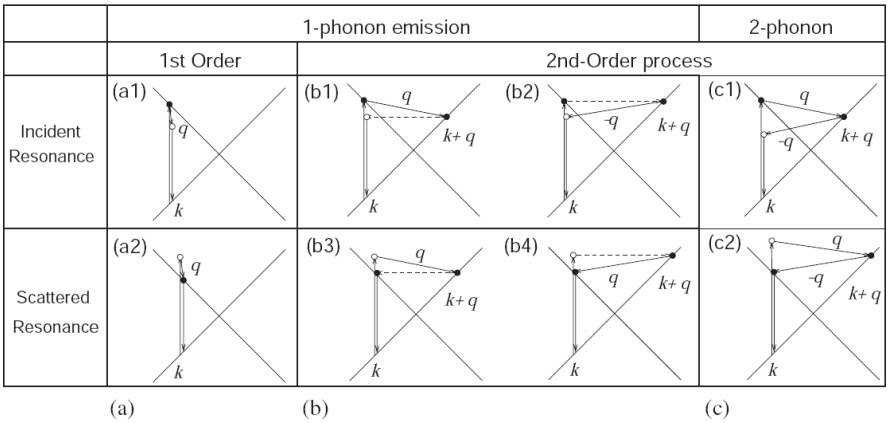

Figure 2.6: Schematic description of different Raman scattering processes, first-order scattering in (a), second-order scattering including one phonon in (b), and second-order scattering with two phonons in (c). The first row describes the incident resonant condition, where excitation of electrons is between real valence (lower lines) and conduction band (upper lines) states, but the scattering of electrons back to initial state, due to the emission of out-coming photons, is from artificial state. The second row describes the same but in the case of scattered resonance. Taken from Ref. [11].

the polarizability of the system, which gives one possibility to proceed, and this is the approach used in this thesis. Details of resonant Raman calculations are left into the Appendix E.

2.6.1 Non-resonant empirical bond-polarization method

Non-resonant bond-polarization theory uses static empirical polarizability parameters for individual bonds to estimate the Raman intensity of different modes. It does not describe the full scattering process and resonant effects, but can be used to investigate effects of different defects for Raman-active modes at the Γ-point. Related to carbon nanostructures, these modes are responsible of the RBM- and G-band for SWCNTs and graphene. Although resonant calculation gives comparable spectra to experiments, non-resonant calculations can still give the information about the changes in Raman-active modes in the systems that are either computationally too expensive or not sufficiently known to be calculated with resonant description.

The grounds of non-resonant bond-polarization theory are in static electronic polarizability description. It postulates that the full static electronic polarizability of the system can be expressed as a sum of individual bond-polarizabilities. Another assumption is the independency of the individual bond-polarizabilities on their chemical

environment. For a given bond of an atom pair the polarizability can be written as [95]

$$\Pi_{ij} = \frac{1}{3}\left(\alpha_1 + 2\alpha_2\right)\delta_{ij} + \left(\alpha_1 - \alpha_2\right)\left(\frac{R_i R_j}{R^2} - \frac{1}{3}\delta_{ij}\right), \tag{2.12}$$

where subscripts i and j denote Cartesian coordinates and $\mathbf{R}$ is the vector connecting the two neighboring atoms. $\alpha_1 + 2\alpha_2$ describes the isotropic and $\alpha_1 - \alpha_2$ anisotropic contribution, with α_1 and α_2 giving the polarizability parameters in parallel and perpendicular directions to the bond. Mean static polarizability of the system can be written as $\bar{\alpha} = \frac{1}{3}\left(\alpha_{xx} + \alpha_{yy} + \alpha_{zz}\right)$, which is the sum of individual mean bond-polarizabilities $\bar{\Pi} = \frac{1}{3}\left(\Pi_{xx} + \Pi_{yy} + \Pi_{zz}\right) = \frac{1}{3}\left(\alpha_1 + 2\alpha_2\right)$.

As was mentioned in section 2.5.1, Raman-active modes tend to the change polarizability of the system. In the non-resonant bond-polarization method the change in polarizability is determined as a sum of individual bond-polarizability changes with respect to atomic displacements $\tilde{R}$; and are related to actual phonon eigenvectors v_μ. Taking the product of the phonon eigenvectors and the derivatives of bond-polarizability, the change in total polarizability of the system due to phonon μ is [95]

$$\begin{aligned} P'_{\mu,ij} &= \sum_l \left[\frac{\partial \Pi_{l,ij}}{\partial \tilde{R}_l}\right]_0 \mathbf{v}_\mu(l) \\ &= -\sum_l \sum_b \Bigg(\left(\frac{\alpha'_1 + 2\alpha'_2}{3}\right) \mathbf{R}_0(l,b)\cdot \mathbf{v}_\mu(l)\delta_{ij} \\ &\quad + \left(\alpha'_1 - \alpha'_2\right)\left(R_{0i}(l,b)R_{0j}(l,b) - \frac{1}{3}\delta_{ij}\right)\mathbf{R}_0(l,b)\cdot \mathbf{v}_\mu(l) \\ &\quad + \left(\frac{\alpha_1 - \alpha_2}{R_0(l,b)}\right)\left(R_{0i}(l,b)v_{\mu,j}(l) + R_{0j}(l,b)v_{\mu,i}(l) - 2R_{0i}R_{0j}\mathbf{R}_0(l,b)\cdot \mathbf{v}_\mu(l)\right)\Bigg), \end{aligned} \tag{2.13}$$

which includes the assumption that the bond-polarizabilities depend only on the bond length. The first sum in equation (2.13) goes over atoms l and the second over the bonds of atom l. $\mathbf{R}_0(l,b)$ is the equilibrium bond vector and $\mathbf{v}_\mu(l)$ is the eigenvector at the atom site l. Indices i and j denote Cartesian coordinates with respect to incident and scattered light polarizations.

Three different empirical polarization parameters are needed and the values used here, $\alpha'_1 + 2\alpha'_2 = 4.7$ Å^2, $\alpha'_1 - \alpha'_2 = 4.0$ Å^2 and $\alpha_1 - \alpha_2 = 0.04$ Å^3, are adapted from Ref. [96]. For carbon nanotubes and graphene, the estimation of the polarizability parameters is rather easy, because all the bonds have the same bond order. In the original description for fullerenes, more parameters had to be taken into account as there exists both single and double bonds. Parameters for fullerenes were determined based on model molecules with similar bonding properties such as hydrocarbons like ethane

Table 2.2: Bond-polarizability parameters for different carbon-related molecules [96].

Molecule	Bond	$\alpha_1 + 2\alpha_2$ (Å^3)	$\alpha_1 - \alpha_2$ (Å^3)	$\alpha_1' + 2\alpha_2'$ (Å^2)	$\alpha_1' - \alpha_2'$ (Å^2)
CH_4	C–H	1.944			
C_2H_6	C–C	2.016	1.28	3.13	2.31
C_2H_4	C=C	4.890	1.65	6.50	2.60
C_{60}	C–C		1.28	2.30 ± 0.01	2.30 ± 0.30
	C=C		0.32 ± 0.09	7.55 ± 0.40	2.60 ± 0.36
C_{60}	C–C		1.28 ± 0.20	1.28 ± 0.30	1.35 ± 0.20
	C=C		0.00 ± 0.20	5.40 ± 0.70	4.50 ± 0.50
SWCNT	C=C		0.04	4.7	4.0

and ethylene. Parameters for SWCNTs are determined using interpolation based on parameters of the fullerenes. Interpolated parameters are adjusted to describe sensibly the Raman spectra of randomly oriented SWCNT, for which relative intensities will hold well with respect to changes in polarizabilities. In that sense, the static bond-polarizability approach with uniform tube parameters works also as a good approximation for systems with minor defects. Only the lowest E_2^+ mode is known to be sensitive to polarizability parameter $\alpha_1 - \alpha_2$, which is not responsible for the most important experimental RBM- or G-bands. Table 2.2 lists the parameters for different carbon materials.

The total non-resonant first-order scattering Raman (Stokes) intensity for incident and scattered light directions is a sum of single bond-polarizability derivatives, equation (2.13), weighted by the factors depending on the mode energy [95]

$$I_{ij}(\omega) = C \sum_{\mu=1}^{3N} \frac{\langle n(\omega_\mu)\rangle + 1}{\omega_\mu} |P'_{\mu,ij}|^2 \delta(\omega - \omega_\mu), \tag{2.14}$$

where $\langle n(\omega_\mu)\rangle = (\exp(\beta\hbar\omega_\mu) - 1)^{-1}$ is the thermal occupation of mode μ, and the dependence on incident and scattered light frequencies is embedded in the constant C. For zero temperature thermal occupation is then zero. Instead of Dirac delta function $\delta(\omega - \omega_\mu)$ also broadening with Lorentzian distribution can be used, similarly to description in section 2.3 for electron density of states.

2.7 Nudged elastic band method

Molecular dynamics (MD) simulations are one possibility to investigate diffusion. Uncertainty in MD-simulations – if anything happens in a reasonable timescale — em-

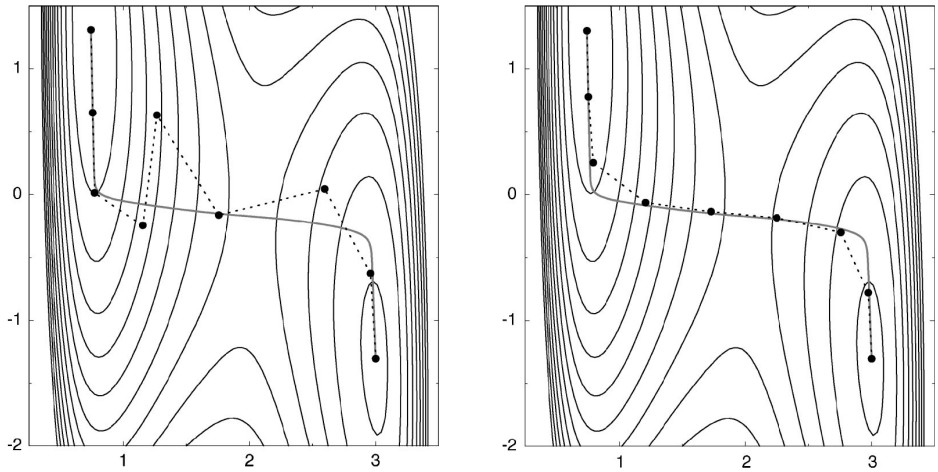

Figure 2.7: An example of the conditions for initial guess (left) and the optimized minimum energy path (right) drawn within the equipotential curves. In the middle of the path there is a saddle point, and the initial and final states are fixed into local energy minima. Each sphere denotes one state of the system on the path. Taken from Ref. [97].

phasize the use of direct diffusion barrier methods. The nudged elastic band method (NEB) [97] can be used to find a minimum energy path (MEP) between given initial and final states of the system, which is suitable for direct diffusion barrier calculations.

The state with the highest energy along the MEP gives the transition state and defines the barrier for the transition process. Energy barrier can be connected to actual transition rate through Arrhenius equation [98, 99]

$$\nu_{process} = \nu_{trial} \exp\left(\frac{-E_b}{k_B T}\right) \ , \tag{2.15}$$

where $\nu_{process}$ is rate for diffusion (or any other transition process), ν_{trial} is the trial rate, E_b is the energy barrier for the transition process, and T is the temperature. In other words, Arrhenius equation describes the chemical reaction rate dependency on temperature and activation energy, which is observed to behave in many occasions exponentially. At high temperatures, the reaction rate is closer to the trial rate, while at very low temperatures, only few of the trial attempts really leads to the transition. Depending on the transition process, the trial rate can be estimated from the vibrational frequencies in the system. Because diffusion and reconstruction processes are usually local transitions, for which bond stretching vibrations are relevant, the trial rate is approximated from the highest vibrational frequencies.

Coming back to the diffusion barrier estimation, the NEB process starts by optimizing the initial and final structures, after which they will be fixed. The process continues by

guessing the diffusion path with a discrete set of images, from which the first natural choice is to take linear interpolation between the initial and final states. By adding spring interactions between the images, the discrete states along the diffusion path become connected, namely the elastic band. In addition to forces from the added spring interactions in the parallel direction, the true forces are included in the perpendicular direction to the elastic band.

The role of the two force components is the following: the spring force ensures equal spacing between the images, while the true force will drive the path into the minimum energy "valley" in the optimization process. Projection into parallel and perpendicular forces to the elastic band can be then understood as "nudging". Vectors to the two neighboring images define the tangent of the band for every discrete image. Visualization of the NEB process is shown in figure 2.7 with the initial guess on the left and the optimized minimum energy path on the right, both on top of the equipotential curves. From MEP, the energy barrier for diffusion can be estimated, which is defined by the saddle point in the example of the figure 2.7.

Defining the tangent for each image is critical, because tangent defines also the direction of the elastic band and the forces. The NEB method relies on one intuitive fact: optimization of the MEP is easiest to start from the high potential, near the saddle point. The same idea is implied in the approximation used to define the tangents: the direction of the tangent is always more reliable to estimate to the neighboring image higher in energy e.g. closer to the saddle point.

The tangent can be defined comparing potentials of the neighboring images. If the potential curve between images $i-1$, i and $i+1$ is continuously increasing or decreasing, the tangent can be written as

$$\tau_i = \begin{cases} \tau_i^+ & ; V_{i+1} > V_i > V_{i-1} \\ \tau_i^- & ; V_{i+1} < V_i < V_{i-1} \end{cases} , \tag{2.16}$$

where $\tau_i^+ = R_{i+1} - R_i$ and $\tau_i^- = R_{i-1} - R_i$. If there is a local energy minimum or maximum between the images $i-1$ and $i+1$, e.g. $V_{i+1} < V_i > V_{i-1}$ or $V_{i+1} > V_i < V_{i-1}$, the tangent is defined as a weighted combination of the τ_i^+ and τ_i^-

$$\tau_i = \begin{cases} \tau_i^+ \Delta V_i^{max} + \tau_i^- \Delta V_i^{min} & ; V_{i+1} > V_{i-1} \\ \tau_i^+ \Delta V_i^{min} + \tau_i^- \Delta V_i^{max} & ; V_{i+1} < V_{i-1} \end{cases} , \tag{2.17}$$

where the weight is connected to the differences in the potentials $\Delta V_i^{max} = \max\{|V_{i+1} - V_i|, |V_{i-1} - V_i|\}$ and $\Delta V_i^{min} = \min\{|V_{i+1} - V_i|, |V_{i-1} - V_i|\}$. This gives always the maximum weight for the tangent that is defined using the neighboring image higher in energy and closer to saddle point.

The unit vector $\hat{\tau}_i = \tau_i / |\tau_i|$ of the tangent in the equations (2.16) and (2.17) connects the directions of the forces. The spring force parallel to tangent is simply

$$F_i^{spr}|_{\parallel} = k \left(|R_{i+1} - R_i| - |R_i - R_{i-1}| \right) \hat{\tau}_i \ , \tag{2.18}$$

where k is the spring constant. The true force perpendicular to the tangent is given by the gradient of the potential

$$\nabla V(R_i)|_{\perp} = \nabla V(R_i) - \nabla V(R_i) \cdot \hat{\tau}_i \ . \tag{2.19}$$

The total force for an image is the sum of forces in equations (2.18) and (2.19)

$$F_i = F_i^{spr}|_{\parallel} - \nabla V(R_i)|_{\perp} \ . \tag{2.20}$$

To optimize the diffusion path, conventional structure optimization algorithms can be used; in this thesis the FIRE-algorithm [100] has been used.

3 Results

3.1 Raman spectra of single-walled carbon nanotubes with vacancies

To have an effect, the effective size of the defect must go hand in hand with the length scale of the phenomenon producing the measured observable. To simplify this with a non-physical example, if one is measuring the population of the whole world, taking one human away does not affect the result. But on the contrary, if the number of students in classroom, for instance, is measured, one missing person already makes the difference. One fundamental property affecting the effective size is the compatibility of the symmetries of the defects and the observable. Continuing with the classroom example; the effect increases immediately, if the missing student should have given the presentation of the day.

In article I these properties of defects are realized in a more physical example – Raman spectra of single-walled carbon nanotubes with vacancies. Vacancies are one of the easiest point-defects to construct and are therefore suitable to start with. Although carbon nanomaterials are reported to anneal themselves [25], results give general knowledge about the effects of point defects on phonon modes of SWCNTs, and verifies the sensibility of structural characterization.

Figure 3.1 shows the non-resonant Raman spectra for various different vacancy configurations calculated with DFTB-method, Section 2.2, and phonon convention described in 2.5. The size of the individual vacancy is small, which induces the biggest changes into the high-energy phonon modes with short wavelengths. Vacancies make the structural strength of the tube decrease, which lowers the energies of both the longitudinal and the circumferential high-energy modes. In general, none of the energies of Raman-active modes increase considerably compared to original non-defective tube mode energies.

Changes and behavior of the defective tube modes can be explained by the symmetries of defects with respect to the symmetry of the phonon. If the symmetries of the defects break considerably the symmetries of the original Raman-active modes, the Raman spectrum is also changed, because the original Raman-active mode can not exist in the same form in the defective tube. Unifying the symmetry breaking with the classroom

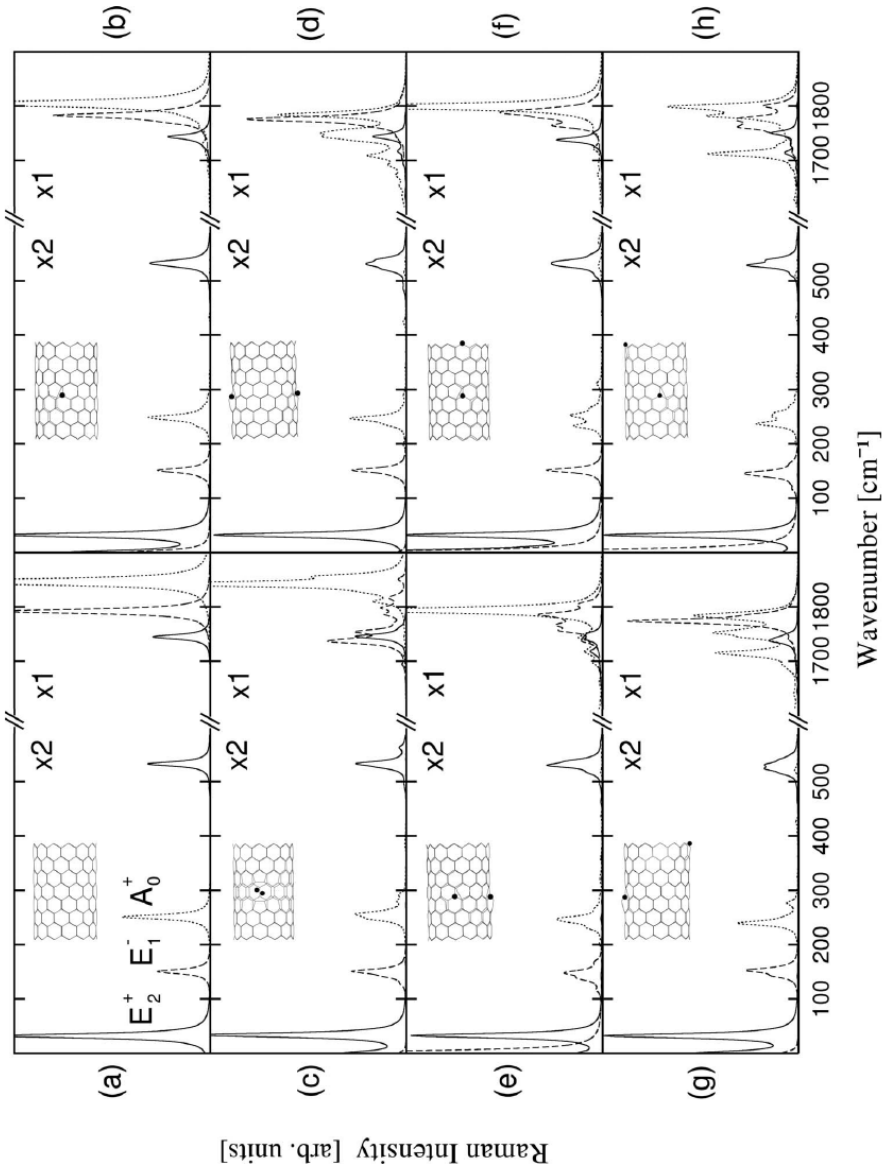

Figure 3.1: Raman-active spectra for uniform periodic (13,0) and (13,0) tubes with different vacancy systems. Dotted line denotes zz (A_0^+), dashed line xz (E_1^-) and solid line xy (E_2^+) incident/scattered light polarizations (symmetries). The spectra are Lorentz-broadened with FWHM= 5 cm^{-1}, which produces observation limit close to the experimental one. Compared to ideal tube, the energies generally drop because single vacancies make the structures weaker. Symmetry compatibility between the defects and the phonons can also be realized. Taken from paper I.

example, vacancies can be thought to be the missing class student, that should give their own important contribution to the presentation — for the motion in phonons. Considering high-energy modes, diversity in the nodal structure of the E_2^+ symmetric mode makes it more stable under defects than E_1^- and A_0^+ symmetric modes. As a reminder, you can check the details of the modes from the section 2.5.1.

The size compatibility become visible on the lowest energy modes, which remain untouched under considerably large defect concentrations compared to high-energy modes due to their collective motion characteristics. Collective motion of the atoms does not get disturbed by small local deformations, because the energy of the phonon is related to motion of a big group of atoms. As the number of defects is increased in the system, changes on the low energy modes are also more probable. Adjacent point-defects merge effectively into a bigger point defect or defective section in the tube and at the same time the effective size gets closer to the range of collective motion. Symmetries play also role for multiple point-defect systems e.g. making the strength of the tube circumferentially imbalanced throughout the tube length breaks the symmetry of the radial breathing mode, which must go through severe changes.

The biggest overlap between the modes of the uniform and defective tube modes gives information about the mode that most probably corresponds to the original Raman-active mode. Based on the overlaps, measuring the similarity between the phonon eigenmodes, the effective size of the defects seen by the original phonon can be estimated. Comparison of the average amplitudes within distances from the defect determines the effective size i.e. the limit, after which the original uniform tube eigenvectors coincide with the defective tube eigenvectors of the phonons with the biggest overlap. Beyond a certain distance the modes cannot be distinguished from their amplitudes. To make this effective size estimation reasonable, the phases of two distinct modes must be the same, which can be adjusted using symmetry operations of the system.

The effective size of the vacancies is the biggest for the high-energy modes as expected, and can be very close to zero for collective low energy modes. Figure 3.2 shows an example of the effective size estimation for Raman-active high-energy mode E_1^-. At the same time it represents one of the largest observed effective sizes for a single vacancy. None of the effective sizes for the tube with a single vacancy exceeded 10 Å. It is good to note that although the size estimation is approximative, it supports both the symmetry and size effect interpretations.

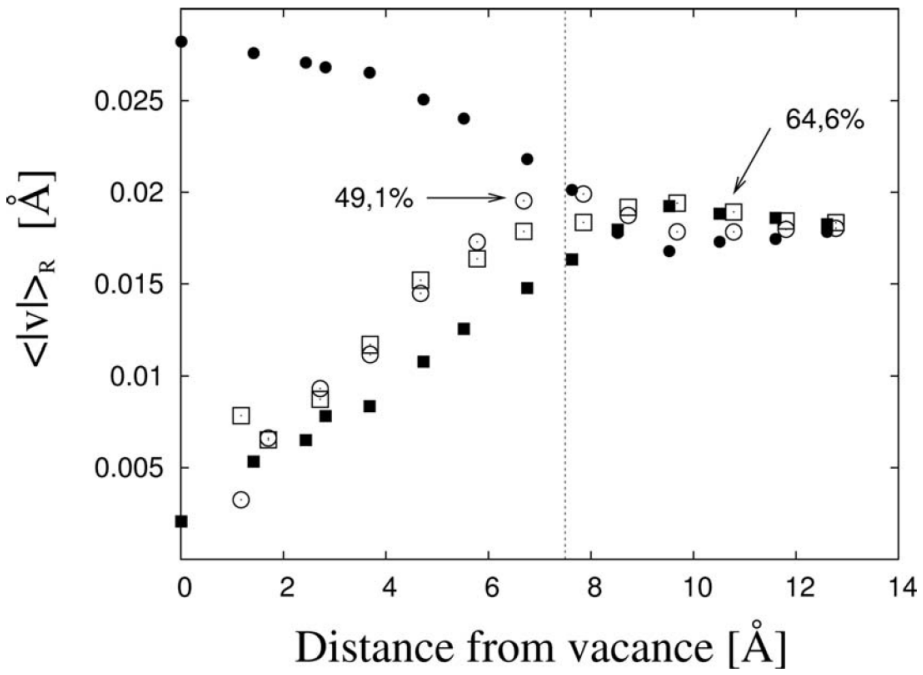

Figure 3.2: Averaged magnitude of the vibrations inside different distances from vacancy for the highest E_1^- symmetry corresponding modes in Fig. 3.1(b) type of one vacancy system (empty symbols). Percentages denotes maximum overlap for both represented vacancy modes with respect to original degenerate E_1^- mode in uniform tube (filled symbols). Dotted line shows the radius inside of which the vacancy considerably affects the motion of the atoms. Taken from paper I.

3.2 Effect of bending on Raman active vibration modes of carbon nanotubes

Bending is a very common mechanical deformation. Effects of bending on Raman-active phonon modes in SWCNTs are investigated in article II. Changes in modes can be understood by considering changes in bond strengths, being stronger in inner and weaker in outer part of the bending. This problem does not get directly reduced into behavior under pure compression or stretch, which would make the energy of all of the modes either increase or decrease. Because bond strengths are not constant throughout the tube, but change continuously along the circumference, different modes behave differently and both decreasing and increasing energies with respect to bending exist.

The first computational problem in investigation of bending is to introduce it in the first place. In investigation of phonons, fixing atoms is not possible, because that makes the effects of bending to be wiped out by the effects of fixed atoms themselves. Continuous periodic bending conditions are desired with totally freely moving atoms. One nice option to bend a system without any constraints is to consider wedge boundary conditions shown in figure 3.3, which we developed in this work.

Periodic images are added by rotation and the shortest distance, considering also periodic images, defines the vector between the atoms. In classical mechanics this is already enough for a working scheme. In quantum mechanics choosing the direction of the quantization axis causes extra problems. Requiring that the direction of the quantization axis changes symmetrically under rotations due to the periodic wedge boundaries, also quantum mechanical calculations are accurate for any system. For DFT-method described in the Section 2.1 and Appendix A these boundary conditions could be more difficult to apply than for DFTB, that was chosen for all of our Raman studies and introduced in the Section 2.2 and Appendix D.

For carbon nanotubes with relatively small bending angles the approximative approach is suitable, because of the structural stiffness and complex bond interface at the boundaries. Approximation divides the error that is made in an improper direction of quantization axis in periodic images between the two boundaries. Forces and energies are not exact near the boundaries, but do not depend anymore on the boundary on which they are calculated. In general, the error caused by quantization axis is relatively small and does not affect the shape or the optimized length of the bent tubes.

Bending breaks the symmetry along the circumference of the tube. In contradiction to the symmetry breaking due to the vacancies described in section 3.1, this breaking is continuous. Instead of the uniform interaction strength distribution, bond strength

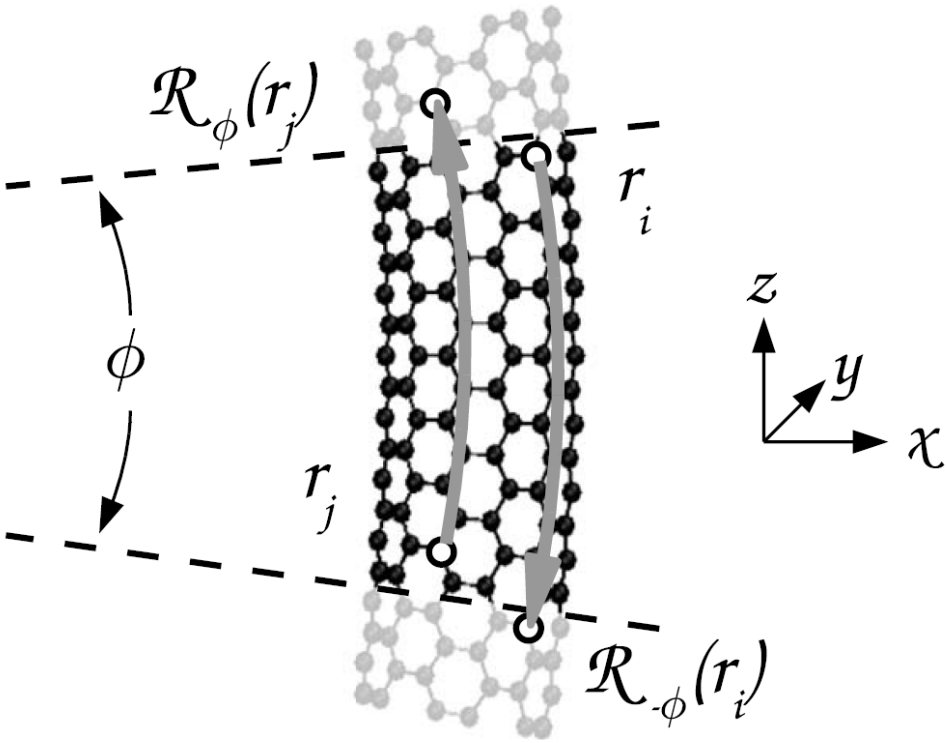

Figure 3.3: Schematic of the wedge boundary condition. Wave functions satisfy $\psi(\mathbf{r}_B) = \psi(\mathcal{R}_{\pm\phi}(\mathbf{r}_B))$, where $\mathbf{r}_B$ is a point on either boundary (with one **k**-point along tube axis); operation $\mathcal{R}_{\pm\phi}(\mathbf{r}_j)$ rotates $\mathbf{r}_j$ an angle $\pm\phi$ around the wedge apex. We define the vector $\mathbf{r}_{ij}$ from atom i to atom j as equal to shortest of vectors $(\mathcal{R}_{\phi}(\mathbf{r}_j) - \mathbf{r}_i)$, $(\mathcal{R}_{-\phi}(\mathbf{r}_j) - \mathbf{r}_i)$ or $(\mathbf{r}_j - \mathbf{r}_i)$, where $\mathbf{r}_i$ and $\mathbf{r}_j$ are atom positions within the simulation box. For some atom pairs $\mathbf{r}_{ij}$ crosses the boundary and renders Newton's third law invalid. Taken from paper II.

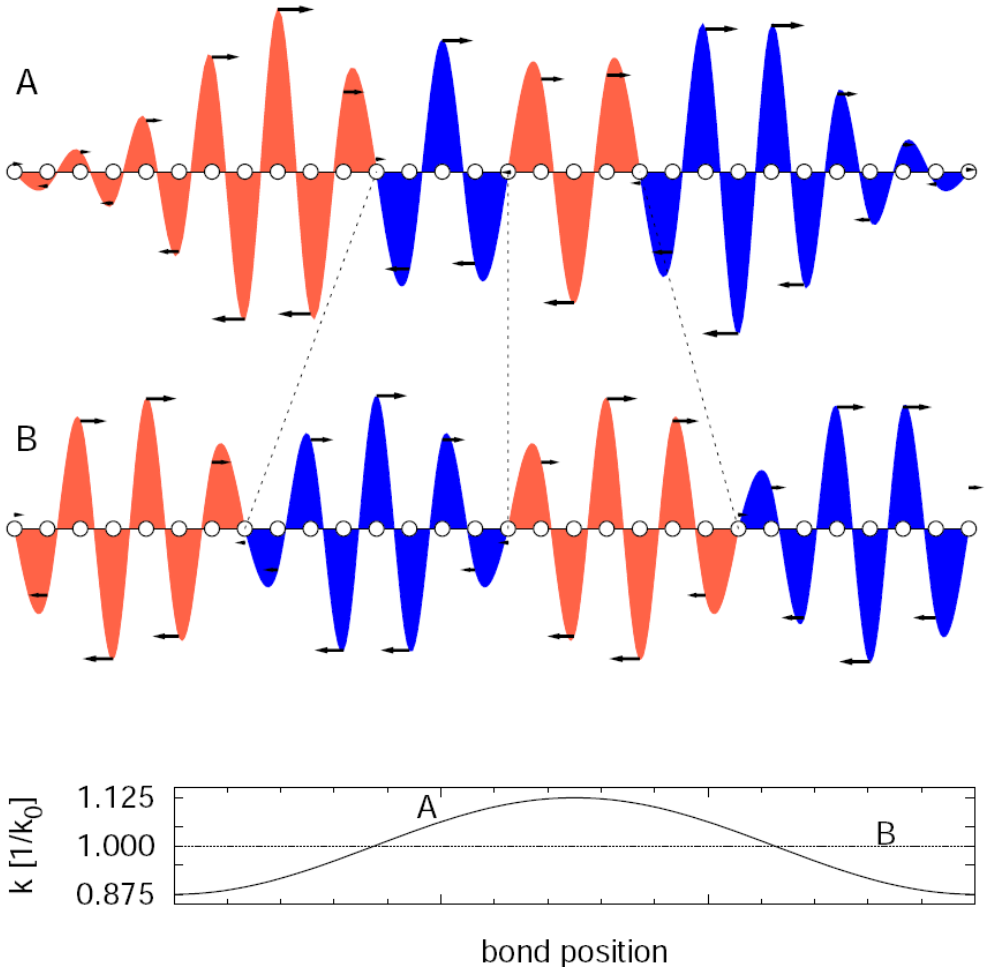

Figure 3.4: Change of the high-energy phonon mode for a periodic chain of atoms connected with simple springs. Figures show two different systems with either continuously changing (A) or uniform spring constant distribution (B). Variation of the spring constant along the chain is shown in lower figure. Arrows above and below the chain denotes the phonon eigenvectors and colors in curves different phases. Distance of the filled curve from the chain is comparable to the amplitude of the actual phonon eigenvectors and guiding lines are drawn to highlight the node migration.

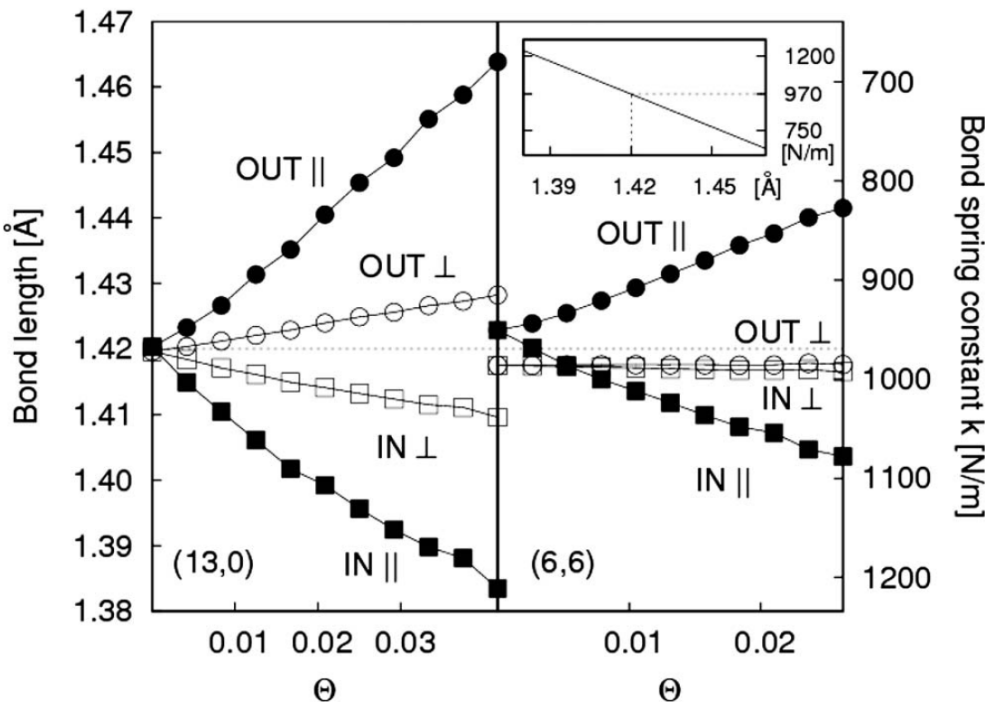

Figure 3.5: Variation of bond lengths for (13,0) (left) and (6,6) (right) tubes as a function of bending parameter $\Theta = D/2R$, where D is tube diameter and R radius of the curvature measured from the axis. Bonds are divided into mostly parallel (||) and mostly perpendicular ($\perp$) bonds with respect to tube axis (in and out refer to the sides of torus). Inset shows the effective nearest neighbor spring constant, calculated by scaling single graphene layer; the inset was used to map the bond length scale (left-hand axis) into spring constant scale (right-hand axis). Bonds parallel to tube direction will be changed continuously along the circumference of the tube from short in inner side to long in outer side of the bending. Taken from paper II.

varies continuously along the circumference. Symmetry breaking affects the nodal division of the phonon modes especially at high energies. Because of the collective nature, the low-energy modes hardly change at all. Change in high-energy modes can be visualized with a simple model of chain of atoms connected periodically with springs. Figure 3.4 shows the migration of the nodes between the systems with uniform and continuously changing distribution of spring constants. Vibrating sections closer to weak interactions get wider, while the nodes and antinodes with changing amplitudes migrate towards stronger interactions. In addition, vibrations vanish towards the weakest interactions, which makes the node area effectively bigger. The relative variation in the spring constant is fitted to the actual change in bonds of the bent nanotubes, modeling the effective interaction strength on different side of the bending. Actual interaction behavior for bonds in zigzag and armchair tubes is shown in figure 3.5.

Figure 3.6 visualizes changes in the high-energy modes of zigzag (13,0) and armchair (6,6) tubes due to bending. Bending parameter is defined as $\Theta = D/2R$, where D is tube diameter and R radius of the curvature measured from the axis. The same kind of changes are visible for the nanotube as for the simple chain described previously. Due to bending, the nodes get denser and vibrating sections narrower in either inner or outer part of the bending with changed amplitudes. Migrating nodes and antinodes induce polarizability change for some specific new modes that become Raman-active, at least in non-resonant picture, that was represented in section 2.6.1. One specialty is the splitting of the degenerate modes to be visible in different polarization pictures, which is caused by the differences in nodal structure due to bending. Being orthogonal to each other, one of the degenerate modes has nodes and the other antinodes at the inner and outer part of the bending. Lengths of different vibrational sections along the circumference is the same in the degenerate mode with nodes in inner and outer part of the bending, whereas the balance is disturbed in the other degenerate mode with antinodes in inner and outer part of the bending.

Figure 3.7 represents the high-energy non-resonant Raman spectra for three different kind of tubes, zigzag, armchair and chiral showing the contribution from the G-band modes. The changes in spectra show the newly appeared Raman-active modes as new spectral peaks and the behavior of the peaks is directly related to changes in modes. Roughly, the more the nodal division and antinodes resemble the originally Raman-active modes, the more intensive the new Raman-active modes become. Change in the mode energies depends on the side on which the vibrations concentrates as bending increases. If the atoms vibrate mostly on the inner part where bonds get shorter, the energy of the mode will increase. On the other hand, if the atoms vibrates mostly on the outer part, where bonds get longer, the energy of the mode will decrease.

Change in the mode energy is dependent on the tube chirality and the type of the mode. For example there is a linear increase of ~ 25 cm^{-1}/% for high-energy mode A_0^+

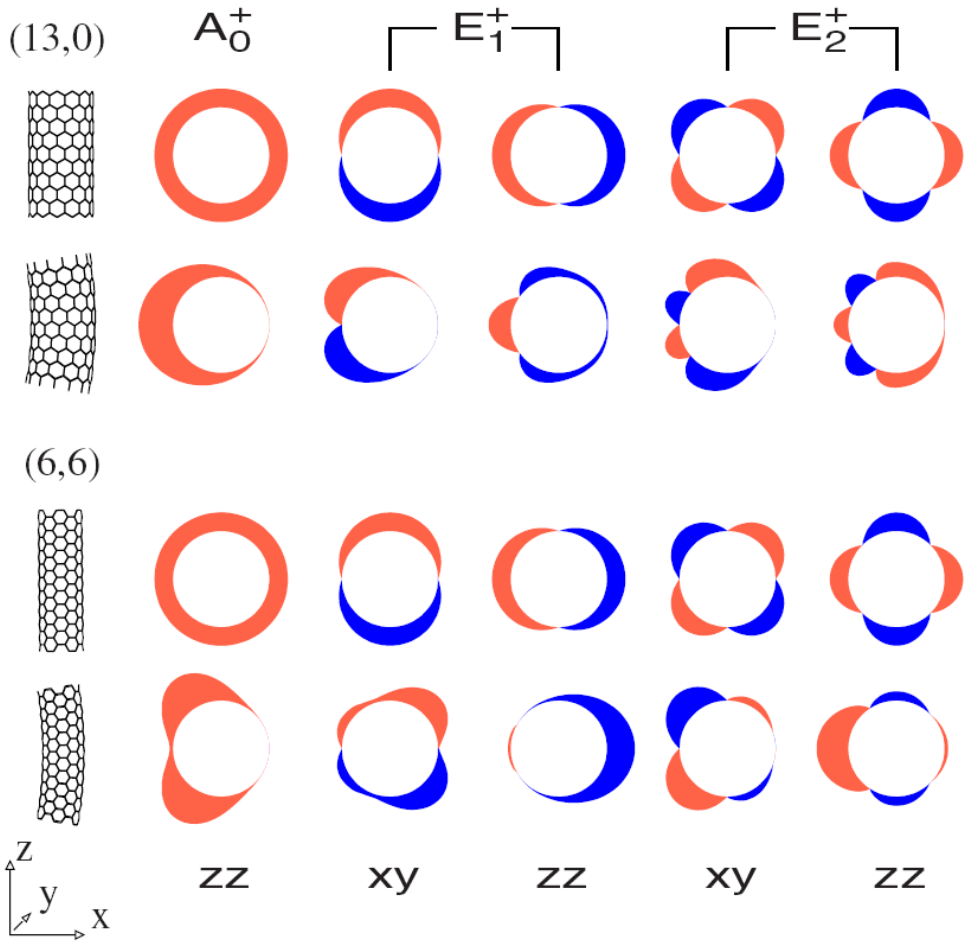

Figure 3.6: Qualitative view of the nodes and antinodes of selected vibration modes for (13,0) and (6,6) tubes. Thick blue line represents an antinode, red an antinode with opposite phase and vanishing line a node; the actual direction of the vibration amplitude is either circumferential or along tube axis. Modes are for straight or bent tubes as indicated on the left. The symbols below show the polarization pictures where the bent modes become most visible. Migration of the nodes and antinodes to both inner and outer part of the bending is observed. The degenerate individual modes from the same symmetry will be split under bending into different polarization spectra. Taken from paper II.

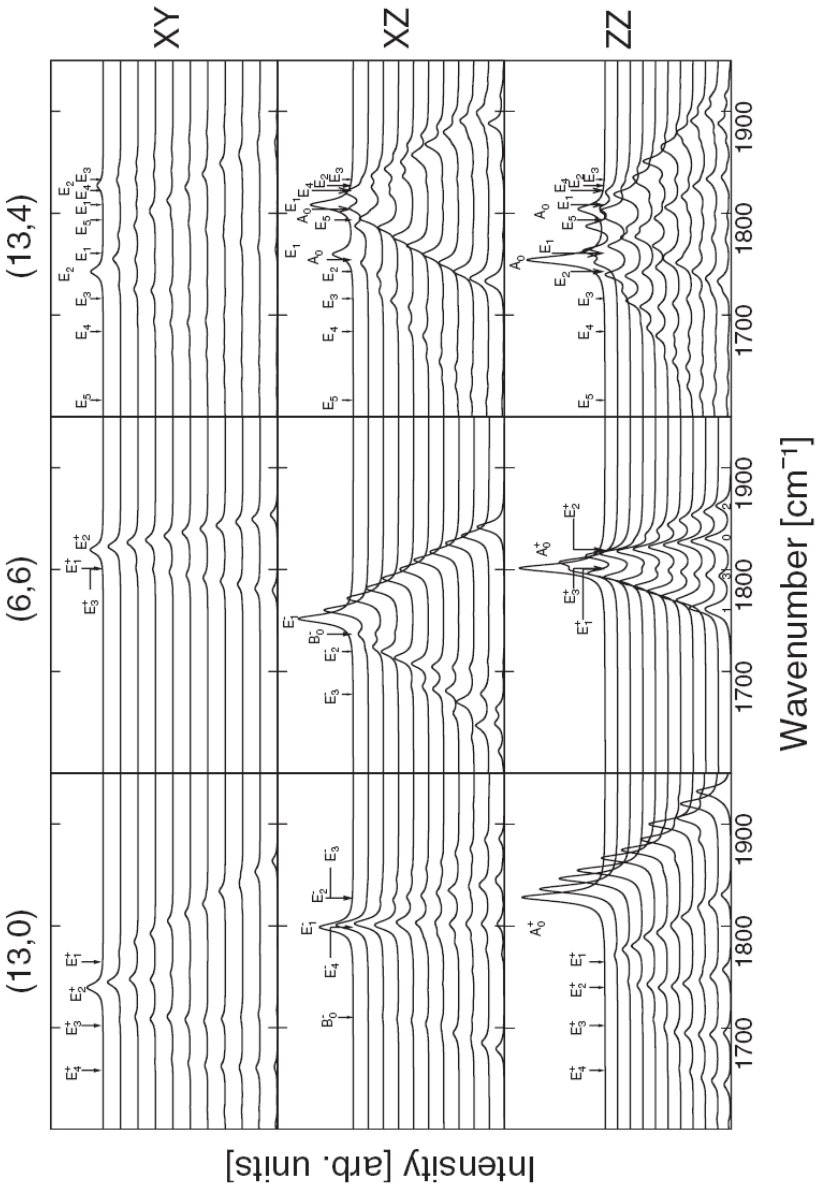

Figure 3.7: Raman spectra of bent (13,0): $\Theta = 0 - 4.2$ % ,(6,6): $\Theta = 0 - 2.6$ % and (13,4): $\Theta = 0 - 4.8$ % carbon nanotubes in different polarization picture of incident and scattered light (on right). As the bending increases there exist new peaks in spectra i.e. new Raman-active modes, for which probable and observed contributions from original straight tube modes are labeled. The behavior of the different modes is assigned into the zz-polarization spectra of (6,6) tube. Taken from paper II.

in zigzag tube (13,0), as for armchair tube (6,6) the change is much less ~ 10 cm^{-1}/%. The difference can be explained with a few insights: first, characteristics of the A_0^+ high-energy mode changes from longitudinal to circumferential between zigzag and armchair, and second, the chiralities of the tubes are different. The latter defines how the bonds are arranged along the tube direction, and further affects the average interaction strength seen by the phonon. All of the chiral tube modes are restricted mainly by these two conditions. Estimation of the mode behaviour accurately for arbitrary chirality and mode is impossible based on only three different tubes. The behaviour of the A_0^+ symmetric modes is the most predictable, and should fall in chiral tubes into the range defined by the zigzag and armchair tubes.

Raman measurements for individual straight tubes is used to determine the chirality of the tube, as was mentioned in the Introduction. Even though bending is not straightforward to apply, it could possibly offer an additional way to confirm the exact chirality out of those few possibilities, because of the chirality-dependent behavior of the high-energy modes under bending. Furthermore, there is no need to break the tube and go beyond the critical buckling limit. Because of the reversible control, the tubes can be used afterwards in applications. Even more useful are these observations for studying nanotube serpentines, that might be the way in the future to assemble nanotubes for new applications.

3.3 Self-passivating edge reconstructions of graphene

Zigzag and armchair have for long time been considered as the only two stable edges of graphene. Article III predicts that in addition to the conventional edges, there is a third energetically even more favorable edge. At the same time these results call for a one new emphasis on graphene research. Article IV compares the vibrational properties and Raman spectra of the new edge and of the zigzag and the armchair edges.

Figure 3.8 shows the reconstructions for graphene edge, optimized with DFT and GPAW (Section 2.1), which are investigated in article III. The most interesting reconstruction is the uppermost edge with alternating heptagons and pentagons. Edge energies are shown in figure 3.9, which reveals that the best edge energetically is the reconstructed zigzag edge. It is even slightly lower in energy than the armchair edge. Comparison of binding energy of the molecular hydrogen H_2 to adsorption energy of hydrogen atom on the edges shows that single hydrogen atom wants to remain attached into H_2 molecule rather than detach and adsorb on the reconstructed zigzag edge. This makes the heptagon-pentagon edge reconstruction self-passivating. If there is hydrogen adsorbed on the edge, zigzag and armchair are the lowest in energy. In other words, to observe the reconstruction experimentally, very strict vacuum condi-

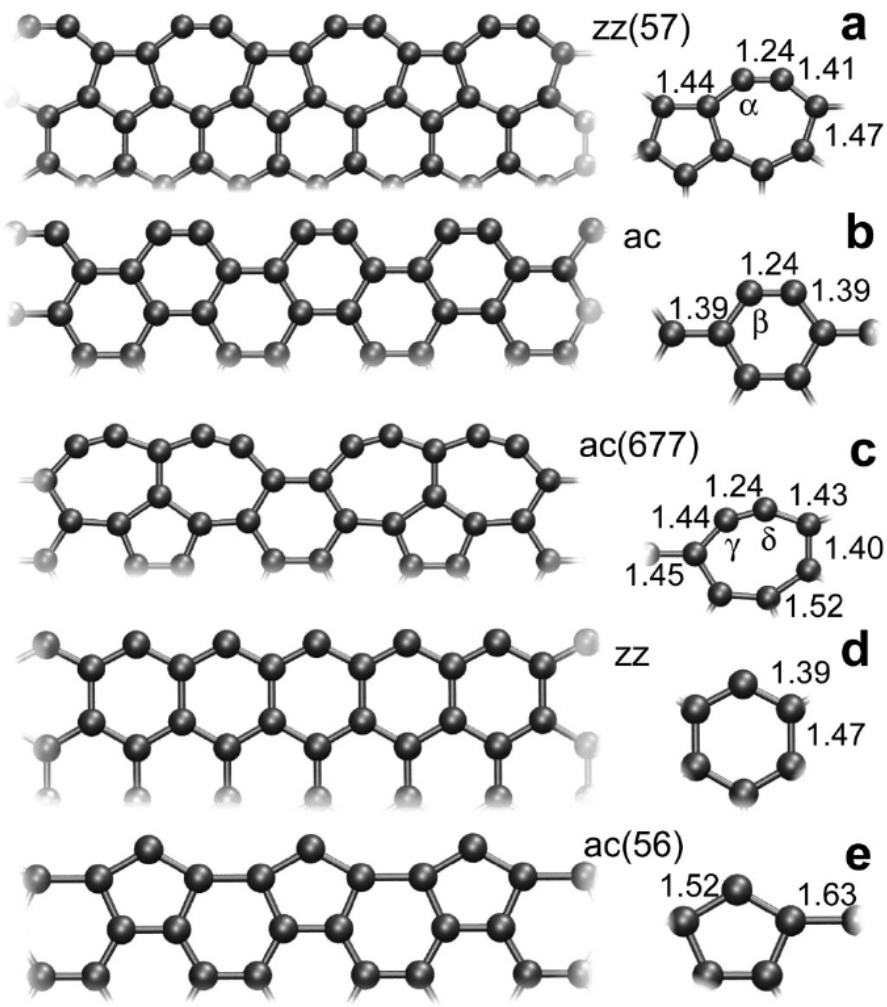

Figure 3.8: The geometries of graphene edges: (a) reconstructed zigzag [zz(57)] (later known also as reczag edge), (b) armchair (ac), (c) reconstructed armchair [ac(677)], (d) zigzag (zz), and (e) pentagonal armchair [ac(56)]. The numbers in parenthesis denote the number of vertices in edge polygons. Some bond lengths (in Å) and bond angles are shown on the right: The bond angles are $\alpha = 143°$, $\beta = 126°$, $\gamma = 148°$, and $\delta = 147°$. All geometries are strictly in-plane. Taken from paper III.

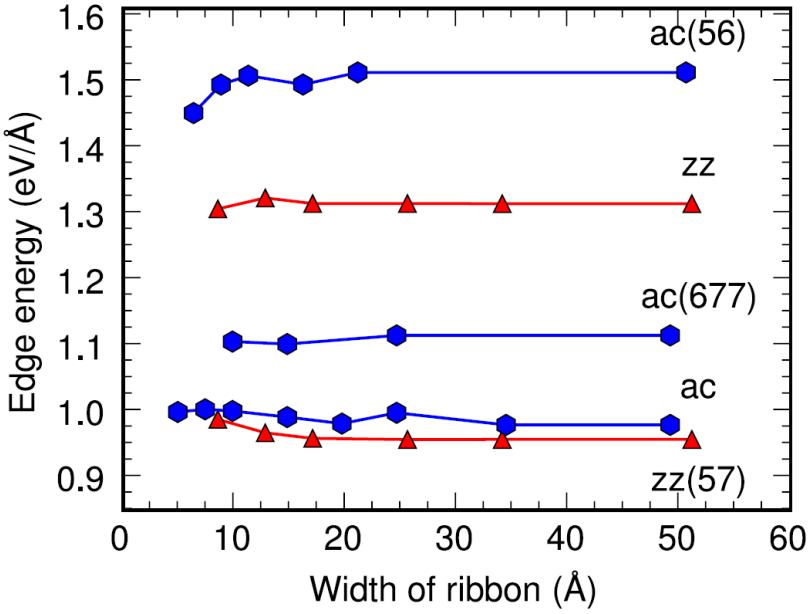

Figure 3.9: The edge energies of carbon nanoribbons. Energies are plotted as a function of the ribbon width for the edges in figure 3.8. The edge energy for zz(57) geometry drops more than 0.3 eV/Å compared to zz and has in general the lowest edge energy. Although calculation was not spin-polarized, the energy difference remains the approximately the same also with spin-polarization [101, 102]. This result infers that zigzag edge is metastable without hydrogen passivation. Taken from paper III.

tions are required.

Difference between zigzag and reconstructed zigzag edge can be seen in the electronic structure and STM image shown in figure 3.10. Reconstruction shifts the dangling bond bands away from the Fermi energy and triple-bonds — the signature of passivation — are seen in theoretical STM-image as isolated bright islands on the edge.

Figure 3.11 shows the non-resonant Raman spectra of graphene ribbons with zigzag, armchair and reconstructed zigzag edges calculated with DFTB, Section 2.2. The spectral details – allowing the identification of the reconstruction – are the edge-localized modes and the triple-bond vibrations. The stretching modes of the triple-bonds are well separable in energy to other modes, and exist only for reconstructed zigzag and armchair ribbons. Breathing and G-band modes do not change in shape or energy, because in them none of the atoms vibrate on the edge.

Reconstruction releases the tension caused by the dangling bonds on the zigzag edge,

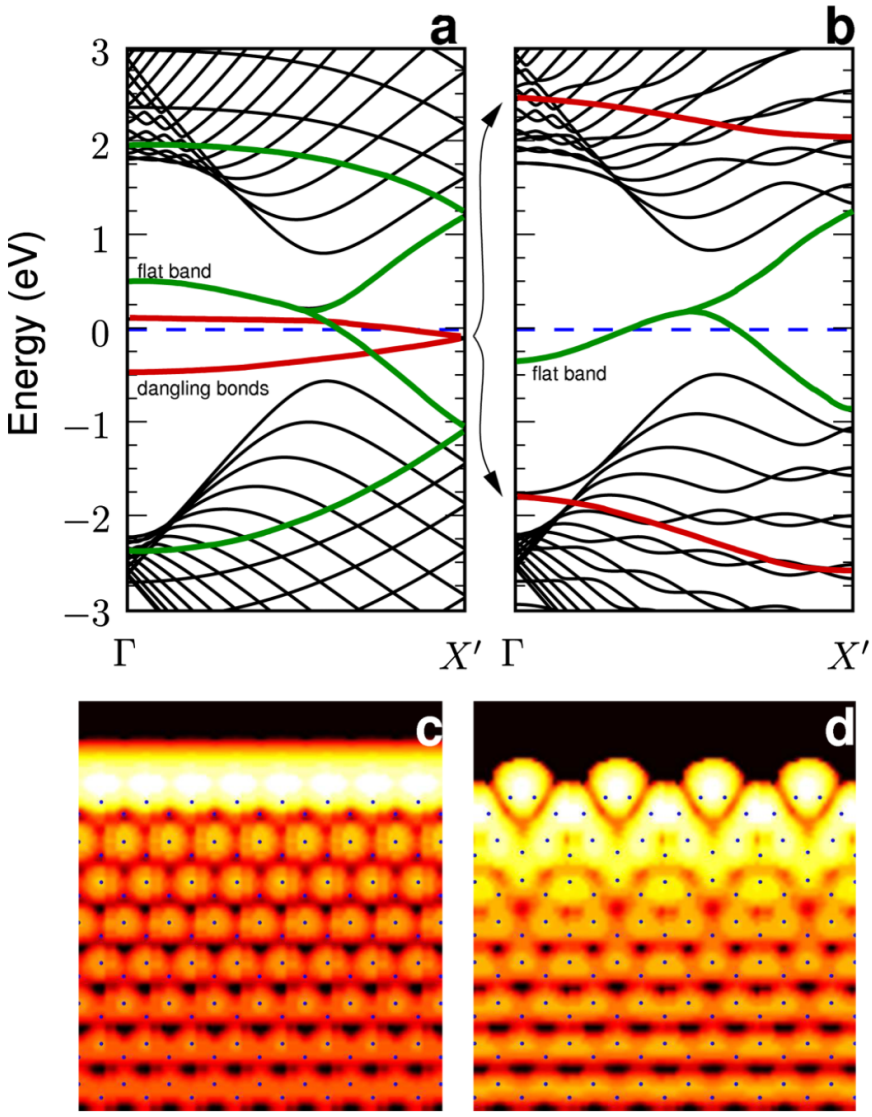

Figure 3.10: The electronic band structure of zigzag and zz(57) edges. (a) and (b) show the band structure for 34 Å wide zigzag and zz(57) nanoribbons, respectively. Dashed line is the Fermi level. The colored bands were identified directly by visual inspection of the wave functions. (c) and (d) show the height profiles of simulated scanning tunneling microscope images in the constant current mode of the respective edges (height variations > 2 Å), formed by integrating the electron density from occupied bands within 0.1 eV of the Fermi energy. The degeneracies at the gamma point are 2 and 4 for the dangling bonds and the flat band, respectively. The reason for non-flat flat-band of zigzag edge is in the spin-polarization that was not taken account. Reconstructed zigzag edge is not spin-polarized in general. After all the main differences in both electronic structure and in STM-image will remain the same. Signs about the passivation, due to the reconstruction, is realized in the shift of dangling bond bands and in the bright nearly isolated triple-bond islands. Taken from paper III.

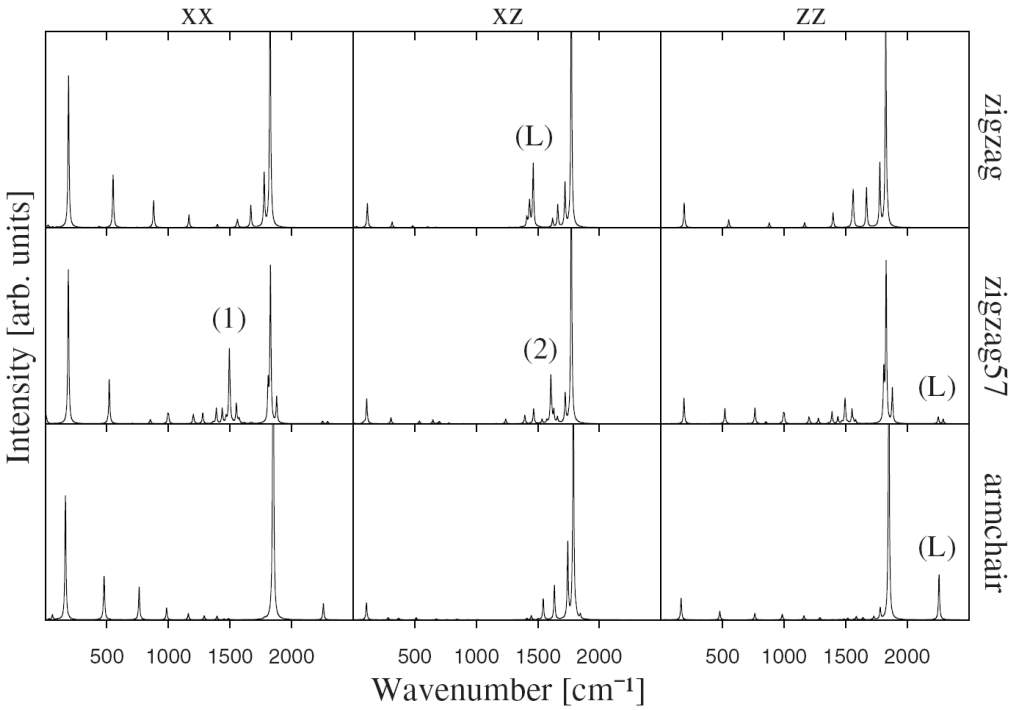

Figure 3.11: Raman spectra of zigzag, reconstructed zigzag, zz(57) (=zigzag57), and armchair graphene nanoribbons (different rows). Columns denote different incident and scattered light polarization spectra (uppermost symbols xx, xz and zz). Edge-localized modes are assigned with symbol (L). Symbols (1) and (2) are the spectral peaks different from zigzag and armchair ribbons. Raman spectra are drawn using Lorenz distribution with full width at half maximum of 5 cm^{-1}. Characteristics that could be used to identify the reconstructed zigzag edge are the edge-localized modes including triple-bond stretching on high energies. Taken from paper IV.

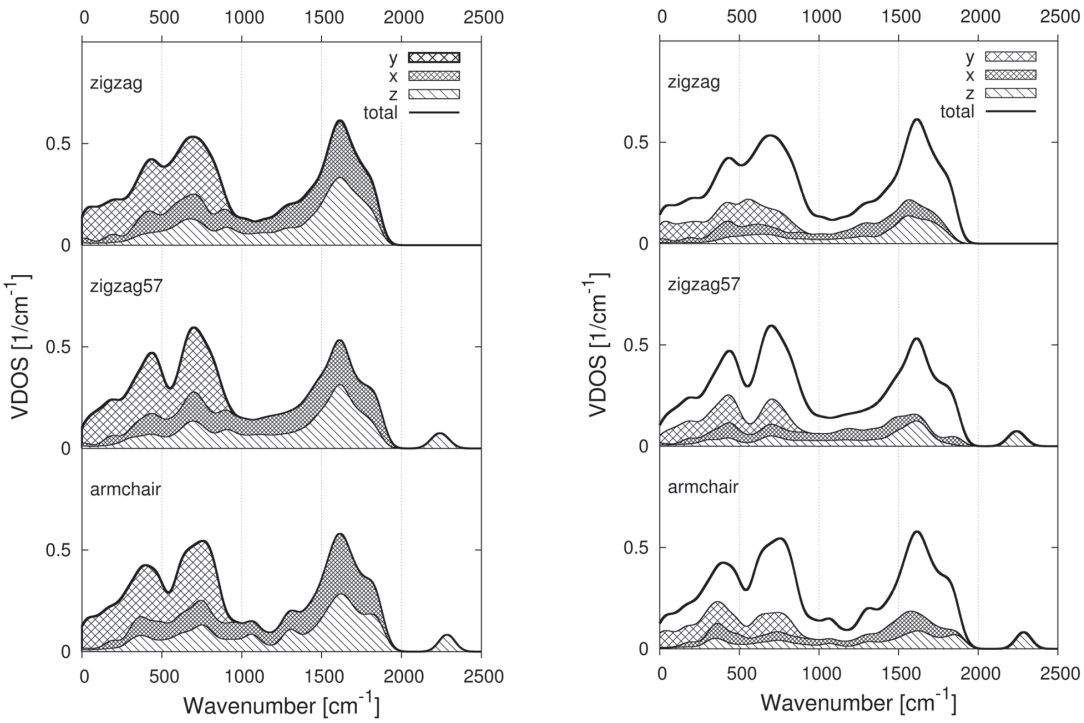

Figure 3.12: On the left the total and on the right the edge-weighted vibrational density of states of zigzag, reconstructed zigzag, zz(57) (=zigzag57), and armchair graphene nanoribbons. Contribution of different directions in vibrational states is shown in different patterned areas. Vibrational density of states is broadened with normal distribution with $\sigma = 45$ cm^{-1}, chosen to illuminate general changes in VDOS under reconstruction. VDOS of the reconstructed zigzag edge resembles the same width armchair, rather than zigzag edge VDOS. Meaning of the edge is dominant for the fine structure of the VDOS profile. Taken from paper IV.

but increases the rigidity of the reconstructed edge. Figure 3.12 shows the total and edge-weighted vibrational density of states (VDOS) separated into different directions. VDOS profiles were calculated with DFTB, Section 2.2. The ribbon with reconstructed zigzag edge resembles the same width armchair, rather than zigzag edge vibrational density of states. Characteristic triple-bonds can be seen in the high energies for both reconstructed zigzag and armchair ribbons, different from zigzag ribbon. In general the increase in the energies of the vibrational states located on the edge is visible in all directions, which confirms the increased rigidity of the reconstructed zigzag edge compared to the zigzag edge.

3.4 In-plane adsorption and diffusion of gold atoms in graphene

Y.Gan et.al. reported in 2008 in-plane diffusion of metal atoms in axial direction of multiwall carbon nanotubes, in-plane of graphene and along graphene edge [70]. The observed diffusion of Au and Pt using transmission electron microscope, discussed in the Introduction, were unexpectedly similar in all of the systems, with activation energies of about 2.5 eV. Article V reports theoretical results for in-plane adsorption of gold atoms in different vacancies of graphene and estimates diffusion barriers and possible mechanisms. Based on theoretical results and information given in the experiment, our interpretation about the diffusion is that it is rather radiation-enhanced than thermally activated.

Figure 3.13 shows the formation energies for vacancies and Au-vacancy complexes separately calculated with DFT, Section 2.1. The difference of these two energies gives the adsorption energy for gold atoms into the given vacancy. The lowest formation energy for Au-vacancy complex gives the optimal in-plane site for the gold atom, which is the double vacancy. In other words, if the gold atom is assumed to be in-plane position, it prefers the double vacancy; and without any additional disturbances the gold atom will eventually remain in the double vacancy after getting there. The adsorption energies range from 3 to 6 eV for most of the vacancies, which gives reason to assume strong binding. Binding of the gold atom to neighboring carbon atoms is not supported in a triangular four-atom vacancy, from which the gold atom is easy to displace.

Analysis of projected density of states, described in Section 2.3, and wavefunctions for the gold atom and neighboring carbon atoms in double vacancy confirms strong chemical binding. Figure 3.14 shows that both in-plane and out-of-plane orbitals bind together in several ways. It is especially the binding of out-of-plane orbitals together that restrict the gold atom to be in-plane position.

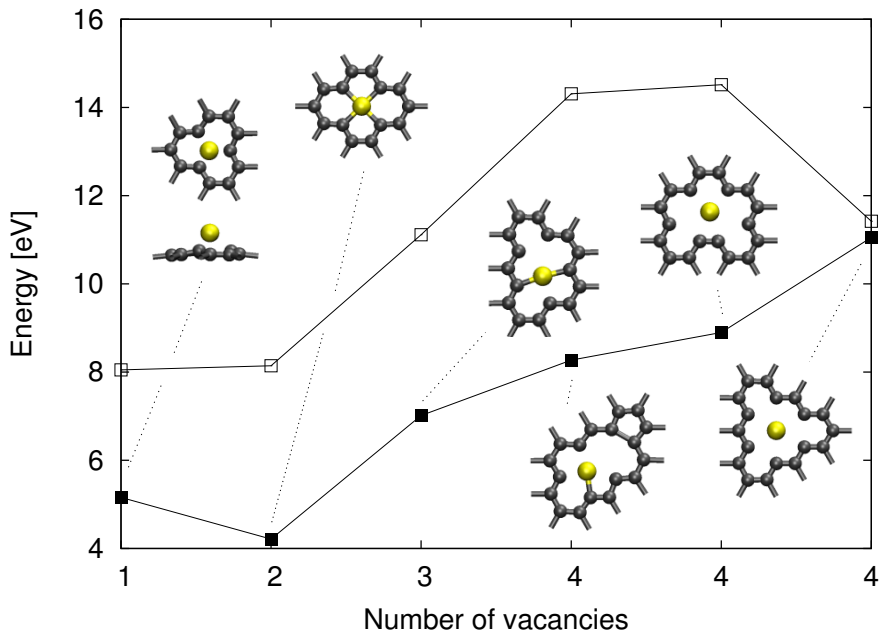

Figure 3.13: Energies for carbon vacancies in graphene (empty squares), and formation energies for Au in graphene vacancies (filled squares; optimized local geometries shown in insets). The difference between the two curves is the Au adsorption energy. Apart from the Au in single vacancy, all structures are planar. The lowest formation energy for Au-vacancy complex reveals the double vacancy to be the optimal in-plane site for the Au atom. Taken from paper V.

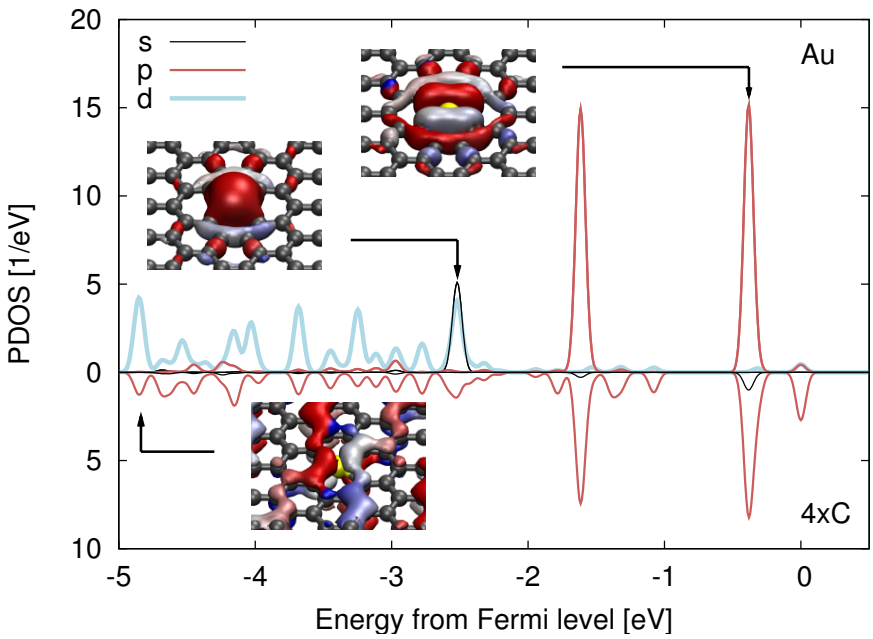

Figure 3.14: Density of states for $s-$, $p-$ and $d-$orbitals of Au (above abscissa) and the four neighboring C atoms (below abscissa). Insets show the wave functions, color standing for the phase, for selected $s-$, $p-$ and $d-$dominated contributions for Au. Charging of Au according to Bader analysis is $+0.5e$. Orbitals bind together in various ways referring to strong bonding of Au atom in double vacancy. Especially binding of out-of-plane orbitals restrict the out-of-plane motion of the gold atom from above and below the graphene layer. Taken from paper V.

If the in-plane diffusion is completely thermal, the optimal vacancy site must be involved. Figure 3.15 shows the examples of the diffusion paths and energy barriers for the gold atom in the double vacancy, which were calculated with DFT and NEB, Sections 2.1 and 2.7. The lowest energy barriers are large ($\geq$ 4 eV) compared to the experimental activation energies ($\approx$ 2.5 eV). Furthermore, the optimized diffusion paths with the lowest barriers do not support in-plane diffusion, because either the gold or the carbon atom has to be taken considerably out of the plane. The closest in-plane is the path III in figure 3.15, which has already a 7 eV energy barrier.

Diffusion barriers for the gold atom in the double vacancy complex do not match with thermal activation. Lower in-plane diffusion barriers are possible, but only for bigger vacancy sites. Figure 3.16 shows one example of diffusion path for triple vacancy with even lower than 2 eV energy barrier. Diffusion in bigger than double vacancies would be justified due to TEM-imaging that constantly creates at least single vacancies into the system and excites the motion of carbon atoms. Single-atom vacancies and interstitial atoms diffuse rapidly [32, 103, 104] and can instantly merge and anneal existing vacancies.

In addition to big vacancies, the diffusion barrier for the gold atom in the single vacancy can be much lower compared to the double vacancy [105]. Diffusion of the Au in the single vacancy happens out-of-plane and does not in this respect coincide with the experimental observations. As figure 3.13 showed, formation energies of the Au-vacancy complexes do not support the existence of single vacancies either; at least, the existence of double vacancies can not be overruled. Out-of-plane positions were not seen for any structure in experiment or in our MD-simulations. Inside the multiwalled carbon nanotubes the out-of-plane motion is in general unlikely. If the in-plane diffusion is possible in multiwalled carbon nanotubes, there should exist similar mechanism also in graphene, which requires a consistent interpretation. After all, the mass difference of gold and carbon atoms and the binding properties are against thermally activated out-of-plane motion.

Reanalyzing the TEM-effect, diffusion and displacing rates coincide with each other, which gives the most prominent explanation for the experiment to be radiation-enhanced diffusion. This interpretation would explain the similarities between the diffusion of different metals in different dimensions and in systems, because under radiation the metal-carbon interface does not play such a crucial role. In the radiation-enhanced interpretation, temperature creates the background conditions and the TEM-beam makes the diffusion of gold atom possible by opening a diffusion route in one way or another. Figure 3.17 shows one possibility for radiation-enhanced diffusion process including a loop of merging of the vacancies, diffusion, and annealing. In radiation-enhanced interpretation the barrier for the direct diffusion of double vacancy is also lower, because the motion of carbon atoms around the gold atom is excited.

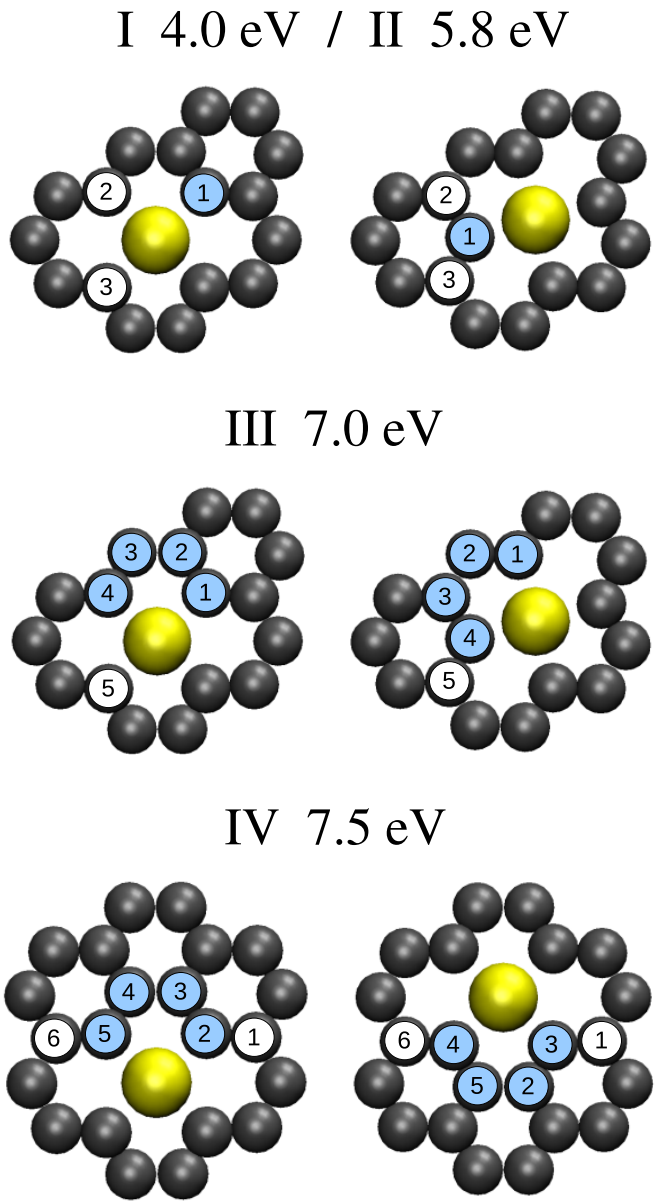

Figure 3.15: Diffusion mechanism paths and their transition state energies for Au in double vacancy. Numbers help to visualize C atom identification during Au jump; blue for C atoms that change positions. Paths were optimized using nudged elastic band method with almost linearly interpolated initial guess. Path I contains out-of-plane motion of Au, whereas path II contains out-of-plane motion of C(1). The lowest energy barrier, given by path I, is much larger than the experimental observation. Taken from paper V.

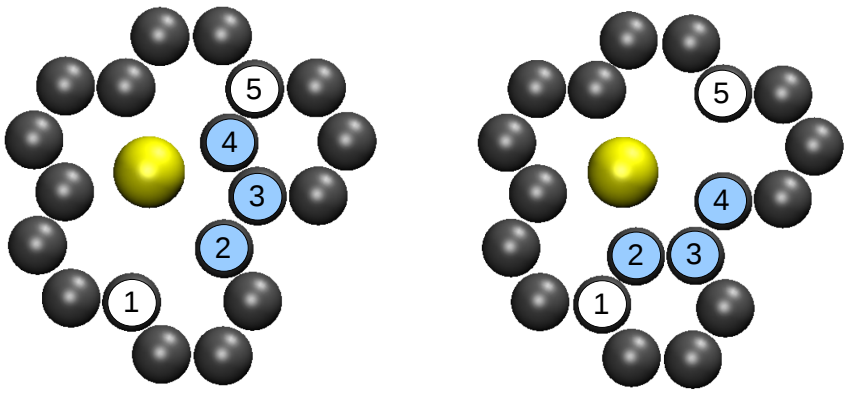

Figure 3.16: An example of the diffusion path for Au in triple vacancy having even lower than 2 eV energy barrier. The diffusion path consists of three moving blue carbon atoms C(2)-C(4) (blue) changing their initial positions shown on the left into final positions shown on the right, and filling the empty side of the triple vacancy.

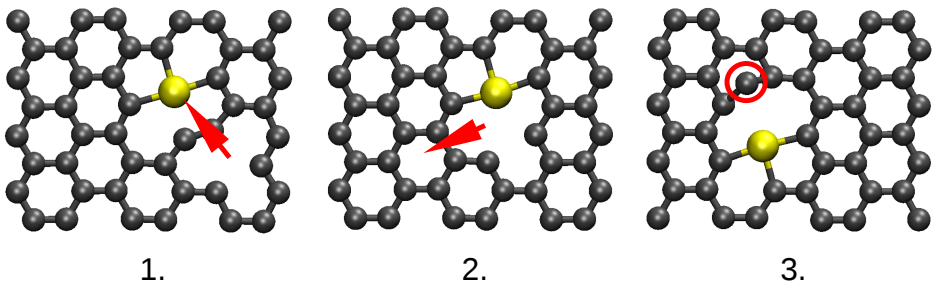

Figure 3.17: One possible sketch for the radiation-enhanced diffusion mechanism. In part 1., the single vacancy merges with the Au in double vacancy. In part 2., Au is in triple vacancy after merging and can diffuse easily. In final part 3., after the diffusion of Au in triple vacancy, the interstitial carbon atom anneals the empty side. Because of the constant TEM-imaging, the loop can start again from the beginning.

4 Summary & Outlook

In science the interface of experiments and theory is a two-way road, where predictions and confirmations shake hands. If a prediction is acknowledged, it usually happens after the confirmation. Although it sounds selfish, the scientific goal of the researcher is to be correct with his/her claims, and because of that, already believing to be correct is thrilling. There is a narrow gap from a selfish to a healthy view on science, from which the latter is purely guided by the joy from solving problems and understanding the physics behind them.

We have contributed theoretical research in close relation to experiments from both sides; predicting but also explaining experiments. Related to the papers of this thesis, the most important prediction in my opinion was the metastability of the zigzag edge. Reconstructed zigzag — now termed the reczag edge — was found to have even lower edge-energy than armchair. The experimental proof was found very soon, within a year from our prediction. Aberration-corrected TEM-images published in Science [71] with outstanding resolution reported behavior of the hole in a single layer of the graphene. Existence of the reczag edge is clear in those experimental images, as shown in figure 4.1, but it was unfortunately overlooked in the original Science paper. There are several frames in the supporting material video, that show rather long segments of reczag edges, that sometimes last several seconds. Because of the TEM-conditions, the lower edge energy cannot be confirmed experimentally and specially not all of the zigzag edges were reconstructed during the experiment.

Something can be still interpreted due to the experiment. When the carbon atoms are displaced away from the edge, the underlying hexagonal lattice reveals only either zigzag or armchair edges. In addition, the reczag edge as well as armchair edge need two carbon atoms to repair themselves. It is also good to note, that compared to the other local reconstructions and defects seen during the experiment, the reczag edges are over all in majority. Things that could possibly affect the appearance differences between zigzag and reczag edges during the measurement are charging of the edge by TEM-beam and corners of the hole in the graphene layer. Corners in the hole can release the tension present on zigzag edge making the it more stable. The size of the vacancy affects the length of the edges, which at the same time decreases the possibilities to reconstruct the edge.

Effects of bending on Raman-active modes of carbon nanotubes have also received interest among experimentalists. Carbon nanotubes can be assembled as serpentines

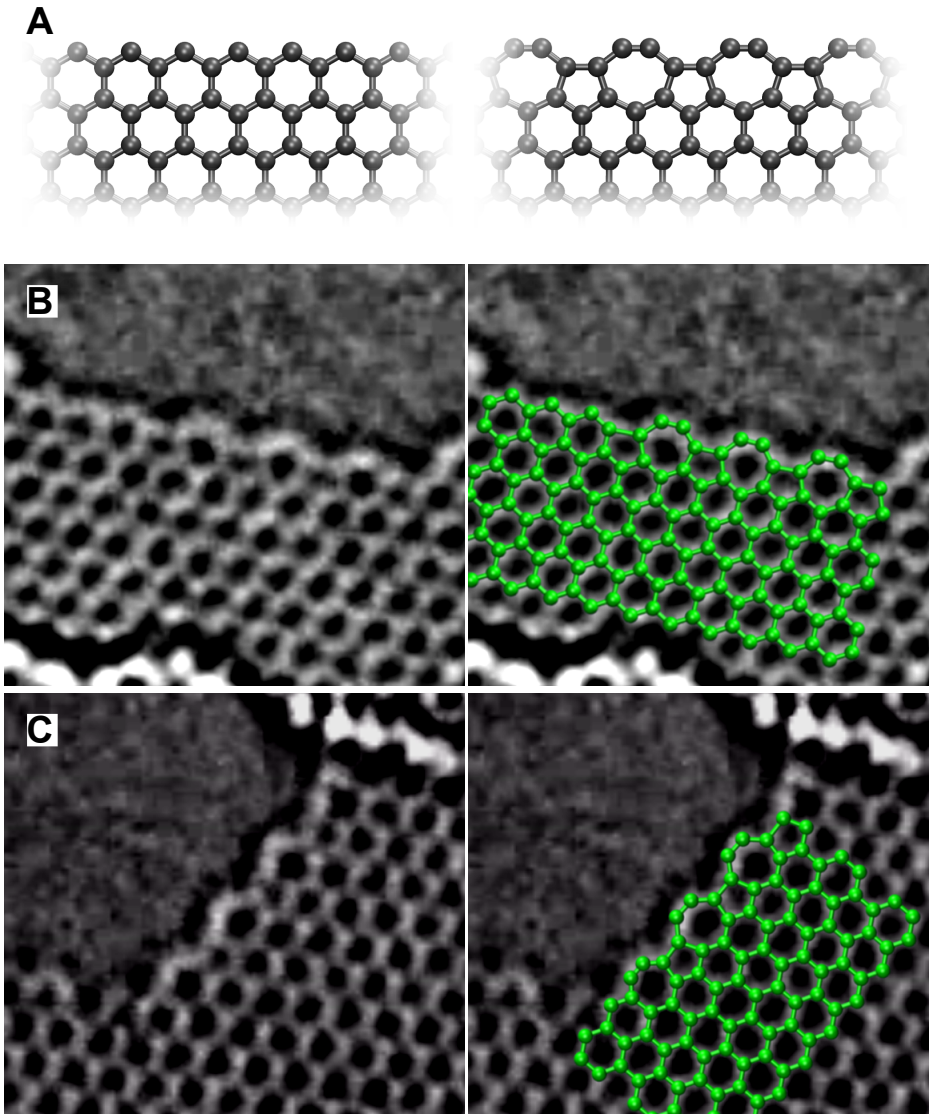

Figure 4.1: Theoretically calculated structures of reconstructed zigzag (right) edge side by side with zigzag edge (left) in (A). (B) and (C) show the experimental proof for existence of the reconstructed zigzag edge. Bright areas at the edge can be identified to triple bonds characteristic for both reconstructed zigzag and armchair. The difference in edge profiles of reconstructed zigzag and pure zigzag is obvious. Taken from Ref. [71].

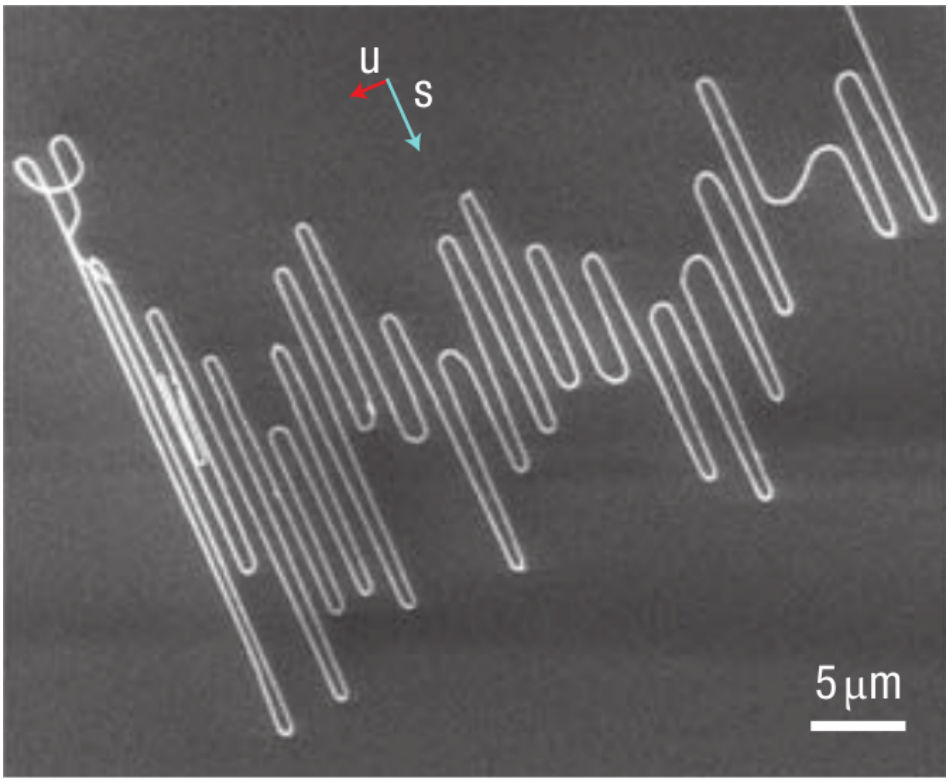

Figure 4.2: Scanning electron microscope (SEM)-image of nanotube serpentine on miscut quartz substrate. Parallel straight sections coincide with the step edges of the substrate (s-vector). Vector u denotes the direction of the gas flow, which guides the landing of the growing nanotube on the substrate. Taken from Ref. [38].

on specific miscut substrates like quartz (vicinal α-SiO_2) shown in figure 4.2, and can have strong local curvatures [38]. Measuring the Raman spectra along the nanotube from the different sections of serpentines, changes due to increase in bending can be obtained. Raman measurements for this kind of systems have been already done and reports are on the way. The results confirm our predictions for different G-band mode behavior under bending [106].

On the other hand, explaining already existing experiment [70] was the main ambition of the article V reporting gold atom adsorption and diffusion in the graphene plane. After the experiment in Ref. [71], which reported the dynamics of the hole in graphene under TEM-conditions, we could put also our alternative interpretation about radiation-enhanced diffusion better into a perspective. Growth of the big vacancy and excitation of the motion of carbon atoms are inevitable under TEM-imaging. The experiment about the hole dynamics in Ref. [71] was for single layer

graphene, while the experiment about metal atom diffusion in-plane of graphene in Ref. [70] has two to three graphene layers. Although the lattice structure beyond the edge seems to be quite stable in the experiment of Ref. [71], in multi-layer carbon structures the generation of small vacancies with TEM is more probable than in single layer structures. After all the acceleration voltage was much higher, around 300 kV in the diffusion study in Ref. [70] compared to hole dynamics study in the Ref. [71] with acceleration voltage around 80 kV. Both of these facts gives good reason to assume excited motion of carbon atoms and existence of single and double of vacancies due to TEM-beam during the metal atom diffusion study in Ref. [70].

There are always ways to do things better. Considering this thesis, resonant Raman calculations would have improved the reliability and extension of the results e.g. giving directly comparable intensities to experiments and information about the D-band. To explain changes in the modes themselves, the same investigations should have still been performed as in papers I, II and IV.

Can there be something more general to be understood based on the results? Or could the observations be used to improve old or to invent something completely new? Those are the questions, that should be asked after every research project. Strong binding reflects usually better conduction properties, if there is conduction at all. One relevant problem related to strong binding of metal atoms in-plane of graphene would be to investigate conduction and mechanical properties of a direct contact of metal electrode and graphene through vacancies. These contacts could be furthermore compared to contacts done by for example oxygen plasma treatment. If the direct contact improves considerably conduction properties compared to the non-covalent graphene-metal contacts or contacts through anchor molecules between them, their properties and use in real applications should be investigated. At the same time understanding how to control metal atoms in-plane of graphene would become crucial. Experimentally this may not be too difficult, because selective irradiation to form vacancies can be already done and adsorption of metal atoms to these preconditioned vacancies is already observed. Similarly it is true that metal atoms can clusterize around plasma treated or pure vacancies in carbon nanostructures. This kind of study would in my opinion give great insight for understanding metal-carbon nanostructure contacts in general. Attachment of electrodes to any point of the layer through vacancies rather than only to the edges would have plenty of advantages. In addition to contacts, systems with different concentration of metal atoms in graphene could have also other interesting properties.

The generalized boundary conditions of different symmetries can be useful for further research, not only for Raman study of carbon nanotubes. Wedge boundary conditions allow investigation of all kind of properties with respect to bending based on quantum mechanical description. To give some examples, diffusion of vacancies or ad-atoms in graphene with respect to bending can be studied in detail, small portion of multi-

walled carbon nanotubes with several layers can be constructed with small number of atoms, and properties of wiggly nanotube structures like serpentines can be calculated as well; all without any additional constraints, only applying specific boundary conditions. One can consider for example boron-nitride tubes and try to find out the reasons behind the current increase under bending and separate them from effects caused by contacts to electrodes. In this problem the first obvious observable to look would be the electron density of states, that is directly given in DFTB.

Appendix A: From many-electron problem to Kohn-Sham equations

The following description about DFT is gathered from several different references, that will be cited separately. The similar kind of overviews can be found from many reviews about DFT, including Refs. [60, 107] that are used here. Before going to actual basic principles of the density functional theory, let us formulate general many-electron problem. The Hamiltonian consists of kinetic $\hat{T}$ and potential part $\hat{V}$, latter including Coulomb interaction between electrons, and interaction of electrons to nuclei and external fields [60]

$$\begin{aligned}\hat{H} =& \hat{T} + \hat{V}_{ee} + \hat{V}_{ext} \\ =& \sum_{i=1}^{N} \frac{1}{2}\nabla_i^2 + \sum_{i\neq j} \frac{1}{|\mathbf{r}_i - \mathbf{r}_j|} - \sum_{i=1}^{N}\sum_{m=1}^{M} \frac{Z_m}{|\mathbf{r}_i - \mathbf{R}_m|} + V_{\text{field}} \ ,\end{aligned} \tag{A.1}$$

where nucleus m has charge Z_m in position $\mathbf{R}_m$ and electrons are located in $\mathbf{r}_i$. All the equations in this chapter are written in atomic units.

Due to Born-Oppenheimer (BO) approximation electron and nuclear parts of wavefunction and Hamiltonian can be separated $\Psi_{tot} = \Psi_{el}\Psi_{nuc}$. In other words, because of the big mass difference, nuclei affect on electrons effectively through their fixed positions. Under BO-approximation the time-independent Schrödinger equation for electrons is

$$\hat{H}\Psi_j = \varepsilon_j \Psi_j \ , \tag{A.2}$$

where Ψ_j are the many-electron eigenfunctions and ε_j eigenenergy of the system. Eigenenergies of the many-electron problem have the lowest limit, the ground state energy $\varepsilon_0 \leq \varepsilon_j = \langle \Psi_j | H | \Psi_j \rangle$; $\forall\ j \neq 0$, which is known as Rayleigh Ritz principle [108].

Because electrons are fermions the wavefunction must obey Pauli principle and be antisymmetric with respect to electron exchange $\mathbf{r}_n\sigma_n \rightarrow \mathbf{r}_m\sigma_m$ [107]. $|\Psi(\mathbf{r}_1\sigma_1, ..., \mathbf{r}_N\sigma_N)|^2$ describes the probability to find the electrons in their positions $\mathbf{r}_i$ with spin σ_i and integration of the square of the wavefunction over the all space must give one. Electron density can be constructed using the probability interpretation from the electron

wavefunction

$$n(\mathbf{r}_i) = N \int \int ... \int |\Psi(\mathbf{r}_1\sigma_1, ..., \mathbf{r}_N\sigma_N)|^2 d^3r_1...d^3r_{i-1}d^3r_{i+1}d^3r_N \ . \tag{A.3}$$

At this point we enter the density functional theory, whose soul is the Hohenberg-Kohn theorem: The ground state wavefunction of the system can be uniquely determined by the ground state electron density [61]. Further, also the ground state potential is uniquely determined by the ground state electron density. In other words, there is a unique mapping between ground state electron density, wavefunction, and potential. Every ground state observable inherits the same unique connection to electron density through the ground state wavefunction.

Minimizing energy due to variational principle with respect to electron density gives the ground state electron density n_0 and ground state energy $E[n_0]$ [107]

$$\frac{\delta E[n]}{\delta n(r)} = 0 \Rightarrow n_0, E[n_0] \ , \tag{A.4}$$

where energies obey $E[n_0] \leq E[n]$; $n \neq n_0$. Using electron density in equation (A.3) the total energy of the system can be written as a sum of the universal functional $F[n] = T[n] + V_{ee}[n]$, same for all many-electron systems, and functional due to external potential $V_{ext}[n]$

$$E[n] = F[n] + V_{ext}[n] = T[n] + V_{ee}[n] + \int n(r) \left(-\sum_m \frac{Z_m}{|\mathbf{r}_i - \mathbf{R}_m|} + V_{\text{field}} \right) dr \ . \tag{A.5}$$

The Kohn-Sham method [62] takes the kinetic and potential energies of a model non-interacting system and shifts the missing information about the true interactions into an extra term called exchange-correlation energy E_{xc}. The model system of non-interacting electrons gives the same ground state density as the true interacting system, which follows from the Hellman-Feynman theorem [107]

$$\frac{dE_\lambda}{d\lambda} = \langle \Psi_\lambda | \frac{\partial H_\lambda}{\partial \lambda} | \Psi_\lambda \rangle \ , \tag{A.6}$$

where Hamiltonian H_λ depends on scaling parameter λ of Coulomb interactions between electrons. Integration of the equation (A.6) from non-interacting $\lambda = 0$ to interacting $\lambda = 1$ gives the equality between the electron densities of the model and the true systems. Hellman-Feynman theorem indicates that the total energy of interacting many-electron system can be always found doing just one-electron theory.

Due to the non-interacting approach in Kohn-Sham method, the ground state wavefunction $\Psi(\mathbf{r}_1\sigma_1, ..., \mathbf{r}_N\sigma_N)$ can be written as a simple Slater determinant

$$\Psi[n](\mathbf{r}_1\sigma_1, ..., \mathbf{r}_N\sigma_N) = \frac{1}{\sqrt{N!}} \begin{vmatrix} \phi_1(\mathbf{r}_1\sigma_1) & . & . & . & \phi_1(\mathbf{r}_N\sigma_N) \\ . & & & & . \\ . & & & & . \\ . & & & & . \\ \phi_N(\mathbf{r}_1\sigma_1) & . & . & . & \phi_N(\mathbf{r}_N\sigma_N) \end{vmatrix} , \tag{A.7}$$

where $\phi(\mathbf{r}_i\sigma_i)$ are so-called Kohn-Sham orbitals. The total energy of Kohn-Sham system is a sum of non-interacting kinetic and potential energy parts and exchange-correlation term

$$E[n] = T_S[n] + V_{ee}[n] + V_{ext}[n] + E_{xc}[n] , \tag{A.8}$$

where the external potential is represented in equation (A.5) and $T_S[n]$ is the kinetic energy part of the non-interacting electrons

$$\begin{aligned} T_S[n] &= -\frac{1}{2}\sum_{i=1}^{N}\int d^3r\phi_i^*(\mathbf{r}\sigma)\nabla_i^2\phi_i(\mathbf{r}\sigma) \\ V_{ee}[n] &= \frac{1}{2}\int\int d^3r d^3r' \frac{n(\mathbf{r})n(\mathbf{r}')}{|\mathbf{r}-\mathbf{r}'|} \\ V_{ext}[n] &= \int d^3r v_{ext}(\mathbf{r})n(\mathbf{r}) . \end{aligned} \tag{A.9}$$

The exchange-correlation energy functional is the difference between the exact energies of the real interacting system and the energies of the non-interacting model system

$$E_{xc}[n] = F_{HK}[n] - T_s[n] - V_{ee}[n] - V_{ext}[n] , \tag{A.10}$$

where $F_{HK}[n]$ is the exact energy from the Hohenberg-Kohn theorem only. The functional derivative of the exchange-correlation energy with respect to electron density determines the exchange-correlation potential. Because there is not exact exchange-correlation functional, it must be approximated. This is the subject of Appendix B.

The Kohn-Sham Hamiltonian is exact if the exchange-correlation functional is exact. The total Hamiltonian of the Kohn-Sham system can be written in terms of single particle Hamiltonians h_s

$$\hat{H} = \sum_{i}^{N} h_s(\mathbf{r}_i) = \sum_{i=1}^{N}\left(-\frac{1}{2}\nabla_i^2 + v_s(\mathbf{r}_i)\right) , \tag{A.11}$$

where v_s includes the potential components of equation (A.1), but now in addition also the exchange-correlation potential $v_s(\mathbf{r}) = v_{ee}+v_{ext}+v_{xc}$. After these assumptions

the problem diminishes to a set of single-particle Schrödinger equations, that can be solved separately

$$\left(-\frac{1}{2}\nabla^2 + v_s\right)\phi_i(\mathbf{r}\sigma) = \varepsilon_i\phi_i(\mathbf{r}\sigma) \ . \tag{A.12}$$

Electron density of equation (A.3) can be written in the Kohn-Sham approach

$$n(\mathbf{r}) = \sum_{\sigma}\sum_{i=1}^{N}|\phi_i(\mathbf{r}\sigma)|^2 \tag{A.13}$$

and the Kohn-Sham potential

$$v_s(\mathbf{r}) = v_{ee} + v_{ext} + v_{xc} \ , \tag{A.14}$$

which finalizes the Kohn-Sham equations (A.12)-(A.14), that must be solved self-consistently. Numerically, the procedure starts with an initial guess for electron density n, which determines the Kohn-Sham potential v_s, and further gives a new electron density. The loop $n \rightarrow v_s \rightarrow n \rightarrow \ldots$ goes on up to self-consistency in electron density and potential.

Forces for atoms can be solved from the total energy of the system, based on Hellman-Feynman theorem in (A.6), by differentiating the Hamiltonian with respect to nuclei positions. Forces are needed in the optimization of the ground state structure and atomic motion in DFT-based molecular dynamics simulations. For the local energy minimum structure all of the forces approach zero.

Appendix B: From local density to generalized gradient approximation

The next description is mainly based on the original paper of PBE, GGA-functional, that can be found from Ref. [74]. The exchange-correlation energy is one of the critical parts in the density functional theory to have right physics, although its contribution to total energy is comparably small. Exchange-correlation potential can be solved exactly only for the homogeneous electron gas; the local density approximation (LDA) is the first step in approximations [60]. It approximates the electron density to be constant around each position and defines the exchange-correlation functional using an analytic solution for homogeneous electron gas

$$E_{xc}^{LDA}[n] = \int d^3 r n(\mathbf{r}) \varepsilon_{xc}(n) \ , \tag{B.1}$$

where the exchange-correlation energy density $\varepsilon_{xc}(n) = \varepsilon_x(n) + \varepsilon_c(n)$ can be determined from the homogeneous electron gas exchange-correlation potential through relation[108]

$$v_{xc}^{LDA}[n(\mathbf{r})] = \left.\frac{d\varepsilon_{xc}}{dn}\right|_{n=n(\mathbf{r})} = -\left(\frac{3}{\pi} n(\mathbf{r})\right)^{1/3} \ . \tag{B.2}$$

LDA works well only for systems with slowly varying density profiles and, naturally, the more the system reminds the homogeneous electron gas, the better is LDA approximation. The local spin density approximation LSD [107, 109] is a version of LDA where the spin is taken account.

For systems with stronger density variations corrections are needed. The next extension is to take into account gradient corrections to the density. Gradient corrections can be derived formally by taking expansion on the density and its gradients. With first order corrections gradient expansion approximation (GEA) functional is established; more extended generalized gradient approximation (GGA) functionals includes also higher order terms[60]. Compared to the LDA functional in equation (B.1) GGA functional depends also on density gradient ∇n [74]

$$E_{xc}^{GGA}[n] = \int d^3 r n(r) \varepsilon_{xc}(n, \nabla n) \ . \tag{B.3}$$

The critical point is to determine a suitable form for $\varepsilon_{xc}(n, \nabla n)$. One way is to write it in terms of an enhancement factor F_{xc} and the homogeneous electron gas exchange-correlation energy ε_x^{unif}

$$E_{xc}^{GGA}[n] = \int d^3r n(\mathbf{r}) \varepsilon_{xc}^{unif}(n) F_{xc}(r_s, \zeta, s) \ , \tag{B.4}$$

where F_{xc} depends on the Wigner-Seitz radius r_s giving information about the electron density, spin-polarization ζ, and dimensionless, renormalized density gradient s. This interpretation is used in the PBE-formulation [74], that is presented next.

Fitting the exchange-correlation functional to produce exact experimental results is one option, but has often limited physical grounds out of their fitting ranges. Perdew, Burke and Ernzerhof reported in 1996 PBE version of GGA exchange-correlation functional [74], which uses fitting parameters based on fundamental facts rather than on empirical parameters.

Exchange and correlation parts in the exchange-correlation functional can be separated $E_{xc} = E_x + E_c$. The correlation functional in GGA has the form

$$E_C^{GGA}[n_\uparrow, n_\downarrow] = \int d^3r n[\varepsilon_C^{unif}(r_s, \zeta) + H(r_s, \zeta, t)] \ , \tag{B.5}$$

where r_s is the local Seitz radius ($n = 3/4\pi r_s^3 = k_F^3/3\pi^2$), $\zeta = (n_\uparrow - n_\downarrow)/n$ is the relative spin polarization, and $t = |\nabla n/2\phi k_s n|$ is dimensionless density gradient. $\phi(\zeta) = [(1+\zeta)^{2/3} + (1-\zeta)^{2/3}]/2$ is a spin-scaling factor, and $k_s = \sqrt{4k_F/\pi a_0}$ is the Thomas-Fermi screening wavenumber ($a_0 = \hbar^2/me^2$).

In the PBE functional the gradient contribution of H can be fitted to a couple of physical restrictions. In the slowly varying density limit ($t \to 0$) H is given by second order gradient expansion, which satisfies the GGA expansion in general. Respectively, in the rapidly varying density limit ($t \to \infty$) correlation should vanish and H should then approach the uniform electron gas correlation $-\varepsilon_C^{unif}$. Under uniform scaling $n(r) \to \lambda^3 n(\lambda r)$ at the high-density limit $\lambda \to \infty$ (yielding $r_s \propto \lambda^{-1} \to 0$ and $t \propto \lambda^{1/2} \to \infty$), the correlation energy must be constant. In addition, the logarithmic singularity existing at the high-density limit of ε_C^{unif} should be neglected in H, that must therefore also be proportional to logarithmic function. As a result of these requirements

$$H = \left(\frac{e^2}{a_0}\right) \gamma \phi^3 \ln\left[1 + \frac{\beta}{\gamma} t^2 \left(\frac{1 + At^2}{1 + At^2 + A^2 t^4}\right)\right] \ , \tag{B.6}$$

where

$$A = \frac{\beta}{\gamma}\left[\exp\left\{\frac{-\varepsilon_C^{unif}}{(\gamma\phi^3 e^2/a_0)}\right\} - 1\right]^{-1} \ . \tag{B.7}$$

Parameters γ and β are adjusted based on the slowly and rapidly varying limit, and high-density scaling limit.

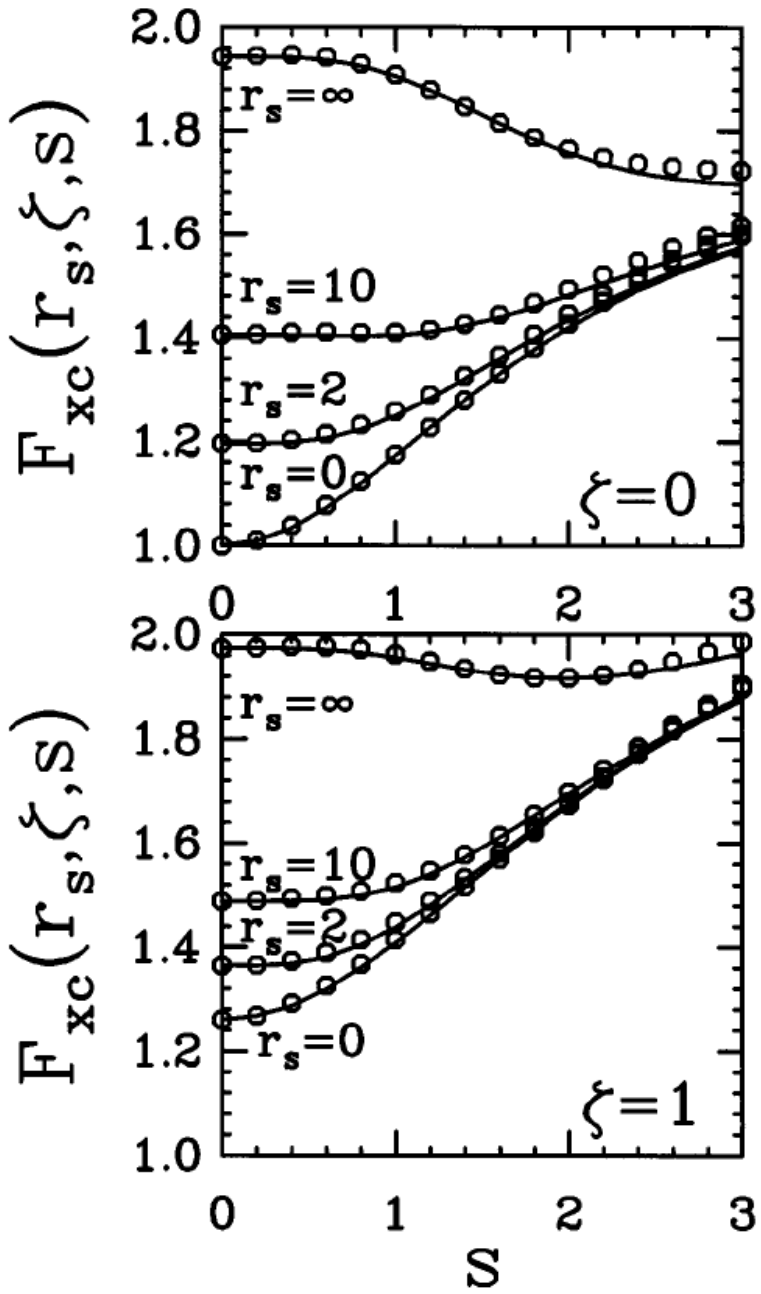

Figure B.1: Electron density gradient s dependence of the enhancement factor F_{xc} representing the non-locality effects of the electron density within GGA PBE-functional in solid lines and compared to another GGA functional PW91 with circles. $\zeta = 0$ is for spin unpolarized and $\zeta = 1$ for spin polarized system. Increase in r_s means increasing electron density and increase in s increase in electron density gradient. Taken from Ref. [74].

To complete the full exchange-correlation energy, the exchange part is also needed. The GGA exchange energy is in general

$$E_X^{GGA} = \int d^3r n \varepsilon_X^{unif}(n) F_X(s) \ , \tag{B.8}$$

where $\varepsilon_X^{unif} = -3e^2 k_F/4\pi$ is the exchange energy of the uniform electron gas, and $s = |\nabla n|/2k_F n = (r_s/a_0)^{1/2}\phi t/c$ is, in addition to t, another dimensionless density gradient with $c = (3\pi^2/16)^{1/3}$.

The gradient correction function $F_X(s)$ for the exchange part can be formed also based on some physical requirements. E_X must scale like λ under uniform density scaling described for the correlation part before equation (B.6). At the limit of a vanishing density gradient, E_X must give the uniform electron gas exchange energy insisting $F_X(0) = 1$. The correct spin-scaling of the exact exchange energy, $E_x[n_\uparrow, n_\downarrow] = (E_x[2n_\uparrow] + E_x[2n_\downarrow])/2$ is desired. The excellent approximation of LSD for linear response of spin-unpolarized uniform electron gas with small density variations $s \to 0$ is satisfied with $F_X(s) = 1 + \mu s^2$. The universal lower bound for exchange-correlation energy i.e. Lieb-Oxford bound $E_X[n_\uparrow, n_\downarrow] \geq E_{XC}[n_\uparrow, n_\downarrow] \geq -1.679e^2 \int d^3r n^{4/3}$ will be satisfied if the spin polarized ($\zeta = 1$) enhancement factor F_x grows gradually due to density gradient s. This gives the condition $F_X \leq 1.804$. Final form of the gradient correction function in exchange part of PBE-functional can be written

$$F_X(s) = 1 + \kappa - \kappa/(1 + \mu s^2/\kappa) \ , \tag{B.9}$$

where κ is a tunable parameter. The total PBE exchange-correlation energy is a sum of the correlation part defined with equations (B.5), (B.6) and (B.7) and the exchange part defined with equations (B.8) and (B.9).

Figure B.1 shows the dependence of the enhancement factor F_{xc} on to gradient s. The limits and requirements made earlier become clear. With increasing gradients and in high electron-densities the exchange term dominates, while the correlation turns off. The exchange non-locality will be realized for valence electron densities, for which PBE acts more physically than LSD. In contradiction, at low-densities non-locality of the correlation term becomes dominating. As a remark, the non-locality will be approximately cancelled at the low-densities $r_s \to 0$ in fully spin-polarized system to maintain the correct features of LSD.

Appendix C: Projector augmented wave method

The details that are represented next will follow strictly the original paper of the PAW implementation into real-space grids and can be found in Ref. [110]. One essential part of the density-functional theory section is to choose suitable basis set for the system. The full set of electron states is not usually efficient to solve the problem, although the Kohn-Sham approach has itself already diminished the many-body problem into a set of single-electron problems.

The projector augmented wave method (PAW) [73, 110] is an all-electron method, which uses linear transformation to get all-electron Kohn-Sham wavefunctions from more practical pseudo-wavefunctions. The concept of pseudo-wavefunctions in general is to simplify the inert core states with pseudopotentials, that define the Hamiltonian for valence electrons. Instead of real wavefunctions, the valence electrons will be described with pseudo-wavefunctions. Within pseudopotentials the core states have to be solved only once, which makes the calculation faster. Some of the basic principles of pseudopotentials are build into the following PAW description, but the wavefunctions do not have to be normalized as in pure norm-conserving pseudopotential methods [111]. The PAW-method has been constructed also for plane waves, but that must not be mixed with the pseudo-wavefunction approach represented here.

In the PAW method, core-electron states are taken to be frozen. The rest of the wavefunctions is expanded into partial-waves inside the suitably chosen augmentation regions centered around each atom. An example of the core and valence state selection for platinum atom is shown in figure C.1. The expansion into valence pseudo-wavefunctions must be chosen to match the true all-electron wavefunction outside of the augmentation regions wavefunction. This is one of the basic requirements familiar from pure pseudo-potential methods also. Linear transformation between pseudo-wavefunction and all-electron wavefunction acts only inside the augmentation region and gives identity operator outside. Because of the projection to the all-electron wavefunctions, the PAW method gives true all-electron wavefunctions and densities. This is another main difference from the pure pseudopotential methods, in which the electron densities are constructed directly from the pseudo-wavefunctions. Figure C.2 shows the relation of pseudo-wavefunctions to all-electron wavefunctions in PAW-method with the CO-molecule example.

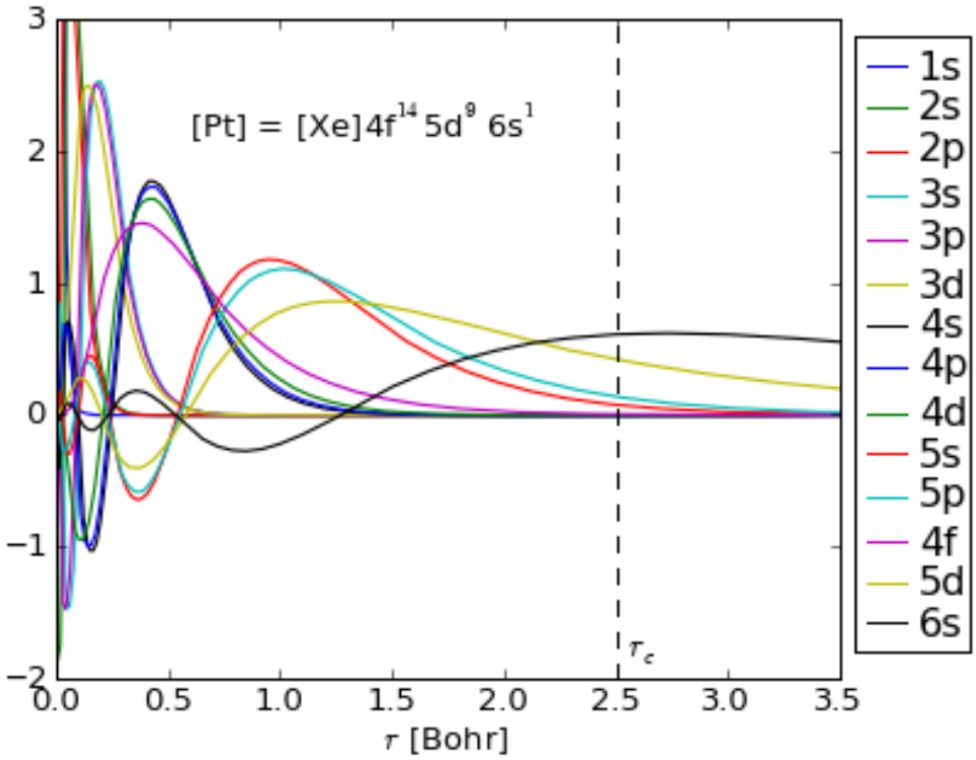

Figure C.1: Separation of wavefunctions of Platinum atom into core states $[Xe]$ and valence states $4f^{14}$, $5d^9$ and $6s^1$ with cutoff radius $r_c = 2.5$ Bohr. Taken from Ref. [72].

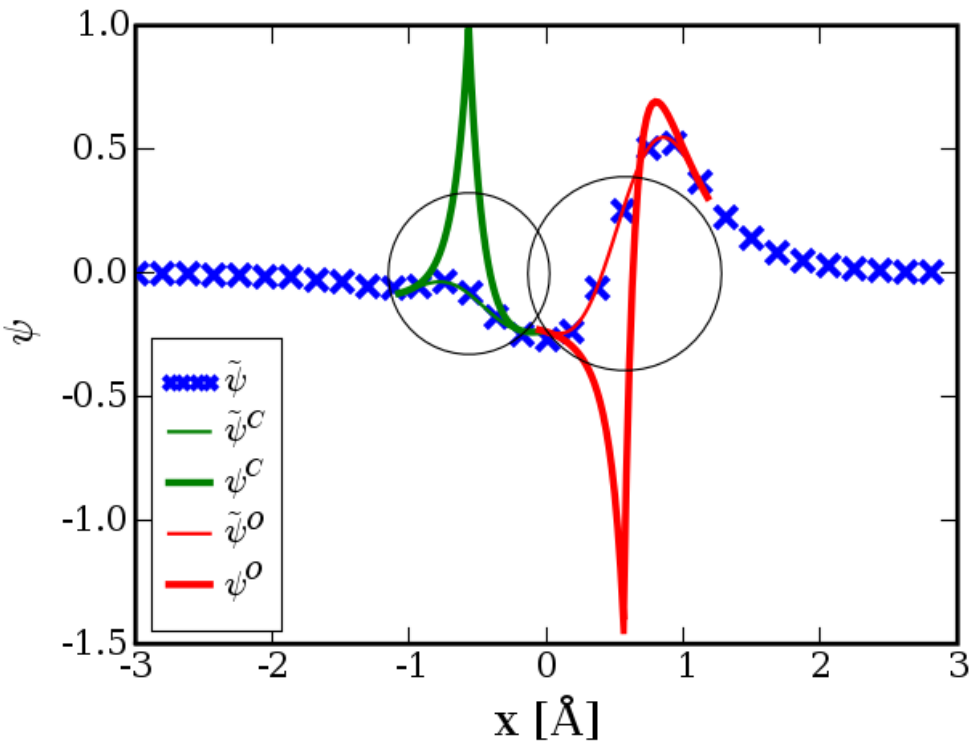

Figure C.2: Visualization of different wavefunctions in PAW-method for CO molecule, $\Psi^{C/O}$ stands for all-electron wavefunction (thick lines) and $\tilde{\Psi}^{C/O}$ for pseudo-wavefunctions (thin lines) of individual atoms C/O, and $\tilde{\Psi}$ for the total pseudo-wavefunction (blue crosses) of the CO molecule. Taken from Ref. [72].

The PAW-problem reduces to find out expression for the linear transformation defining the projection inside the augmentations regions. Linear transformation between a given smooth pseudo-wavefunction $\tilde{\Psi}_n$ and true all-electron Kohn-Sham wavefunctions Ψ_n is

$$\Psi_n(\mathbf{r}) = \hat{\tau}\tilde{\Psi}_n(\mathbf{r}) \ , \tag{C.1}$$

where n denotes the band index, and smoothness indicates, that there are no nodes in valence pseudo-wavefunctions. The transformation operator is determined in terms of atom-centered all-electron wavefunctions $\phi_i^a(\mathbf{r})$, the corresponding smooth partial pseudo-waves $\tilde{\phi}_i^a(\mathbf{r})$, and projector functions $\tilde{p}_i^a(\mathbf{r})$

$$\hat{\tau} = 1 + \sum_a \sum_i \left(|\phi_i^a(\mathbf{r})\rangle - |\tilde{\phi}_i^a(\mathbf{r})\rangle \right) \langle \tilde{p}_i^a(\mathbf{r})| \ . \tag{C.2}$$

Atom index is a whereas principal, angular, and magnetic quantum numbers (n, l, m) are combined into index i. Atom centered all-electron states ϕ_i^a, smooth partial valence states $\tilde{\phi}_i^a$, and projector functions due to partial states $\tilde{p}_i^a$ are left to be determined. For all of the three components the spherical symmetry around atoms is required

$$\begin{aligned} \phi_i^a(\mathbf{r}) =& \phi_{nl}^a(r) Y_L(\hat{\mathbf{r}}) \\ \tilde{\phi}_i^a(\mathbf{r}) =& \tilde{\phi}_{nl}^a(r) Y_L(\hat{\mathbf{r}}) \\ \tilde{p}_i^a(\mathbf{r}) =& \tilde{p}_{nl}^a(r) Y_L(\hat{\mathbf{r}}) \ , \end{aligned} \tag{C.3}$$

where Y_L is a real-valued spherical harmonics with index L including quantum numbers l and m. At this point a suitable cut off radius r_c^a is chosen for each augmentation region, which is of the same order as the cut-off radius for pseudopotential. By increasing the cutoff radius, smoother pseudo-wavefunctions can be found, but different augmentation regions must remain separable. Figure C.3 shows the schematic conditions for the augmentation regions.

To have a reasonable description for total all-electron wavefunction smooth partial waves of valence states must match the corresponding all-electron waves for $r > r_c^a$. Projector functions must be localized inside the augmentation spheres and be orthogonal with all-electron valence states: $\langle \tilde{p}_{i_1}^a | \tilde{\phi}_{i_2}^a \rangle = \delta_{i_1 i_2}$ and $\int_0^{r_c^a} r^2 \tilde{p}_{nl}^a \tilde{\phi}_{n'l}^a(r) = \delta_{nn'}$. With this construction also valence all-electron states transform linearly $\phi_i^a(\mathbf{r}) = \hat{\tau}\tilde{\phi}_i^a(\mathbf{r})$.

The electron density will have a rather simple form, which includes pseudo electron density and a correction term. First, from the atomic frozen-core electron density n_c^a can be constructed the smooth core-electron density $\tilde{n}_c^a$, that, like for wavefunctions, must be equal to the frozen core-electron density outside the augmentation sphere. Pseudo electron density has a contribution from the pseudo-wavefunctions $\tilde{\Psi}_n(\mathbf{r})$ and from the atom-centered smooth core-electron densities $\tilde{n}_c^a$

$$\tilde{n}(\mathbf{r}) = \sum_n f_n |\tilde{\Psi}_n(\mathbf{r})|^2 + \sum_a \tilde{n}_c^a(|\mathbf{r} - \mathbf{R}^a|) \ , \tag{C.4}$$

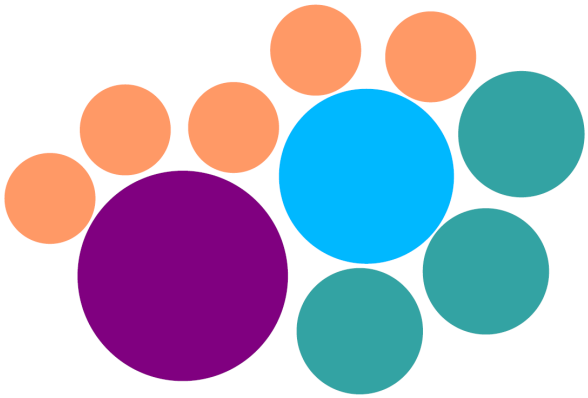

Figure C.3: Conditions for spherical augmentation regions within PAW, different colors denoting different atoms. For each kind of atom the cut-off radius is the same. Taken from Ref. [72].

where f_n are the occupation numbers and $\mathbf{R}^a$ is the position of atom a. Atom-centered all-electron and pseudo electron densities can be written

$$\begin{aligned} n^a(\mathbf{r}) &= \sum_{i_1 i_2} D^a_{i_1 i_2} \phi^a_{i_1} \phi^a_{i_2} + n^a_c(r) \\ \tilde{n}^a(\mathbf{r}) &= \sum_{i_1 i_2} D^a_{i_1 i_2} \tilde{\phi}^a_{i_1} \tilde{\phi}^a_{i_2} + \tilde{n}^a_c(r) \ , \end{aligned} \tag{C.5}$$

where $D^a_{i_1 i_2} = \sum_n \langle \tilde{p}^a_{i_1} | \tilde{\Psi}_n \rangle f_n \langle \tilde{\Psi}_n | \tilde{p}^a_{i_2} \rangle$ is the atomic density matrix. Finally the electron density in PAW formalism is

$$n(\mathbf{r}) = \tilde{n}(\mathbf{r}) + \sum_a \left[n^a(\mathbf{r} - \mathbf{R}^a) - \tilde{n}^a(\mathbf{r} - \mathbf{R}^a) \right] \ . \tag{C.6}$$

Total energy gets the same kind of form

$$E = \tilde{E} + \sum_a (E^a - \tilde{E}^a) \ , \tag{C.7}$$

where $\tilde{E}$ is the soft energy contribution and $E^a - \tilde{E}^a$ describes the correction needed for each atom a similarly as for electron densities in equation (C.6). The soft energy is

$$\begin{aligned} \tilde{E} = &\sum_n f_n \int d^3 r \tilde{\Psi}^*_n(\mathbf{r}) \left(-\frac{1}{2} \nabla^2 \right) \tilde{\Psi}_n(\mathbf{r}) + \frac{1}{2} \int d^3 r \tilde{v}_H \tilde{\rho}(\mathbf{r}) + E_{xc}[\tilde{n}(\mathbf{r})] \\ &+ \int d^3 r \tilde{n}(\mathbf{r}) \sum_a \overline{v}(|\mathbf{r} - \mathbf{R}^a|) \ , \end{aligned} \tag{C.8}$$

where E_{xc} is the exchange-correlation energy, $\tilde{v}_H$ is the pseudo-Hartree potential satisfying Poisson equation $\nabla^2\tilde{v}_H = -4\pi\tilde{\rho}$. $\overline{v}$ is an arbitrary localized potential vanishing outside the atomic augmentation region. Energies in correction term are given by

$$E^a = \sum_i^{core} \int d^3r \phi_i^{a,core}(\mathbf{r}) \left(-\frac{1}{2}\nabla^2\right) \phi_i^{a,core}(\mathbf{r}) + \sum_{i_1 i_2} D^a_{i_1 i_2} \int d^3r \phi_i^a(\mathbf{r}) \left(-\frac{1}{2}\nabla^2\right) \phi_i^a(\mathbf{r})$$
$$+ \frac{1}{2}\int d^3r \int d^3r' \frac{[n^a(\mathbf{r}) + Z^a(\mathbf{r})][n^a(\mathbf{r}') + Z^a(\mathbf{r}')]}{|\mathbf{r}-\mathbf{r}'|} + E_{xc}[n^a(\mathbf{r})] \tag{C.9}$$

and

$$\tilde{E}^a = \sum_{i_1 i_2} D^a_{i_1 i_2} \int d^3r \tilde{\phi}_i^a(\mathbf{r}) \left(-\frac{1}{2}\nabla^2\right) \tilde{\phi}_i^a(\mathbf{r})$$
$$+ \frac{1}{2}\int d^3r \int d^3r' \frac{[\tilde{n}^a(\mathbf{r}) + \tilde{Z}^a(\mathbf{r})][\tilde{n}^a(\mathbf{r}') + \tilde{Z}^a(\mathbf{r}')]}{|\mathbf{r}-\mathbf{r}'|} + E_{xc}[\tilde{n}^a(\mathbf{r})] + \int d^3r \tilde{n}^a(\mathbf{r}) \overline{v}^a(r), \tag{C.10}$$

where Z^a and $\tilde{Z}^a$ are compensation charges for all-electron density and pseudo electron density, and are added to have a neutral charge density $\rho = n(\mathbf{r}) + \sum_a Z^a(\mathbf{r} - \mathbf{R}^a)$ and $\tilde{\rho} = \tilde{n}(\mathbf{r}) + \sum_a \tilde{Z}^a(\mathbf{r} - \mathbf{R}^a)$. Compensation charges can be determined requiring that pseudo charge density $\tilde{n}^a + \tilde{Z}^a$ has the same electrostatic multipole moments as the all-electron charge density $n^a + Z^a$.

Finally the methods to determine partial wave and projector functions is represented. First, the radial all-electron wave functions $\phi_{nl}^{a,core}$ can be solved from the radial Kohn-Sham equations, which further defines the smooth frozen-core electron density

$$n_c^a(r) = s \sum_{nl}^{\text{core}} \frac{2l+1}{4\pi} [\phi_{nl}^{a,core}(r)]^2 \ . \tag{C.11}$$

Smooth partial waves $\tilde{\phi}_{nl}^a$ are fitted with coefficients c_i so that they will approach smoothly all-electron wavefunctions ϕ_{nl}^a at the augmentation region boundaries $r = r_c^a$

$$\tilde{\phi}_{nl}^a = \sum_{i=0}^{3} c_i r^{2i} \ . \tag{C.12}$$

Smooth partial waves defines the projector functions to be

$$\tilde{p}_{nl}^a(r) = \left(-\frac{1}{2}\nabla^2 + \tilde{v}(r) - \varepsilon_{nl}^a\right) \tilde{\phi}_{nl}^a \ , \tag{C.13}$$

where $\tilde{v} = \tilde{v}^H + \tilde{v}_{xc} + \overline{v}^a$ is the local effective potential. The arbitrary potential $\overline{v}^a$ will be chosen to give the shape of $\tilde{v}$ by

$$\tilde{v}(r) = a^a + b^a r^2 \ , \ r \leq r_c^a \ . \tag{C.14}$$

To find constants a^a and b^a, potential $\overline{v}$ is required to go smoothly to zero at the boundaries of the augmentation regions; $\overline{v}(r_c^a) = 0$ and $d\overline{v}/dr|_{r=r_c^a} = 0$.

In order to be applicable in numerical calculations previous formulas must be discretized with good accuracy. GPAW uses a real-space-grid, and instead of having computationally inefficient large grids, it uses the double-grid technique of Ono and Hirose [75]. The main discretization is done in a coarse-grid and the final accuracy is achieved by interpolating the electron densities, wavefunctions, and potentials to finer, denser grid. This changes the formulation of PAW method only with an additive interpolation mapping [110]. To find self-consistency within Kohn-Sham equations GPAW uses Pulay-mixing [112, 113] for electron densities.

Appendix D: Density-functional tight-binding method

The following description strictly follows the details presented in paper of P. Koskinen et.al. and can be found from the Ref. [79]. Code used in this thesis is hotbit [114]. Density-functional tight-binding (DFTB) [76, 77] Kohn-Sham equations can be derived starting from DFT Kohn-Sham total energy in equation (A.8) with ion-ion interaction included [79]

$$E[n] = \sum_a f_a \langle \Psi_a | -\frac{1}{2}\nabla^2 + V_{ext} + \frac{1}{2}\int d^3r' \frac{n(\mathbf{r}')}{|\mathbf{r}' - \mathbf{r}|} | \Psi_a \rangle + E_{xc}[n] + E_{II} \ , \tag{D.1}$$

where $f_a \in \{0, 1, 2\}$ is the occupation of the eigenstate a.

Electron density can be written in terms of neutral atom electron density n_0 and a small change δn yielding $n(\mathbf{r}) = n_0 + \delta n$ and $n(\mathbf{r}') = n_0' + \delta n'$. With certain δn_0 the total energy will be minimized. For small fluctuations, neutral atom density must be close to ground state density. Expanding the total energy with respect to n_0 and δn all the linearly dependent terms in density fluctuations will vanish. Because n_0 is fixed, the only dependence is on δn, and the expanded total energy can be written

$$\begin{aligned} E[\delta n] \approx & \overbrace{\sum_a f_a \langle \Psi_a | -\frac{1}{2}\nabla^2 + V_{ext} + V_H[n_0] + V_{xc}[n_0] | \Psi_a \rangle}^{=E_{BS}} \\ & \overbrace{+\frac{1}{2}\int\int' \left(\frac{\delta^2 E_{xc}[n_0]}{\delta n \delta n'} + \frac{1}{|\mathbf{r} - \mathbf{r}'|} \right) \delta n \delta n'}^{=E_{fluct}} \\ & \overbrace{-\frac{1}{2}\int V_H[n_0](\mathbf{r}) n_0(\mathbf{r}) + E_{xc}[n_0] + E_{II} - \int V_{xc}[n_0](\mathbf{r}) n_0(\mathbf{r})}^{=E_{rep}} \ , \end{aligned} \tag{D.2}$$

where shorthand notations $\int d^3r = \int$, $\int d^3r' = \int'$, $n(\mathbf{r}) = n$, and $n(\mathbf{r}') = n'$ have been used. Energy can be divided into three parts shown in equation (D.2); (1) band structure part E_{BS} with neutral electron density and no charge transfer in Hamiltonian,

(2) Coulombic energy term E_{fluct} responsible of density fluctuations, and (3) repulsive energy part E_{rep}. The neutral atom Hamiltonian included in band structure part is $H[n_0] = H^0 = -\frac{1}{2}\nabla^2 + V_{ext} + V_H[n_0] + V_{xc}[n_0]$. The repulsive energy part contains, in addition to true repulsive ion-ion interaction, all the rest of the energy terms, that are not dependent on density fluctuations, and are not included in band structure. This kind of division aims for tight-binding type energy interpretation.

Starting from the last term; the repulsive energy can be approximated with a sum of pair potentials depending on distance R_{IJ} between atoms I and J

$$E_{rep} = \sum_{I<J} V_{rep}^{IJ}(R_{IJ}) \ , \tag{D.3}$$

which will be finally parametrized based on reference structures.

To simplify the second term, Coulomb energy due to fluctuations, the extra charge in atom I will be denoted by $\Delta q_I \approx \int_{\Omega_I} \delta n(\mathbf{r}) d^3r$, where Ω_I is the space needed by atom I. Denoting normalized fluctuations with $\delta\tilde{n} = \frac{\delta n}{\Delta q}$ and reducing the integration space to atomic regions Ω_I, the second term of equation (D.2) can be written

$$E_{fluct} = \begin{cases} \frac{1}{2}\Delta q_I^2 \int_{\Omega_I} \int'_{\Omega_I} \left(\frac{\delta^2 E_{xc}[n_0]}{\delta n \delta n'} + \frac{1}{|\mathbf{r}-\mathbf{r}'|} \right) \tilde{n}\tilde{n}' & ; I = J \\ \frac{1}{2}\Delta q_I \Delta q_J \int_{\Omega_I} \int'_{\Omega_J} \frac{1}{|\mathbf{r}-\mathbf{r}'|} \tilde{n}\tilde{n}' & ; I \neq J \ , \end{cases} \tag{D.4}$$

where for on-site energy with $I = J$ Hubbard U identifies to be the coefficient given by the double integral, since all of the quadratic dependencies of charge fluctuations are in E_{fluct}. Hubbard U is by definition the coefficient of the second order term in energy expanded with respect to extra charge Δq. Integration of the exchange-correlation energy derivative for $I \neq J$ will be zero because of the localization of the atoms.

To solve inter-site energy with $I \neq J$, normalized charge fluctuations are chosen to be Gaussian

$$\delta\tilde{n}_I(r) = \frac{1}{(2\pi\sigma_I^2)^{3/2}} \exp\left(\frac{-r^2}{2\sigma_I^2} \right) \ , \tag{D.5}$$

where $\sigma_I = W_I/\sqrt{8\ln 2}$ gives the variation of Gaussian fluctuation distribution for atom I with full width of half maximum (FWHM) denoted by W_I. Using equation (D.5) and extending the integration over all space Ω, double integral of equation (D.4) for $I \neq J$ gives an analytic solution

$$\int_\Omega \int'_\Omega \frac{1}{|\mathbf{r}-\mathbf{r}'|} \tilde{n}\tilde{n}' = \frac{\overbrace{\mathrm{erf}\,(C_{IJ}R_{IJ})}^{=\gamma_{IJ}(R_{IJ})}}{R_{IJ}} \ ; C_{IJ} = 2\sqrt{\frac{\ln 2}{(W_I + W_J)}} \ . \tag{D.6}$$

Change of the integration over all space is valid, if electrons are localized into definite atoms. When charge distributions are far away from each other compared to their

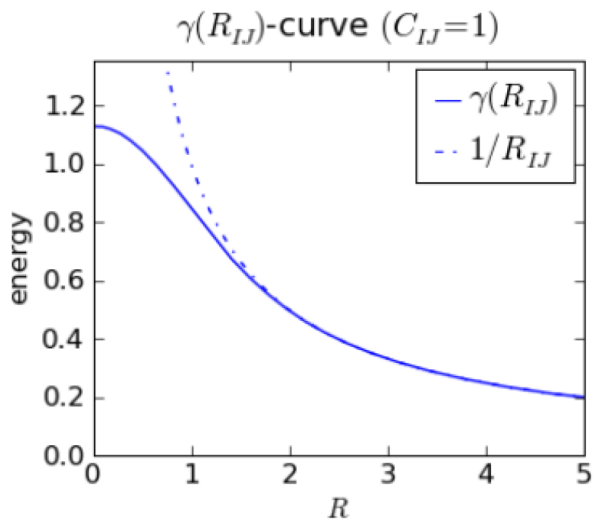

Figure D.1: Example of $\gamma_{IJ}(R_{IJ})$ function for two spherically symmetric Gaussian charge distributions with $W_I = W_J$ and $C_{II} = 1.177/W_I$. With $R_{IJ} \gg W_I$ interaction is Coulomb like i.e. $\propto 1/R_{IJ}$, and with $R_{IJ} \to 0$ approaches to Hubbard U. Taken from Ref. [79].

widths e.g. $R_{IJ} \gg W_I, W_J$, Coulomb interaction of pure point-like charges can be assumed giving dependence $W_I \propto 1/R_{IJ}$. On the other limit $R_{IJ} \to 0$ e.g. $I \to J$ widths are inversely proportional to Hubbard U. This initiates from the exact solution in equation (D.6) giving $\gamma_{IJ}(R_{IJ} \to 0) \to 2\sqrt{\pi}C_{IJ}$, which must be then connected to the on-site energies. After all, fluctuation dependent energy term effectively depends only on Hubbard U. For extra clarification, dependencies of γ_{IJ}, just described, is shown in figure D.1.

The width of the charge fluctuation distribution obtained on the on-site limit is

$$W_I = \sqrt{\frac{8\ln 2}{\pi}}\frac{1}{U_I} \ . \tag{D.7}$$

This is the default dependence that includes information from all of the energy parts in the on-site energy, not only Coulomb part. Finally the fluctuation dependent energy term can be written

$$\begin{aligned} E_{fluct} =& \frac{1}{2}\sum_{IJ}\gamma_{IJ}(R_{IJ})\Delta q_I \Delta q_J \ ; \\ \gamma_{IJ} =& \begin{cases} U_I & I = J \\ \frac{\mathrm{erf}(C_{IJ}R_{IJ})}{R_{IJ}} & I \neq J \ . \end{cases} \end{aligned} \tag{D.8}$$

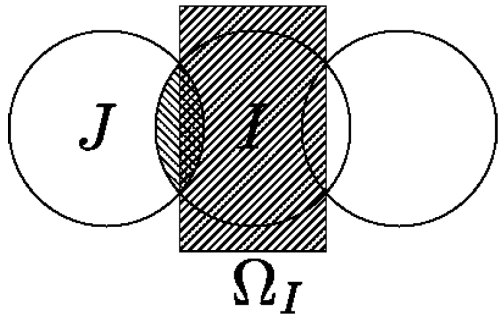

Figure D.2: Convention used in Mulliken charge analysis in integral of the charge equation (D.11). From the overlap of two wavefunctions from different atoms I and J, half will be considered to belong to atom I and half to atom J. Taken from Ref. [79].

The first term in equation (D.2), the band structure part, depends on the neutral atom electron density and does not need any approximations. At this point tight-binding approach is taken account. Tight-binding wavefunctions for eigenstate a are described by linear combination of atomic orbitals (LCAO) $\phi_\nu(\mathbf{r})$

$$\Psi_a(\mathbf{r}) = \sum_\nu c_{a\nu}\phi_\nu(\mathbf{r}) \ , \tag{D.9}$$

which in the case of periodic lattices can be written in terms of Bloch waves

$$\Psi_{a,\mu}(\mathbf{k},\mathbf{r}) = \frac{1}{\sqrt{N}}\sum_{\mathbf{T}} \exp\left(i\mathbf{k}\cdot\mathbf{T}\right)\phi_\mu(\mathbf{r}-\mathbf{T}) \ , \tag{D.10}$$

where $\mathbf{T}$ describes the periodic translation. Bloch waves changes the final form of the Kohn-Sham equations only giving the $\mathbf{k}$-dependence.

Atomic orbitals are normalized and strongly localized, but have small overlap $S_{\mu\nu} = \langle\phi_\mu|\phi_\nu\rangle \neq \delta_{\nu\mu}$. Atomic orbitals will be calculated for pseudo-atom using DFT with LDA and extra confinement to describe free atoms as a part of a solid. Confinement squeezes the orbital wavefunctions, which gives opportunity to use short cut off radius. Hamiltonian for orbital calculation is $H = -\frac{1}{2}\nabla^2 + \frac{Z}{r} + V_H(r) + V_{xc}(r) + V_{conf}$, where the confinement is $V_{conf} \propto \left(\frac{r}{r_0}\right)^2$ and $r_0 \approx 2r_{cov}$, twice the covalent radius. The minimal basis set is usually chosen for DFTB to optimize the computational efficiency. DFT with LDA, but without confinement, is also used for solving free neutral atom electron density n_o.

Mulliken charge analysis is one opportunity to define charges of atoms. Figure D.2 shows the approximative convention that is suitable for strongly localized orbitals i.e.

for only little overlapping atomic regions. Charge on atom I with tight-binding basis of equation (D.9) can be written

$$q_I = \sum_a f_a \sum_{\mu\nu} c^*_{a\mu} c_{a\nu} \int_{\Omega_I} \phi^*_\mu \phi_\nu \ , \tag{D.11}$$

which goes through all the eigenstates a and wavefunctions ϕ_μ and ϕ_ν, and sums together their overlap integrals over the space of atom I. Using Mulliken charge analysis with convention shown in figure D.2, equation (D.11) can be written with the overlap matrix S

$$q_I = \frac{1}{2} \sum_a f_a \sum_{\mu \in I} \sum_\nu \left(c^*_{a\mu} c_{a\nu} S_{\mu\nu} + c^*_{a\nu} c_{a\mu} S_{\nu\mu} \right) \ . \tag{D.12}$$

LCAO basis gives the band structure energy to be

$$E_{BS} = \sum_a f_a \sum_{\nu\mu} c^*_{a\mu} c_{a\nu} H^0_{\mu\nu} \tag{D.13}$$

where $H^0_{\mu\nu} = \langle \phi_\mu | H^0 | \phi_\nu \rangle$. Total energy can be combined from equations (D.3),(D.8), and (D.13). Written in three rows similarly to equation (D.2) DFTB total energy is

$$\begin{aligned} E = & \sum_a f_a \sum_{\nu\mu} c^*_{a\mu} c_{a\nu} H^0_{\mu\nu} \\ & + \frac{1}{2} \sum_{IJ} \gamma_{IJ}(R_{IJ}) \Delta q_I \Delta q_J \\ & + \sum_{I \neq J} V^{IJ}_{rep}(R_{IJ}) \ . \end{aligned} \tag{D.14}$$

Kohn-Sham equations in DFTB can be finally written by taking variation of expectation value of the total energy with respect to $c^*_{a\mu}$

$$\sum_\nu c_{a\nu} \left(H_{\mu\nu} - \varepsilon_a S_{\mu\nu} \right) = 0 \ , \tag{D.15}$$

where ε_a is a Lagrange multiplier. Hamiltonian matrix element $H_{\mu\nu}$ is

$$\begin{aligned} H_{\mu\nu} = & H^0_{\mu\nu} + \frac{1}{2} S_{\mu\nu} \sum_K \left(\gamma_{IK} + \gamma_{JK} \right) \Delta q_K \ ; \ \mu \in I, \ \nu \in J \\ = & H^0_{\mu\nu} + h^1_{\mu\nu} S_{\mu\nu} \ , \end{aligned} \tag{D.16}$$

where $h^1_{\mu\nu} = \frac{1}{2} \left(\epsilon_I + \epsilon_J \right)$ gives the average of electrostatic energies of atom I and atom J.

Tight-binding Kohn-Sham equation must be solved self-consistently. The computational procedure starts by guessing trial charges for atoms and proceeds with construction of the Hamiltonian and the wavefunctions; hence, giving computational loop $q_I \rightarrow h^1_{\mu\nu} \rightarrow H_{\mu\nu} \rightarrow \Psi_a \rightarrow q_I \rightarrow \ldots$.

The repulsive pair potential V^{IJ}_{rep} can be fitted to a set of DFT total energies for specific reference systems. On-site and inter-site energies $H^0_{\mu\nu}$ and $S_{\mu\nu}$ are also parameterized with DFT. For inter-site part, Slater-Koster transformations is used to decompose atomic orbitals giving Slater-Koster tables. These parameterizations are the characteristic of tight-binding approach and reduces the computational load significantly. Compared to evaluation of interactions on every step like in DFT, using pre-parameterization in DFTB is computationally much more efficient.

Appendix E: Theoretical modeling of resonant Raman spectroscopy

Details that will be represented next follow the description reported in review of the Ref. [11]. Resonant Raman calculation mimics the scattering process strictly, which was described in chapter 2.6. In first order scattering process, figure 2.6 (a), resonant Raman intensity can be written by denoting electron-photon coupling with $M^{el-phot}$ and electron-phonon coupling with $M^{el-phon}$ as [11]

$$\begin{aligned} I(\omega, E_L) =& C \sum_j \left| \sum_a J_a(\omega) \right|^2 \quad ; \\ J_a(\omega) =& \frac{M^{el-phot}(k-q, jb) M^{el-phon}(q, ba) M^{el-phot}(k, aj)}{\Delta E_{aj}(\Delta E_{bj} - \hbar\omega)} \quad , \end{aligned} \tag{E.1}$$

where j, a and b are the initial, excited and scattered electron states respectively, and $\Delta E_{aj} = E_L - (E_a - E_j) - i\gamma$ with a broadening factor γ for resonant event. E_L is the energy of the laser, and E_a and E_j energies of the excited and initial electron states. Constant C includes for example the thermal occupation of phonons and possible extra structural dependencies.

Based on description of the first-order Raman scattering, it is easy to construct second-order process shown in figure 2.6 (c) by just adding an extra electron-phonon coupling matrix [11]

$$\begin{aligned} I(\omega, E_L) =& C \sum_j \left| \sum_{a,b,\omega_1,\omega_2} J_{a,b}(\omega_1, \omega_2) \right|^2 \quad ; \\ J_{a,b}(\omega_1, \omega_2) =& \frac{M^{el-phot}(k-q, jc) M^{el-phon}(-q, cb) M^{el-phon}(q, ba) M^{el-phot}(k, aj)}{\Delta E_{aj}(\Delta E_{bj} - \hbar\omega_1)(\Delta E_{cj} - \hbar\omega_1 - \hbar\omega_2)} \quad , \end{aligned} \tag{E.2}$$

where now also one extra intermediate electron state c appears in the scattering process and $\omega = \omega_1 + \omega_2$. The rest of the interpretation remains the same.

Second-order scattering can also exist as a one-phonon process shown in figure 2.6 (b). One of two the electron-phonon coupling matrices in equation (E.2) is replaced then by

matrix describing electron coupling to some defect in the system; $M^{el-pho}(-q, cb) \rightarrow M^{el-defect}(cb)$ in numerator and $(\Delta E_{cj} - \hbar\omega_1 - \hbar\omega_2) \rightarrow (\Delta E_{cj} - \hbar\omega_1)$ in denominator. J does not depend anymore on ω_1 and ω_2, but just one phonon frequency ω_1. Dependence on four electron states still remains [11]

$$\begin{aligned} I(\omega, E_L) =& C \sum_j \left| \sum_{a,b,\omega_1,\omega_2} J_{a,b}(\omega_1, \omega_2) \right|^2 ; \\ J_{a,b}(\omega_1) =& \frac{M^{el-phot}(k-q, jc) M^{el-defect}(cb) M^{el-phon}(q, ba) M^{el-phot}(k, aj)}{\Delta E_{aj}(\Delta E_{bj} - \hbar\omega_1)(\Delta E_{cj} - \hbar\omega_1)} . \end{aligned} \tag{E.3}$$

Electron-photon coupling from initial state Ψ_i to final state Ψ_f can be estimated mainly from the product of polarization vector P of the light and dipole vector $\langle \Psi_f(k) | \nabla | \Psi_i(k) \rangle$ of the system [11]

$$M^{el-phot}(k, fi) = i \frac{e\hbar}{m\omega} \sqrt{\frac{I}{\varepsilon c}} e^{i(\omega_f - \omega_i \mp \omega)t} P \cdot \langle \Psi_f(k) | \nabla | \Psi_i(k) \rangle , \tag{E.4}$$

where I and ω are the intensity and the frequency of the photon, and $\mp$ denotes photon absorption and emission, respectively. For absorption initial state is on valence and final state conduction band, whereas for emission vice versa. Related to equations (E.1), (E.2) and (E.3), for the first photon absorption initial state $i = j$ and final state $f = a$.

Electron-phonon coupling is usually taken from the change in the effective Kohn-Sham potential under the Born-Oppenheimer approximation [11]

$$M_j^{el-phon}(q, fi) = \mathbf{v}_q^j \cdot \langle \Psi_f(k+q) | \nabla V_{eff} | \Psi_i(k) \rangle , \tag{E.5}$$

where $\mathbf{v}_q^j$ is the eigenvector of the phonon j with wave vector q; i and f are for the initial and final electron states during the phonon scattering. Related to the equations (E.1), (E.2) and (E.3) initial state is $i = a$ and final state is $f = b$ for the first electron-phonon coupling. Scattered states and change in effective potential can be calculated for example using linear response theory, for which the change in effective potential is usually written in response form with respect to atomic displacements $\frac{\delta V_{eff}}{\delta R}$ [67, 68]. The more complete descriptions about resonant Raman calculation, including for example the derivation of the self-consistently solvable linear response theory equations for electron-phonon coupling, are omitted.

References

[1] H.W. Kroto, J.R. Heath, S.C. O'Brien, R.F. Curl, and R.E. Smalley, Nature (London) **318**, 162 (1985).

[2] S.Iijima, Nature (London) **354**, 56 (1991).

[3] M.I. Katsnelson, Mater. Today **10**, 20 (2007).

[4] J.C. Meyer, A.K. Geim, M.I. Katsnelson, K.S. Novoselov, T.J. Booth, and S. Roth, Nature (London) **446**, 60 (2007).

[5] K.S. Novoselov, A.K. Geim, S.V. Morozov, D. Jiang, Y. Zhang, S.V. Dubonos, I.V. Grigorieva, and A.A. Firsov, Science **306**, 666 (2004).

[6] K.S. Novoselov, A.K. Geim, S.V. Morozov, D. Jiang, M.I. Katsnelson, I.V. Grigorieva, S.V. Dubonos, and A.A. Firsov, Nature **438**,197 (2005).

[7] Y. Zhang, Y.-W. Tan, H.L. Stormer, and P. Kim, Nature **438**, 201 (2005).

[8] C. Berger, Z. Song, X. Li, X. Wu, N. Brown, C. Naud, D. Mayou, T. Li, J. Hass, A.N. Marchenkov, E.H. Conrad, P.N. First, and W.A. de Heer, Science **312**,1191 (2006).

[9] E. Rollings, G.-H. Gweon, S.Y. Zhou, B.S. Mun, J.L. McChesney, B.S. Hussain, A.V. Fedorov, P.N. First, W.A. de Heer, and A. Lanzara, J. Phys. Chem. Solids **67**, 2172 (2006).

[10] A.H. Castro Neto, F. Guinea, N.M.R. Peres, K.S. Novoselov, and A.K. Geim, Rev. Mod. Phys. **81**, 109 (2009).

[11] M.S. Dresselhaus, G. Dresselhaus, R. Saito, and A. Jorio, Phys. Rep. **409**, 47 (2005).

[12] M.S. Dresselhaus, G. Dresselhaus, A. Jorio, A.G. Souza Filho, and R. Saito, Carbon **40**, 2043 (2001).

[13] P.C. Eklund, J.M. Holden, and R.A. Jishi, Carbon **33**, 959 (1995).

[14] C. Thomsen and S. Reich, Topics Appl. Physics **108**, 115 (2007).

[15] R. H. Baughman, A. A. Zakhidov, and W. A. de Heer, Science **297**, 787 (2002).

[16] J.M. Kinaret, T. Nord, and S. Viefers, Appl. Phys. Lett. **82**, 1287 (2003).

[17] S. Stankovich, D.A. Dikin, G.H.B. Dommet, K.M. Kohlhaas, E.J. Zimney, E.A. Stach, R.D. Piner, S.T. Nguyen, and R.S. Ruoff, Nature (London) **442**, 282 (2006).

[18] A.G. Nasibulin, P.V. Pikhitsa, H. Jiang, D.P. Brown, A.V. Krasheninnikov, A.S. Anisimov, P. Queipo, A. Moisala, D. Gonzalez, G. Lientschnig, A. Hassanien, S.D. Shandakov, G. Lolli, D.E. Resasco, M. Choi, D. Tománek, and E.I. Kauppinen, Nature Nanotechnology **2**, 156 (2006).

[19] P. Avouris, Z. Chen, and V. Perebeinos, Nature Nanotechnology **2**, 605 (2007).

[20] G.G. Wildgoose, C.E. Banks, and R.G. Compton, Small **2**, 182 (2006).

[21] N. Nemec, D. Tománek, and G. Cuniberti, Phys. Rev. B **77**, 125420 (2008).

[22] N. Nemec, D. Tománek, and G. Cuniberti, Phys. Rev. Lett. **96**, 076802 (2006).

[23] J.C. Charlier, Acc. Chem. Rev. **35**, 1063 (2002).

[24] M. Yoon, S. Han, G. Kim, S.B. Lee, S. Barber, E. Osawa, J. Ihm, M. Terrones, F. Banhart, J.-C. Charlier, N. Grobert, H. Terrones, P.M. Ajayan, and D. Tománek, Phys. Rev. Lett. **92**, 075504 (2004).

[25] A.V. Krasheninnikov. *Irradiation-induced phenomena in carbon nanotubes* in *Chemistry of carbon nanotubes* edited by V. A. Basiuk and E. V. Basiuk. American Scientific Publisher, 2008.

[26] F. Banhart and A.V. Krasheninnikov. Nature Materials **6**, 723 (2007).

[27] C. Jin, K. Suenaga, and S. Iijima. Nature Nanotechnology **3**, 17 (2008).

[28] F. Ding, Phys. Rev. B **72**, 245409 (2005).

[29] M. Ishigami, H. Joon Choi, S. Aloni, S. G. Louie, M. L. Cohen, and S. Zettl, Phys. Rev. Lett. **93**, 196803 (2005).

[30] H. Amara, S. Latil, V. Meunier, Ph. Lambin, and J.-C. Charlier. Phys. Rev. B **76**, 115423 (2007).

[31] M. Vandescuren, H. Amara, R. Langlet, and Ph. Lambin, Carbon **45**, 349 (2007).

[32] G.-D. Lee, C. Z. Wang, E. Yoon, N.-M. Hwang, D.-Y. Kim, and K. M Ho, Phys. Rev. Lett. **95**, 205501 (2005).

[33] C. W. Chang, D. Okawa, H. Garcia, A. Majumdar, and A. Zettl, Phys. Rev. Lett. **99**, 045901 (2007).

[34] J. N. Barisci, G. G. Wallace, and R. H. Baughman, Journal of Electroanalytical Chemistry **488**, 92 (2000).

[35] Z. F. Ren, Z. P. Huang, J. W. Xu, J. H. Wang, P. Bush, M. P. Siegal, and P. N. Provencio, Science **282**, 1105 (1998).

[36] L. Song, W. Ma, Y. Ren, W. Zhou, S. Xie, P. Tan, and L. Sun, Appl. Phys. Lett. **92**, 121905 (2008).

[37] J. Loos, A. Alexeev, N. Grossiord, C. E. Koning, and O. Regev, Ultramicroscopy **104**, 160 (2005).

[38] N. Geblinger, A. Ismach, and E. Joselevich, Nature Nanotechnology **3**, 195 (2008).

[39] J. Wu, K. C. Hwang, and Y. Huang, Journal of Mechanics and Physics of Solids **56**, 279 (2007).

[40] X. Guo, A. Y. T. Leung, X. Q. He, H. Jiang, and Y. Huang, Composites: Part B **39**, 202 (2007).

[41] A. Maiti, Chem. Phys. Lett. **331**, 21 (2000).

[42] M. Huhtala, A. Kuronen, and K. Kaski. I. J. Mod. Phys. C **15**, 517 (2004).

[43] M. Huhtala, A. Kuronen, and K. Kaski. Comp. Phys. Comm. **146**, 30 (2002).

[44] D. Qian, G. J. Wagner, W. K. Liu, M.-F. Yu, and R. S. Ruoff, Appl. Mech. Rev. **55**, 495 (2002).

[45] D. Jiang, B.G. Sumpter, and S. Dai, The Journal of Chem. Phys. **126**, 134701 (2007).

[46] K. Nakada, M. Fujita, G. Dresselhaus, and M.S. Dresselhaus, Phys. Rev. B **54**, 17954 (1996).

[47] M. Yamada, Y. Yamakita, and K. Ohno, Phys. Rev. B **77**, 054302 (2008).

[48] J.-C. Charlier, A. De Vita, X. Blase, and R. Car, Science **275**, 647 (1997).

[49] Y. H. Lee, S. G. Kim, and D. Tománek, Phys. Rev. Lett. **78**, 2393 (1997).

[50] T. Kawai, Y. Miyamoto, O. Sugino, and Y. Koga, Phys. Rev. B **62**, R16349 (2000).

[51] E. Hernandez, P. Ordejon, I. Boustani, A. Rubio, and J. A. Alonso, J. Chem. Phys. **113**, 3814 (2000).

[52] D. Gunlycke, D. A. Areshkin, and C. T. White, Appl. Phys. Lett. **90**, 142104 (2007).

[53] Y. Kobayashi, K.-I. Fukui, T. Enoki, and K. Kusakabe, Phys. Rev. B **73**, 125415 (2006).

[54] M. Wimmer, I. Adagideli, S. Barber, D. Tománek, and K. Richter. Phys. Rev. Lett. **100**, 177207 (2008).

[55] K. Jian, A. Yan, I. Kulaots, G. P. Crawford, and R. Hurt, Carbon **44**, 2102 (2006).

[56] Y. Ouyang, Y. Yoon, J.K. Fodor, and J. Guo, Appl. Phys. Lett. **89**, 203107 (2006).

[57] Y. Yoon and J. Guo, Appl. Phys. Lett. **91**, 073103 (2007).

[58] G.-D. Lee, C.Z. Wang, E. Yoon, N.-M. Hwang, and K.M. Ho, Appl. Phys. Lett. **92**, 043104 (2008).

[59] Y. Gan, J. Kotakoski, A.V. Krasheninnikov, K. Nordlund, and F. Banhart, New J. Phys. **10**, 023022 (2008).

[60] U. von Barth, Physica Scripta **T109**, 9 (2004).

[61] P. Hohenberg and W. Kohn, Phys. Rev. **136**, B864 (1964).

[62] W. Kohn and L.J. Sham, Phys. Rev. **140**, A1133 (1965).

[63] A. Hartschuh, H. N. Pedrosa, L. Novotny, and T. D. Krauss, Science **301**, 1354 (2003).

[64] A. Ferrari, Solid State Comm. **143**, 47 (2007).

[65] J. Zhou and J. Dong, Appl. Phys. Lett. **91**, 173108 (2007).

[66] L.G. Cancado, M.A. Pimenta, B.R.A. Neves, G. Medeiros-Ribeiro, T. Enoki, Y. Kobayashi, K. Takai, K. Fukui, M.S. Dresselhaus, R. Saito, and A. Jorio, Phys. Rev. Lett. **93**, 047403 (2004).

[67] S.Y. Savrasov, Phys. Rev. B **54**, 16470 (1996).

[68] S.Y. Savrasov and D.Y. Savrasov, Phys. Rev. B **54**, 16487 (1996).

[69] V.N. Popov, New J. Phys. **6**, 17 (2004).

[70] Y. Gan, L. Sun, and F. Banhart, Small **4**, 587 (2008).

[71] C.Ö. Girit, J.C. Meyer, R. Erni, M.D. Rossell, C. Kisielowski, L. Yang, C.-H. Park, M.F. Crommie, M.L. Cohen, S.G. Louie, and A. Zettl, Science **27**, 1705 (2009).

[72] GPAW wiki, https://wiki.fysik.dtu.dk/gpaw.

[73] P.E. Böchl, Phys. Rev. B **50**, 17953 (1994).

[74] John P. Perdew, Kieron Burke, and Matthias Ernzerhof, Phys. Rev. Lett. **77**, 3865 (1996).

[75] T. Ono and K. Hirose, Phys. Rev. Lett. **82**, 5016 (1999).

[76] D. Porezag, Th. Frauenheim, Th. Köhler, G. Seifert, and R. Kaschner, Phys. Rev. B **51**, 12947 (1995).

[77] M. Elstner, D. Porezag, G. Jungnickel, J. Elstner, M. Haugk, Th. Frauenheim, S. Suhai, and G. Seifert, Phys. Rev. B **58**, 7260 (1998).

[78] P. Koskinen, H. Häkkinen, G. Seifert, S. Sanna, Th. Frauenheim, and M. Moseler. New J. Phys **8**, 9 (2006).

[79] P. Koskinen and V. Mäkinen, *Dftb for beginners*, *(submitted for publication)* (2009).

[80] W.A. Hofer, A.S. Foster, and A.L. Shluger, Rev. Mod. Phys. **75**, 1287 (2003).

[81] J. Tersoff and D.R. Hamann, Phys. Rev. Lett. **50**, 1998 (1983).

[82] J. Tersoff and D.R. Hamann, Phys. Rev. B **31**, 805 (1985).

[83] Kimmo Tuominen, *Group Theory and Physics*, Lecture Notes University of Jyväskylä (2006).

[84] H. Wilhelm, M. Lelaurain, E. McRae, and B. Humbert, J. Appl. Phys. **84**, 6552 (1998).

[85] E.W.S. Caetano, V.N. Freire, S.G. dos Santos, D.S. Galvao, and F. Sato, J. Chem. Phys. **128**, 164719 (2008).

[86] E. B. Barros, A. Jorio, G. G. Samsonidze, R. B. Capaz, A. G. Souza Filho, J. Mendes Filho, G. Dresselhaus, and M. S. Dresselhaus, Phys. Rep. **431**, 261 (2006).

[87] M. Damnjanovic, I. Milosevic, T. Vukovic, and R. Sredanovic, Phys. Rev. B **60**, 2728 (1999).

[88] I.B. Bozovic and M. Vujicic, J. Phys. A: Math. Gen. **14**, 777 (1981).

[89] S. Reich, *Carbon nanotubes: Vibrational and electronic properties (PhD thesis)*, Technical University of Berlin, (2002).

[90] J.B. Marion and S.T. Thornton, *Classical dynamics of particles and systems*, Harcourt Brace & Company, USA, 4th edition, 1995.

[91] Mika Petterson, *Molecular Spectroscopy*, Lecture Notes University of Jyväskylä, 2007.

[92] R. Saito, G. Dresselhaus, and M.S. Dresselhaus, *Physical Properties of Carbon Nanotubes*, Imperial College Press, London, 1998.

[93] Ofir E. Alon, Phys. Rev. B **63**, 201403 (2001).

[94] P.C. Eklund, J.M.Holden, and R.A. Jishi, Carbon **33**, 959 (1995).

[95] S. Guha, J. Menendez, J.B. Page, and G.B. Adams, Phys. Rev. B **53**, 13106 (1996).

[96] R. Saito, T. Takeya, T. Kimura, G. Dresselhaus, and M.S. Dresselhaus, Phys. Rev. B **57**, 4145 (1998).

[97] G. Henkelman and H. Jonsson, J. Chem. Phys. **113**, 9978 (2000).

[98] S. Arrhenius, J. Phys. Chem. **4**, 226 (1889).

[99] K.J. Laidler and M.C. King, J. Chem. Phys. **87**, 2657 (1983).

[100] E. Bitzek, P. Koskinen, F. Gähler, M. Moseler, and P. Gumbsh, Phys. Rev. Lett. **97**, 170201 (2006).

[101] B. Huang, M. Liu, N. Su, J. Wu, W. Duan, B.-L. Gu, and F. Liu, Phys. Rev. Lett. **102**, 166404 (2009).

[102] T. Wassman, A.P. Seitsonen, A.M. Saitta, M. Lazzeri, and F. Mauri, Phys. Rev. Lett. **101**, 096402 (2008).

[103] A.V. Krasheninnikov, P.O. Lehtinen, A.S. Foster, and R.M. Nieminen. Chem. Phys. Lett. **418**, 132 (2006).

[104] F. Banhart, J. X. Li, and A.V. Krasheninnikov. Phys. Rev. B. **71**, 241408(R) (2005).

[105] A.V. Krasheninnikov, P.O. Lehtinen, A.S. Foster, and R.M. Nieminen, Phys. Rev. Lett. **102**, 126807 (2009).

[106] Private communication with P. Eklund (2009).

[107] J.P. Perdew and S. Kurth, *Density Functionals for Non-Relativistic Coulomb Systems*, Lecture Notes in Physics. Springer, Berlin, 1998.

[108] Robert van Leeuwen, *Density Functional Theory and its Applications in Nanoscience*, Lecture Notes University of Jyväskylä, 2008.

[109] U. von Barth and L. Hedin, J. Phys. C **5**, 1629 (1972).

[110] J.J. Mortensen, L.B. Hansen, and K.W. Jacobsen, Phys. Rev. B **71**, 035109 (2005).

[111] N. Troullier and J.L. Martins, Phys. Rev. B **43**, 1993 (1991).

[112] P. Pulay, Chem. Phys. Lett. **73**, 393 (1980).

[113] G. Kresse and J. Furthmuller, Phys. Rev. B **54**, 11169 (1996).

[114] hotbit wiki, https://trac.cc.jyu.fi/projects/hotbit/wiki